Exciton Center-of-Mass Motion in Quantum Wells and Quantum Wires

DISSERTATION

zur Erlangung des akademischen Grades
doctor rerum naturalium
(dr. rer. nat.)
im Fach Physik

eingereicht an der
Mathematisch-Naturwissenschaftlichen Fakultät I
Humboldt-Universität zu Berlin

von
Herr Dipl.-Phys. Anastassios Siarkos
geboren am 10.03.1966 in Berlin

Präsident der Humboldt-Universität zu Berlin:
Prof. Dr. Dr. h.c. H. Meyer

Dekan der Mathematisch-Naturwissenschaftlichen Fakultät I:
Prof. Dr. B. Ronacher

Gutachter:

1. Prof. Dr. R. Zimmermann
2. Prof. Dr. U. Rössler
3. Prof. Dr. F. Henneberger

eingereicht am:	29. Mai 2000
Tag der mündlichen Prüfung:	10. November 2000

Abstract

This thesis presents a thorough investigation of the center-of-mass dispersion properties of excitons in semiconductor quantum wells and quantum wires. The $\vec{k}\cdot\vec{p}$ coupling of heavy and light holes as well as the Coulomb coupling are taken fully into account.

High-quality numerical calculations of the exciton center-of-mass dispersion are achieved by optimizing the center-of-mass transformation, making use of an Ansatz for the dependence of the groundstate exciton upon the center-of-mass momentum $\vec{Q}$. Indeed, the envelope in the subband expansion of the groundstate exciton is to a good approximation independent of Q. This technique made possible for the first time multiband calculations in quantum wires that take the Coulomb coupling fully into account.

Various physically interesting effects are found and investigated, like, e.g., the non-monotonous increase of the exciton groundstate binding energy with Q or the fact that the exciton groundstate energy follows the exciton continuum edge rather closely.

The center-of-mass optimization leads also to an analytical expression for an estimate of the exciton groundstate center-of-mass mass.

Keywords:
exciton mass, quantum wells and wires, semiconductor heterostructures, numerical methods

Zusammenfassung

Diese Arbeit stellt eine gründliche Analyse der Schwerpunktsbewegung von Exzitonen in Halbleiter-Quantengräben und -Quantendrähten dar. Dabei wurde die $\vec{k} \cdot \vec{p}$ -Kopplung der schweren und leichten Löcher im Valenzband sowie das Coulomb-Potential voll berücksichtigt.

Die Optimierung der Schwerpunktstransformation auf der Basis eines Ansatzes für die Abhängigkeit des Grundzustands des Exzitons vom Schwerpunktsimpuls $\vec{Q}$ ermöglichte numerische Ergebnisse hoher Qualität. Es zeigt sich nämlich, daß in einer Subbandentwicklung die Enveloppe des Grundzustands des Exzitons in guter Näherung unabhängig vom Schwerpunktsimpuls ist. So konnten erstmalig Multiband-Exziton-Berechnungen in Quantendrähten mit voller Berücksichtigung der Coulomb-Wechselwirkung durchgeführt werden.

Die in dieser Arbeit dargestellten Untersuchungen zeigen interessante physikalische Effekte auf, wie beispielsweise eine nichtmonotone Zunahme der Bindungsenergie des exzitonischen Grundzustands mit wachsendem Q und einen zur entsprechenden Kontinuumskante weitestgehend parallelen Verlauf der Dispersion des exzitonischen Grundzustands.

Die Optimierung der Schwerpunktstransformation führt außerdem zu einem analytischen Ausdruck für eine mittlere Masse, die relevant für den exzitonischen Grundzustand ist.

Schlagwörter:
Exziton Masse, Quantengräben und Quantendrähte, Halbleiter Heterostrukturen, Numerische Methoden

Contents

Chapter 1

Introduction

More than 30 years have passed since Esaki and Tsu back in 1969 first proposed to alternatingly grow different material layers on a substrate and create this way a solid with completely new properties [1]. Today, such material systems, called heterostructures, are of great importance both in technology and research. Fabrication techniques, like molecular beam epitaxy (MBE) or metal organic chemical vapour deposition (MOCVD), evolved that allow an astonishing degree of growth control; nowadays, heterostructures can be *tailored* to the desired properties.

A main property of semiconductor heterostructures is the confinement of the free carriers in one, for quantum wells (QW), two, for quantum wires (QWR), or all three, for quantum dots, spatial directions. This spatial confinement leads, among others, to an enhancement of excitonic effects, due to the decreased average distance of the constituent electron and hole. Excitonic effects become, hence, more pronounced in lower dimensions: excitons survive even at room temperature and dominate the optical properties near the fundamental band edge at low temperatures. For example, the absence of an energy shift with increasing excitation density has been attributed to direct involvement of excitons in QWR lasing [2, 3, 4]. Further, early expectations that QWR devices would profit from the diverging one-dimensional density of states had to be revised due to excitonic interactions reducing the spectral density considerably [5, 6, 7, 8]. In addition, remarkable effects have been predicted such as an exciton crystal in finite-length QWR [9]. As a consequence, the physics of excitonic effects became of prominent theoretical and practical importance in low-dimensional heterostructures.

The internal structure of the groundstate exciton, i.e., the relative motion of electron and hole, determines the binding energy, the polarization dependence of its absorption, and influences the interaction with external electric and magnetic fields. On the other hand, details of the excitonic optical spectra related to the center-of-mass (COM) motion like, e.g., inhomogeneous broadening and Stokes shift between photoluminescence (PL) and absorption, are frequently used for structure characterization. These features are influenced by exciton localization and diffusion in the presence of interface or alloy disorder [10, 11]. Spatially resolved spectroscopy techniques like micro PL and near-field scanning optical microscopy allow direct observation of exciton COM quantization in local potential minima [12]. In addition, optical spectra and their temporal evolution are determined by the exciton formation processes [13, 14, 15, 16] and the subsequent energy and spin [17, 18, 19] relaxation dynamics.

In semiconductor QW, the broken translational symmetry in the growth direction leads to new features like the splitting of heavy and light hole bands at the Γ-point and the formation of heavy and light excitons. Due to the large hole-to-electron mass ratio, the influence of the valence-band dispersion features on the COM motion is greater than on the relative motion. The exciton dispersions are, thus, strongly non-parabolic. Direct consequences of the exciton dispersion anharmonicity in QW like slow indirect excitonic transitions due to camel-back shaped dispersions [20] have been experimentally observed [21].

All these phenomena are intimately related to the exciton COM properties whereby different energy and COM momentum regions of the exciton dispersion are probed in different processes. A detailed analysis of the exciton COM properties in low-dimensional heterostructures is, therefore, highly desirable.

Not surprisingly, a steady stream of papers calculating QW excitons at vanishing COM momentum, $Q = 0$, with improving accuracy and insight was seen over the last fifteen years [22, 23, 24, 25, 26, 27, 28, 29]. The numerical effort for such calculations remains reasonable due to the high symmetry of this point. In contrast, much less has been done regarding QW excitons at finite momentum [30, 31, 32, 33] and even less for QWR excitons. For QWR, all published work on optical spectra prior to our own (i) used drastically simplified models for the underlying single-particle bands, or (ii) considered highly idealized geometries, [34] or (iii) treated the Coulomb interaction only approximately. The first group [35, 36, 37, 38] typically ignored the multiband character of the valence-band maximum. The last group either ignored the Coulomb interaction completely, [39, 40] added it as a rigid shift of all states at a final stage [41, 42], approximated it by a one-dimensional form, [34] or, in the best case, used a Hartree approximation [6, 43]. In the latter, each constituent of the exciton reacts to the charge distribution of the other one, but correlations between both particles are neglected. For QWR, again, work has been focused on properties of the exciton at rest, $Q = 0$.

The fact that there are so few publications on multiband exciton dispersions (i.e., with the coupling of light- and heavy-hole valence band explicitly taken into account) in QW and, before our own [44], none even for multiband exciton at $Q = 0$ in realistic QWR structures is related to the very demanding calculations necessary. On the one hand, methods for improving the numerical accuracy and reducing the effort of such calculations are desired. On the other hand, easy-to-use approaches that give the main features of the exciton dispersion with at least moderate accuracy like, e.g., an *average* mass, would be particularly useful. Furthermore, a deeper understanding of the processes and mechanisms determining the exciton dispersion features in heterostructures is necessary. With this work we aim to address the above issues. We introduce an optimized COM transformation, that enables us to calculate exciton dispersions with unprecedented accuracy even for rather large COM momenta. We investigate thoroughly the exciton dispersion properties in QW. We present multiband exciton results for a realistic V-groove QWR structure. We, further, manage to extract an analytical expression for an average COM mass for the exciton groundstate.

The main body of the work is structured as follows: After sketching some relevant bulk semiconductor basics in Chap. 2, the theoretical model for the description of the exciton in QW and QWR used in this work is developed in Chap. 3. The optimization of the COM transformation, which proved essential for the high-quality of our numerical results, is addressed in Chap. 4. In Chap. 5 results for the exciton dispersions in GaAs/$Al_{0.3}Ga_{0.7}As$ QW are presented. These are obtained with two different numerical methods: (i) a well established method in momentum space, that gives results of highest accuracy, and (ii) a discretization method in real space used for the first time for multiband exciton calculation in QW and QWR. The latter is of less accuracy, but has its own merits. The features of the exciton dispersions in QW are discussed in detail. In the following Chap. 6 an analytical expression for the average groundstate exciton mass is introduced and its applicability is demonstrated. Further, an effective reduced exciton mass is proposed, which proved useful in the understanding of experimental magnetoexciton data in $Zn_{0.87}Cd_{0.13}Se$/ZnSe and ZnSe/$Zn_{0.85}Mg_{0.15}Se$ QW. In Chap. 7, results of multiband exciton calculations for a realistic V-groove QWR obtained with the real space method of Chap. 5 are presented. A short summary of our main achievements and a brief outlook is given in Chap. 8. Some details related to various topics discussed in the main body of this work are outlined in the appendices A-E.

Chapter 2

Semiconductor Basics

As a result of the periodicity of crystal solids, all elementary excitations, like, e.g., free carriers and free excitons in semiconductors, are characterized by a crystal momentum $\vec{k}$; the excitation's dispersion $\mathcal{E}(\vec{k})$ is its energy variation with the crystal momentum.

Time inversion symmetry is valid in crystal solids in the absence of magnetic fields. A direct consequence is the inversion symmetry of the band dispersions, $\mathcal{E}(\vec{k}\uparrow) = \mathcal{E}(-\vec{k}\downarrow)$ [45]; it is of no relevance whether an elementary excitation of crystal momentum $\vec{k}$ propagates to the "left" or to the "right".

However, most solids crystallize in structures that have more symmetries than the simple translational one. These additional symmetries determine further bandstructure properties.

2.1 Zinc-blende bulk semiconductors

Almost all semiconductors of practical interest crystallize in the diamond, zinc-blende (sphalerite), wurtzite, chalcopyrite, or rocksalt structure. Some of the technologically most important III-V compounds, in particular GaAs, AlAs, and its mixed crystal $\mathrm{Al}_x\mathrm{Ga}_{1-x}\mathrm{As}$, which will be of main concern to us, crystallize in the zinc-blende structure at normal pressure. Also many of the important II-VI compounds like the materials (Zn,Cd)(S,Se,Te) or MgSe show up at least in a zinc-blende modification. This lattice, similar to the one of the diamond structure, consists of two interpenetrating, face-centered (f.c.c.) lattices, displaced relative to each other by one fourth of the cube's main diagonals (see Fig. 2.1). One of these lattices is occupied by the cation atoms and the other by the anion atoms of the compound. The nearest neighbors are arranged tetrahedrally around each lattice site. This structure shows all the symmetry elements of a tetrahedron (point group T_d). The diamond structure exhibits cubic symmetry. Additionally to the T_d symmetry elements it shows also inversion symmetry with respect to the point $(\frac{1}{8}, \frac{1}{8}, \frac{1}{8})$. The inversion symmetry of the lattice leads to doubly degenerate bands [46]. In contrast, the zinc-blende structure lacks of

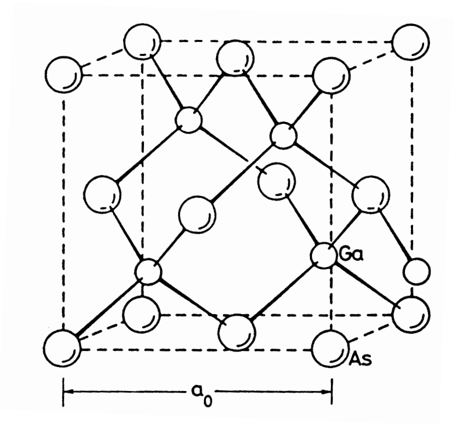

Figure 2.1: Primitive cell of a zinc-blende lattice (GaAs), a_0 is the lattice constant (a_0=0.565nm for GaAs).

inversion symmetry due to the two f.c.c. lattices being occupied by dissimilar atoms.

The reciprocal lattice of the f.c.c. Bravais lattice underlying the zinc-blende structure is a body-centered cubic lattice. The first Brillouin zone (BZ) of the reciprocal lattice is a truncated octahedron, see Fig. 2.2(a). Several high symmetry points and lines of the first Brillouin zone, e.g. the Γ, X and L points, are displayed. The ΓX lines will be of special interest to us, since we will concentrate on QW and QWR grown along the [001] directions.

The GaAs band structure near the band gap is shown in Fig. 2.2(b). The bands at the vicinity of the band gap in III-V compounds originate from *s*- and *p*-like atomic orbitals that hybridize (sp^3-hybridization) in the crystal yielding bonding and anti-bonding bands. At the high-symmetry points of the BZ these bands are characterized according to the symmetry group of these points. However, due to the spin-orbit interaction, the double group of the respective space point group T_d has to be considered. The spin-orbit interaction is of relativistic origin and scales with the atomic number, being considerable for the rather heavy Ga and As atoms.

All materials relevant to this work are direct band gap semiconductors, i.e., the valence and conduction band extrema occur at the center of the Brillouin zone, i.e., the Γ point. At this point, the bands originating from the sp^3-hybridization transform according to the Γ_6 (2-fold), Γ_7 (2-fold) and Γ_8(4-fold) irreducible representations of the double group of T_d. The Γ_6 bands have *s* character, while Γ_7 and Γ_8, split by the spin-orbit interaction, have *p* character. Usually only the bonding Γ_7 and Γ_8 bands are considered as valence bands, since the bonding Γ_6 is strongly bound, while the antibonding Γ_6 is considered as the conduction band, the other antibonding bands lying too high in energy. The lower lying Γ_7 valence band is the so-called (spin-orbit) split-off valence band, while the higher lying Γ_8 valence band splits in a heavy- and a light-hole

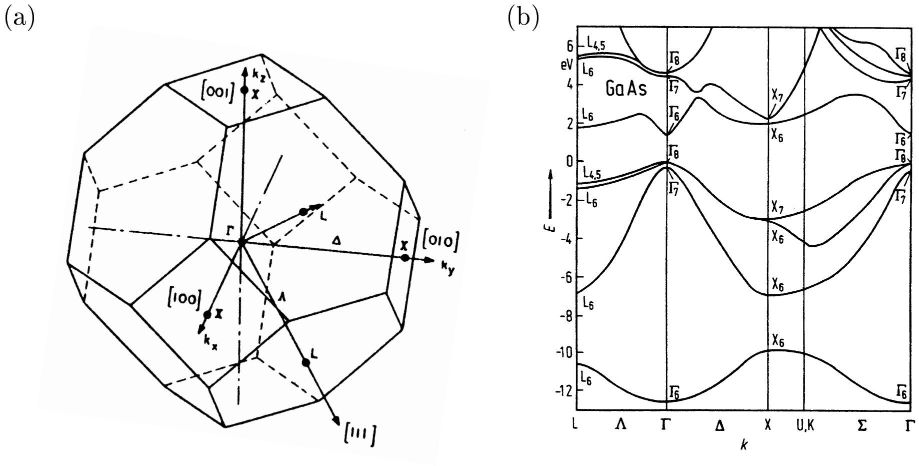

Figure 2.2: (a) First Brillouin zone of the face-centered cubic lattice [47]. (b) Band structure of bulk GaAs calculated with the empirical pseudopotential method (after [48]). Note the band structure in the vicinity of the Γpoint at the band gap (near $E \approx 0$), which dominates the electrical and optical properties.

valence band outside the Γ point (notice in Fig. 2.2(b) the visible splitting of the higher valence band along the ΓL direction).

From the point of view of the electronic structure, ternary or quaternary solid solutions between III-V or II-VI binary compounds are, strictly speaking, not crystalline: the potential felt by the electrons has no exact translational symmetry due to the random distribution of the atoms at the sites of the zinc-blende lattice. However, in the virtual crystal approximation the alloy is thought of as an ideal crystal of an effective material that gives the same periodic potential felt on the average by the electrons in the alloy. The material parameters are usually interpolated between the respective values for the binary crystals.

2.2 The $\vec{k} \cdot \vec{p}$ method

Band structures over the whole first Brillouin zone, like the one shown in Fig. 2.2b, are computed in large-scale numerical calculations using, e.g., the empirical or the ab-initio pseudopotential technique [48]. However, in semiconductors and, in general, materials where the free carrier concentration is much lower than the number of lattice sites, the mobile electrons and holes cluster near the extrema of the valence and conduction band, respectively. Hence, for most common physical situations such materials can be efficiently modeled if one knows the carrier dispersion within a comparatively narrow region around the band-structure extrema. Furthermore, external perturbations, like electric and magnetic fields or the complex potentials in heterostructures, can not be calculated efficiently or even at all with the pseudopotential technique. The same is true for carrier-phonon and carrier-carrier interactions, as well as compound particles, like excitons, trions, biexcitons, etc., since the pseudopotential technique is essentially a one-particle method. Thus, these materials have to be modeled in a simple context (although some progress has been achieved recently in the calculation of excitonic effects in large gap materials exhibiting strong excitonic effects [49, 50, 51]).

The $\vec{k}\cdot\vec{p}$ method is such a simple context for this purpose ([46], [52], [47], [53], [54])[1]. It is based on perturbation theory in the vicinity of band extrema and is described briefly below. In the mean-field approximation each valence electron experiences the same average potential $V_{crys}(\vec{r})$, the so called crystal potential, which usually has the same symmetries as the lattice. According to Blochs theorem, the eigenfunctions of the valence electrons can be chosen to be also eigenstates of the respective translational operator, i.e.,

$$\psi_{n\vec{k}}(\vec{r}) \;=\; e^{i\vec{k}\cdot\vec{r}}\,|n\vec{k}\rangle, \tag{2.1}$$

with $\vec{k}$ lying in the first Brillouin zone and n the band index. $|n\vec{k}\rangle$ has the crystal periodicity and is the material-specific part of the Bloch function. Using the above expression and neglecting the spin-orbit interaction, the Schrödinger equation describing the motion of the valence electrons becomes

$$\left(\frac{p^2}{2m_0} + V_{crys}(\vec{r}) + \frac{\hbar^2 k^2}{2m_0} + \frac{\hbar}{m_0}\vec{k}\cdot\vec{p}\right)|n\sigma\vec{k}\rangle \;=\; \mathcal{E}_{n\sigma}(\vec{k})|n\sigma\vec{k}\rangle, \tag{2.2}$$

where m_0 is the free electron mass. The Bloch functions $e^{i\vec{k}\cdot\vec{r}}|n\sigma\vec{k}\rangle$ are two-component spinors characterized by the spin quantum number σ. In order to take into account the spin-orbit interaction, the momentum operator $\vec{p}$ has to be replaced by

$$\vec{\pi} \;=\; \vec{p} + \frac{\hbar}{4m_0c^2}\vec{\sigma}\times\vec{\nabla}V_{crys}\,, \tag{2.3}$$

where $\vec{\sigma} = (\sigma_x, \sigma_y, \sigma_z)$ are the Pauli spin matrices.

In the vicinity of a band extremum (although this is not a precondition) like, e.g., the Γ point ($k = 0$), the $\vec{k}$-dependent terms in Eq. (2.2) are viewed as a perturbation, $\frac{\hbar}{m_0}\vec{k}\cdot\vec{p}$ being the perturbative term that couples different bands. For instance, for a non-degenerate band like the Γ_6 conduction band (neglecting for a moment the spin-orbit coupling) one gets up to second order in perturbation theory in the vicinity of the Γ point

$$\mathcal{E}_c(\vec{k}) \;\simeq\; \mathcal{E}_c(0) + \frac{\hbar}{m_0}\langle c\,0\,|\,\vec{k}\cdot\vec{p}\,|\,c\,0\rangle + \frac{\hbar^2k^2}{2m_0} + \frac{\hbar^2}{m_0^2}\sum_{n\neq c}\frac{\left|\langle n0\,|\,\vec{k}\cdot\vec{p}\,|\,c0\rangle\right|^2}{\mathcal{E}_c(0)-\mathcal{E}_n(0)}, \tag{2.4}$$

---

[1] Similar in spirit is the method of invariants, where the dispersion of the bands near high symmetry points of the Brillouin zone is parameterized using group theory [46]. However, the $\vec{k}\cdot\vec{p}$ method gives more insight to the relative importance and origin of the various contributions to the band structure.

and

$$|c\,\vec{k}\rangle \;\simeq\; |c\,0\rangle + \frac{\hbar}{m_0}\sum_{n\neq c}\frac{\langle c\,0\,|\,\vec{k}\cdot\vec{p}\,|\,n\,0\rangle}{\mathcal{E}_c(0)-\mathcal{E}_n(0)}. \tag{2.5}$$

The effective mass of the conduction band is then

$$\frac{1}{m_e} \;=\; \frac{1}{m_0} + \frac{2}{m_0^2 k^2}\sum_{n\neq c}\frac{\left|\langle n\,0\,|\,\vec{k}\cdot\vec{p}\,|\,c\,0\rangle\right|^2}{\mathcal{E}_c(0)-\mathcal{E}_n(0)}. \tag{2.6}$$

Usually, the positions of the band extrema coincide with high-symmetry points of the Brillouin zone and symmetry considerations can be applied to simplify the results of the perturbation theory. For example, for the Γ_8 valence band in the vicinity of the Γ point the k-linear terms vanish in centro-symmetric crystals. In zinc-blende crystals, the deviation from the inversion symmetry is usually small and these k-linear terms are often neglected. In non centro-symmetric crystals, spin-orbit interaction results generally in a complete lifting of degeneracy except at high-symmetry points of the Brillouin zone [46].

The momentum matrix elements and the energy gaps between the bands occurring in the $\vec{k}\cdot\vec{p}$ method are usually fitted to experiment.

2.3 The Luttinger Hamiltonian

In the $\vec{k}\cdot\vec{p}$ method for degenerate or quasi-degenerate bands, such as the valence bands at the Γ point for cubic and zinc-blende materials, perturbation theory for degenerate states is appropriate. The bandstructure in the vicinity of such points is, thus, described through a matrix Hamiltonian acting on the space of the (quasi-) degenerate band edge states.

In many cubic and zinc-blende materials, like, e.g., GaAs, ZnSe, CdTe, the splitting of the valence band at the center of the Brillouin zone due to the spin-orbit coupling and the band gap are large enough to consider the Γ_8 valence band as well separated. The $\vec{k}\cdot\vec{p}$ Hamiltonian describing the bandstructure of the top valence band for cubic materials is in the invariant form first introduced by Luttinger [55]

$$H_{Lut}(\vec{k}) \;=\; \frac{\hbar^2}{2m_0}\left\{\gamma_1 k^2 I - 2\gamma_2 J_i^2\left(k_i^2-\frac{k^2}{3}\right) - 2\gamma_3\{J_i,J_j\}k_ik_j\right\}, \tag{2.7}$$

where the Einstein summation convention has been used with $i,j=x,y,z$. In the above expression, I is the 4×4 unity matrix, J_i are the matrix representation of the total angular momentum $\vec{J}=\vec{L}+\vec{S}$ for $J=\frac{3}{2}$ [46], $\{J_i,J_j\}=J_iJ_j+J_jJ_i$, and $\gamma_1,\gamma_2,\gamma_3$ are the so-called Luttinger parameters. The Luttinger Hamiltonian is also appropriate for the top valence band in zinc-blende materials when the small k-linear terms originating from the inversion asymmetry of the lattice are neglected.

As was mentioned before, the valence band at the Γ point neglecting the spin-orbit coupling has p character, i.e., the band edge states transform like the functions X, Y, Z. Due to the spin-orbit coupling the valence band splits into the Γ_8 and Γ_7 bands that transform according to $J=\frac{3}{2}$ and $J=\frac{1}{2}$, respectively. In the $J=\frac{3}{2}$ basis with the coordinate system along the $\langle 100\rangle$ directions, the spin quantization axis being the z -axis and the phase convention originally used by Luttinger,

$$\begin{array}{rcl} |\,\frac{3}{2},+\frac{3}{2}> & = & \frac{1}{\sqrt{2}}(X+iY)\uparrow \\ |\,\frac{3}{2},+\frac{1}{2}> & = & \frac{i}{\sqrt{6}}\Big((X+iY)\downarrow -2Z\uparrow\Big) \\ |\,\frac{3}{2},-\frac{1}{2}> & = & \frac{1}{\sqrt{6}}\Big((X-iY)\uparrow +2Z\downarrow\Big) \\ |\,\frac{3}{2},-\frac{3}{2}> & = & \frac{i}{\sqrt{2}}(X-iY)\downarrow \end{array} , \tag{2.8}$$

the Luttinger Hamiltonian Eq. (2.7) takes the form

$$H_{Lutt} \quad = \quad -\frac{\hbar^2}{2m_0}\begin{pmatrix} \mathcal{P}+\mathcal{Q} & \mathcal{L} & \mathcal{M} & 0 \\ \mathcal{L}^\dagger & \mathcal{P}-\mathcal{Q} & 0 & \mathcal{M} \\ \mathcal{M}^\dagger & 0 & \mathcal{P}-\mathcal{Q} & -\mathcal{L} \\ 0 & \mathcal{M}^\dagger & -\mathcal{L}^\dagger & \mathcal{P}+\mathcal{Q} \end{pmatrix}, \tag{2.9}$$

where

$$\begin{array}{rclrcl} \mathcal{P} & = & \gamma_1 k^2 & \mathcal{Q} & = & \gamma_2(k^2-3k_z^2) \\ \mathcal{L} & = & -i\sqrt{3}\gamma_3 k_z k_- & \mathcal{M} & = & \sqrt{3}(\gamma_- k_+^2+\gamma_+ k_-^2) \end{array} , \tag{2.10}$$

and $k_\pm = k_x \pm i k_y$, $\gamma_\pm = \frac{1}{2}(\gamma_2 \pm \gamma_3)$.

The dispersion of the top valence bands obtained by diagonalizing the Luttinger Hamiltonian is given by

$$E_{hh,lh} = \frac{\hbar^2}{2m_0}\left(-\gamma_1 k^2 \pm 2\left[\gamma_2^2 k^4 + 3(\gamma_3^2-\gamma_2^2)(k_x^2 k_y^2 + c.p.)\right]^{1/2}\right), \tag{2.11}$$

where the upper sign is valid for the heavy hole and *c.p.* stands for cyclic permutation of the wavevector components.The Luttinger Hamiltonian predicts correctly the splitting of the Γ_8 valence band outside the Γ point in a heavy and a light hole band. The surfaces of constant energy of the heavy and light hole band are not ellipsoids (see Fig. 2.3); the valence bands are "warped".

An approximation, which is quite useful in bulk semiconductors, is the *spherical* one

$$H_{\Gamma_8}^{sph}(\vec{k}) = \frac{\hbar^2}{2m_0}\Big((\gamma_1+\tfrac{5}{2}\bar{\gamma})k^2 I - 2\bar{\gamma}\,(\vec{J}\cdot\vec{k})^2\Big) \tag{2.12}$$

with

$$\gamma_2 = \gamma_3 = \bar{\gamma} = \tfrac{1}{5}(2\gamma_2+3\gamma_3). \tag{2.13}$$

The spherical approximation gives spherical energy surfaces. However, the spherical approximation is quite crude for QW, where only two of the principal axes remain equivalent.

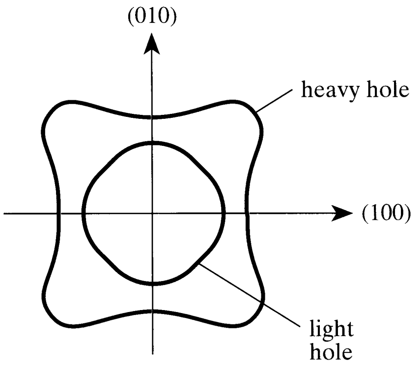

Figure 2.3: Constant energy lines of the Γ_8 valence bands for $k_z = 0$, from [47]. Crystal directions are noted like (100) instead of [100].

In cubic semiconductor systems with an external perturbation applied along one of the principal axes, as are QW grown on (001) surfaces, the *axial* approximation is extensively used. This approximation leads to the vanishing of the warping in the (001) plane. The warping of the valence bands in the xy-plane is due to the second term under the square root in Eq. (2.11) or equivalently to the term in $\mathcal{M}$, Eq. (2.10), proportional to γ_-. The axial approximation consists in setting $\gamma_- = 0$ in the term $\mathcal{M}$ of the original Luttinger Hamiltonian,

$$\mathcal{M} \;=\; \tfrac{\sqrt{3}}{2}\left(\gamma_2+\gamma_3\right)\left(k_x - ik_y\right)^2 . \tag{2.14}$$

An approximation to the Luttinger Hamiltonian often used in the literature is the *diagonal* approximation. This consists in neglecting all off-diagonal terms in the Luttinger Hamiltonian, i.e., $\mathcal{L} = \mathcal{M} = 0$; it gives correct results along the [001] direction, where the Luttinger Hamiltonian becomes diagonal. This approximation is characterized by a mass reversal effect: the heavy hole effective mass is larger than the light-hole mass in the z-direction but smaller in the perpendicular plane

$$m_{h,\|}^{diag} = \left(\gamma_1 \pm \gamma_2\right)^{-1} , \qquad m_{h,z}^{diag} = \left(\gamma_1 \mp 2\gamma_2\right)^{-1} , \tag{2.15}$$

the upper sign holding for the heavy hole.

In more accurate $\vec{k}\cdot\vec{p}$ descriptions of the bandstructure near the Γ point a larger number (up to 14, i.e., all the bands shown in Fig. 2.2(b) of band edge states is treated as quasi-degenerate, so that their coupling is taken exactly into account [56].

2.4 The envelope function approximation

Another big advantage of the $\vec{k}\cdot\vec{p}$ method, besides the efficient description of the band dispersions near extremal points, is the simplicity and versatility of the method in tackling a large class of external perturbations. External fields that are smooth enough are expected to affect the wavefunction of the charged particle only on scales much larger than the lattice constant. The wavefunction of the particle can then be expressed by products of the band edge states times slowly varying functions, the so called *envelopes.* The slowly varying external perturbation is acting predominantly only on the envelopes. External fields are considered smooth in this context, if they change little over distances of the order of the lattice constant and over time intervals of the order of $\Delta E/\hbar$, where ΔE is the typical band separation energy at the considered extremum. This is the well established envelope function approximation (EFA), known in the single-band case also as effective mass approximation. The resulting equations are simple since the explicit form of the band edge states in a lattice cell is not addressed.

To this class of perturbations belong the electric, magnetic and electromagnetic fields usually relevant in semiconductor devices as well as strain and interactions involving long-wavelength lattice phonons [52]. The effect of strain on the Γ_8 valence bands in terms of deformation potentials is to add new terms to the $\vec{k}\cdot\vec{p}$ matrix Hamiltonian [47]:

$$H^{str}_{\Gamma_8}(\vec{k}) = a\sum_i \epsilon_{ii} I - 3b\epsilon_{ii}\left(J_i^2 - \frac{J^2}{3}\right) - \sqrt{3}d\{J_i, J_j\}\epsilon_{ij}, \;\; i,j = x,y,z. \quad (2.16)$$

In the expressions above, $\epsilon_{i,j}, i,j = x,y,z$ are the components of the strain tensor and a, b, d deformation potentials of symmetry $\Gamma_1, \Gamma_3, \Gamma_4$, respectively.

Strain is usually present in heterostructures due to non-matching lattice constants of the constituent materials, like, e.g., in the II-VI QW discussed in Chap. 6, where the different lattice constants give rise, in a first approximation, to a uniaxial stress along [001] in the well material. For such a stress Eq. (2.16) reads

$$H^{str,[001]}_{\Gamma_8} = b\left(\epsilon_{zz} - \frac{\epsilon_{xx}+\epsilon_{yy}}{2}\right) diag\{-1,+1,-1,+1\}. \quad (2.17)$$

It is clear from the form of Eq. (2.17) that uniaxial strain along [001] leads to strain induced splitting of the heavy- and light-hole bands at the Γpoint.

2.5 Bulk Wannier excitons

Wannier excitons can be adequately described in the EFA. Such excitons extend over many elementary cells of the crystal (exciton Bohr-radius $a_B \approx 15$nm, large compared to the lattice constant $a_0 = 0.565$nm in GaAs) and have a binding energy much smaller than the band gap (exciton binding energy 4meV, small compared to the band gap of 1519meV for GaAs). The large extension of

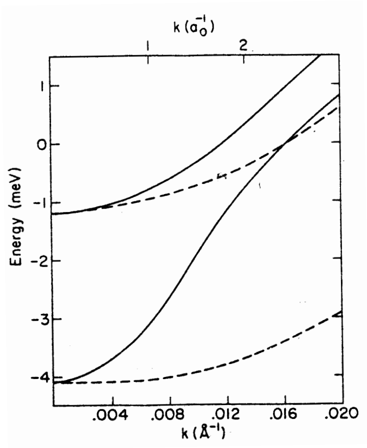

Figure 2.4: Exciton dispersion for the ground and first excited exciton states of bulk GaAs for momentum k along [111], from [57].

the excitons in semiconductor crystals is related to the predominately covalent nature of the binding of the atoms that results rather small band gaps and, hence, in an efficient screening of the Coulomb interaction.

Excitons of the Wannier type can carry momentum and have thus a dispersion. This momentum corresponds to the usual COM momentum known from classical mechanics. In the ideal case of a semiconductor with simple parabolic bands, the exciton dispersion is easily calculated using the well-known COM transformation, which reveals the complete separation of relative and COM motion. In real semiconductors, however, which are characterized by degenerate valence-band maxima, the complete decoupling of relative and translational motion of the electron-hole pair is not possible. This fact was first emphasized by Dresselhaus [58].

The degeneracy of the valence bands leads to new features in the exciton dispersion. Depending on the ratio of the average hole mass to the electron mass (the heavier particle dominates the COM motion) and on the mass difference of heavy- and light-holes, the exciton dispersion can be highly anharmonic and may even exhibit very different masses for different exciton states, leading to avoided crossings and mass-reversal effects [59, 57]. These effects are particularly strong for the direct-band-gap zinc-blende materials, where the electron and light-hole masses are much smaller than the heavy-hole mass. An example of such a highly anharmonic bulk exciton dispersion is shown in Fig. 2.4 for bulk GaAs.

As we will see in the progress of this work, the same physics determine the exciton dispersions in QW and QWR, where the anharmonicity of the exciton dispersion is considerably enhanced due to the rich band structure in two- and one-dimensional heterostructures.

Chapter 3

Excitons in Quantum Wells and Quantum Wires

The fabrication of low-dimensional semiconductor heterostructures has opened a whole range of exciting new perspectives in the development of novel devices and the investigation of quantum-mechanical effects. All electronic and optical properties of semiconductor devices depend upon the bandstructure, which can be tailored to a high degree in heterostructures since quantum size effects appear when carriers are subject to potentials on length scales comparable to the interatomic spacings.

The electronic bandstructure is modified using basically three closely related concepts: alloying of two or more semiconductors, use of heterostructures to benefit from quantum mechanical confinement effects, and use of built-in strain via lattice-mismatched epitaxy.

The spatial confinement has a large influence on the single-particle level. Due to the break down of the bulk translational symmetry along one (QW) or two (QWR) dimensions the bulk bands split in separate so called subbands, each of them showing individual dispersion features that depend strongly on the geometry and material composition of the heterostructure. The reduction of the translational symmetry lifts the degeneracy of the heavy- and light-hole bulk valence band at the center of the Brillouin zone; the resulting subband states are of pure heavy- or light-hole character at the Γpoint in QW, whereas in QWR there is heavy-light-hole mixing in the whole BZ. The lifting of the valence band degeneracy in heterostructures leads to the formation of heavy and light excitons.

The optical properties of low-dimensional semiconductor heterostructures, as quantum wells and quantum wires, are dominated by excitons, at least at low temperature. The confinement of the carriers along one or two spatial directions into regions comparable or smaller than the bulk exciton size enhances the effect of the electron-hole Coulomb interaction. This results in larger binding energies and oscillator strengths. As a consequence, excitons are observed in these structures even at room temperature.

In many heterostructure systems of interest like, e.g., GaAs/AlAs, InGaAs/-InP and ZnCdSe/ZnSeS, the exciton can be described in the envelope function approximation (Wannier exciton) due to its small bulk binding energy (e.g., 4meV for GaAs) or equivalently due to its large size ($\sim$ 15nm for GaAs), much larger than the lattice constant (0.565nm for GaAs). The EFA is a well-suited tool to study excitons in these geometries.

3.1 The envelope function approximation in heterostructures

With epitaxial techniques like metal organic chemical vapour deposition (MOCVD) or molecular beam epitaxy (MBE) one can achieve nowadays within a monolayer ($\sim$ 0.3nm) nearly abrupt interfaces between two different materials depending on material parameters and growth conditions. Thus, especially for the $\mathrm{Al}_x\mathrm{Ga}_{1-x}\mathrm{As}$ system, quantum wells as well as more complicated planar structures like superlattices can be fabricated today with interfaces of high quality. These structures are often well described with models assuming ideal abrupt interfaces.

In contrast, the fabrication of semiconductor heterostructures of lower dimensionality like QWR and quantum dots (QD) is still a relatively new technology and has not yet reached the degree of control possible today in 2D structures. However, even in QWR systems abrupt interfaces are often assumed in theoretical investigation since the complexity of these systems usually does not allow much further refinement. Heterostructures with abrupt interfaces or material composition variations on a scale much larger than the lattice constant are frequently investigated theoretically in the EFA.

While material composition variations on large scales can be easily integrated in the EFA as a slowly varying effective crystal potential, this is not obvious for abrupt interfaces, where the material composition changes on an atomic scale. Indeed, although the EFA is valid in the materials on either sides of the interface, the solutions on both sides have to be connected over the interface through some boundary conditions. A long discussion [60, 61, 62, 63, 64, ?, 65, 66, 67, 68, 69] on whether the EFA is justified in the presence of abrupt interfaces and which are the right boundary conditions has aroused in the literature. Different boundary conditions have been proposed based on various arguments like the hermiticity of the EFA Hamilton operator [69] (or equivalently the continuity of the probability flux) or based on more microscopic derivations of the EFA approximation [61, 62, 64, 66, 63]. However, the choice of the boundary conditions was found to have only minor effects on the single-particle dispersions, and these in turn are not expected to affect significantly the numerical solution of the exciton, which averages over a large area in $\vec{k}$-space. Meanwhile, a certain consensus seems to have been reached on using the simple symmetrized form of the kinetic operator (see below, Eq. (3.5)); they guarantee the continuity of the probability flux at the interfaces. In the literature only this symmetrized form of the kinetic operator was applied to the exciton problem in heterostructures.

In some EFA models so called "spurious solutions" [70] and "wing bands" [68] occur. These represent unphysical solutions (solutions far away from the center of the Brillouin zone, in the vicinity of which the EFA holds, usually outside the first BZ) that may dominate over the physical ones, e.g., during numerical integration of the resulting partial differential equations. These unphysical solutions are, in principle, due to the restriction to a finite number of basis functions in the expansion of the wavefunction in Bloch band edge states that inhibits the reproduction of the bandstructure periodicity [63, 65]. They are not to include in the required solution and are a problem only in conjunction with some numerical methods like integration of partial differential equations. In contrast, other methods like solution of integral equations using quadrature methods [71] have no problems in dealing with these since only long wavelength components are taken into account.

"Spurious solutions" and "wing bands" occur usually in models, where the conduction and the valence band (at least the light-hole valence band) are considered together as quasi-degenerate in the $\vec{k} \cdot \vec{p}$ expansion. This is not the case if the valence band is described in the Luttinger approximation and the conduction band in a single-band approximation. Even in other, more complicated models these unphysical solutions should not be a problem when solving the exciton with the methods applied in this work: a discretization method in $\vec{k}$-space(mesh around the Γpoint) or one in real space(a finite mesh size permits only certain discrete wavevectors within the first BZ). Thus, spurious solutions will be of no concern in the present work.

3.2 Excitons in quantum wells

The ability to fabricate low-dimensional semiconductor heterostructures, where electrons and holes can be strongly confined within small space regions, has given exciton research an important technological aspect. The motivation for exciton studies is based on interest in material characterization, pure physics, and optical information processing.

3.2.1 Theoretical model

In the envelope function approximation, the Wannier exciton is described by the Hamilton operator

$$H = H_e(\vec{r}_e) + H_h(\vec{r}_h) + V_{Coul}(\vec{r}_e - \vec{r}_h). \tag{3.1}$$

Therein, the single-particle operators $H_e(\vec{r}_e)$, $H_h(\vec{r}_h)$ describe the material-dependent bandstructure in the vicinity of the Γpoint of the respective particles and

$$V_{Coul}(\vec{r}_e - \vec{r}_h) = -\frac{e^2}{\epsilon} \frac{1}{\mid \vec{r}_e - \vec{r}_h \mid} I \tag{3.2}$$

stands for the attractive Coulomb potential. Since we will be considering only quantum wells grown in the [100] direction, the coordinate system is chosen, as usual, with the z-axis along the [100] direction; $\vec{r}_e = (x_e, y_e, z_e)\,, \vec{r}_h = (x_h, y_h, z_h)$ denote the space coordinates of electron and hole, respectively.

We have neglected in the Coulomb potential, Eq. (3.2), any effects of the spatial dependence of the dielectric function ϵ when going from the well to the barrier material (image charge effect). As known [25, 72], this dependence when taken into account enhances the exciton binding energy in $\mathrm{Al}_x\mathrm{Ga}_{1-x}\mathrm{As}$ QW since the dielectric constant in the barrier is smaller than in the well. However, this effect is not expected to contribute significantly to the exciton dispersion, since the dielectric mismatch is a purely electrostatic effect, which depends marginally on the amount of the wavefunction in the barriers. The enhancement of the exciton binding energy due to the image charge effect varies from about 1meV for wide wells to 2.5meV for narrow wells for GaAs/AlAs QW [28] and should be substantially smaller for the AlGaAs-systems considered here. The effect is larger for II-VI QW due to the smaller dielectric constants.

We have also neglected in Eq. (3.2) the exchange part of the Coulomb interaction. This leads in QW to a fine splitting of the exciton states at zero COM (<1meV for $\mathrm{Al}_x\mathrm{Ga}_{1-x}\mathrm{As}$ compared to 0.02meV for bulk GaAs) and a further smaller splitting (<0.1meV for $\mathrm{Al}_x\mathrm{Ga}_{1-x}\mathrm{As}$) for finite COM momentum Q [30]. These splittings are related to the further reduction of the symmetry due to the coupling of the spins of the two particles over the exchange part of the Coulomb interaction. The exchange splitting is expected to be larger for II-VI systems because of the smaller dielectric constant and smaller Bohr radius.

For the materials considered, the bulk conduction band is to a good approximation parabolic [52]; anharmonicities in the conduction band arise mainly through the interaction with the light and split-off valence bands, which is small due to the relatively large band gap. The small anharmonicity of the bulk conduction band leads to a small nonparabolicity of the conduction subbands in $\mathrm{Al}_x\mathrm{Ga}_{1-x}\mathrm{As}$ QW [73, 25, 60]. We ignore it, and describe the electron, henceforth, in the spherical single-particle approximation by the Hamilton operator

$$H_e(z_e) \quad = \quad \left(-\frac{\hbar^2}{2m_e}(\partial^2_{x_e} + \partial^2_{y_e} + \partial^2_{z_e}) + V_c(z_e) \right) I. \qquad (3.3)$$

The offset $V_c(z_e)$ accounts for the spatial dependence of the conduction band edge; $m_e(z_e)$ stands for the effective electron mass.

As already mentioned in Sect. 2.3, for many zinc-blende semiconductors the splitting of the valence band at the center of the Brillouin zone due to the spin-orbit coupling is large enough (341meV for bulk GaAs) to not include it explicitly in the description of the Γ_8 valence band. This is a reasonable approximation for states near the valence band edge. The coupling to the other bands need then be taken only implicitly into account, via appropriate choice of the $\vec{k} \cdot \vec{p}$ parameters. In addition, the valence band warping can be safely neglected for small Q values since the exciton wavefunction averages over all in-plane momentum directions. The bandstructure of the Γ_8 valence band is in this case adequately described by the Luttinger Hamiltonian, Eq. (2.9, 2.10),

$$H_h \;=\; H_{Lutt}(z_h) + V_v(z_h)\, I \;, \tag{3.4}$$

where $V_v(z_h)$ accounts for the spatial dependence of the Γ_8 valence band edge. The Luttinger parameters $\gamma_1(z_h), \gamma_2(z_h), \gamma_3(z_h)$, the electron mass $m_e(z_e)$, as well as the offsets $V_v(z_h)$, $V_c(z_e)$ are piecewise constant functions of z_e, z_h. We will use for all further QW calculations the axial approximation, because it simplifies considerably numerical calculations of exciton in momentum space. We remind that, in contrast to the axial approximation, the spherical approximation does not even give the right energies for the subbands at the Γpoint.

In the single-particle Hamilton operators for the electron and hole, Eq. (3.3,3.4), we have neglected all terms that originate from the small inversion asymmetry of the zinc-blende bulk materials [46, 71]. We also neglect asymmetry terms that have their origin at the additional microscopic collapse of the inversion asymmetry at the interfaces for zinc-blende materials [74, 75]. Such terms would lead to a small coupling of the heavy- and light-hole bands at the Γpoint as well as the occurrence of the band extrema slightly off the Γpoint. However, in symmetric Type I QW the inversion symmetry, although locally broken at every interface, is preserved for the whole structure due to the presence of a second interface mirror-symmetrical to the first one.

To ensure that the kinetic operators remain Hermitian in the presence of interfaces, we use the symmetric substitutions

$$\gamma\,\partial_i \rightarrow (\partial_i\,\gamma + \gamma\,\partial_i)/2, \;\; \gamma\,\partial^2_{ij} \rightarrow (\partial_i\,\gamma\,\partial_j + \partial_j\,\gamma\,\partial_i)/2, \;\;\; i,j = x,y,z \tag{3.5}$$

where γ stands for some material parameter. These substitutions ensure the continuity of the probability current.

The quantization axis of the electron spin and of the hole angular momentum J is taken along the growth direction; the valence band edge states have been defined in Sect. (2.8). With the above approximations the electron spin is of no relevance and will be kept fixed at $s_e = +1/2$.

The Hamilton operator (3.1) acts with these approximations on a four-component envelope function in the product basis of the conduction and valence band edge states $\left\{|\tfrac{3}{2}\, m_J\rangle_v\, |\tfrac{1}{2}\, +\, \tfrac{1}{2}\rangle_c\,\right\}$, where the hole spin projection attains values of $m_J = +\frac{3}{2}, +\frac{1}{2}, -\frac{1}{2}, -\frac{3}{2}$.

The in-plane COM momentum operator $\vec{Q} = -i\hbar(\vec{\nabla}_{e_\parallel} + \vec{\nabla}_{h_\parallel})$ is a constant of motion because the interaction term (3.2) depends only on the relative distance of the two particles [76]. Consequently, the wavefunction factorizes into

$$\Psi^{\vec{Q};\,a}(\vec{r}_e, \vec{r}_h) \;=\; \frac{e^{-i\vec{Q}\cdot\vec{R}}}{2\pi}\, \sum_{m_J} \Psi^{\vec{Q};\,a}_{m_J}(z_e, z_h, \vec{\rho})\; |\; \tfrac{3}{2}\; m_J\rangle_v \;\; |\; \tfrac{1}{2}\, \tfrac{1}{2}\rangle_c\, , \tag{3.6}$$

where $\vec{\rho} = \vec{r}_{e_\parallel} - \vec{r}_{h_\parallel}$ is the in-plane particle distance, $\vec{R}$ the COM space coordinate canonically conjugate to $\vec{Q}$, and a stands for the remaining quantum numbers.

The COM space coordinate $\vec{R}$ in (3.6) is not unambiguously defined because of the anharmonic dispersions of the constituent particles [58]. The COM transformation must be linear in order to preserve the commutation relations and has in general the form

$$\begin{array}{rclcrcl} \vec{\rho} & = & \vec{r}_{e_\parallel} - \vec{r}_{h_\parallel} & \qquad & \vec{Q} & = & -i\hbar\left(\vec{\nabla}_{e_\parallel} + \vec{\nabla}_{h_\parallel}\right) \\ \vec{R} & = & \boldsymbol{\beta}\,\vec{r}_{e_\parallel} + (\mathbf{1} - \boldsymbol{\beta})\,\vec{r}_{h_\parallel} & & \vec{k} & = & -i\hbar\left((\mathbf{1} - \boldsymbol{\beta})\,\vec{\nabla}_{e_\parallel} - \boldsymbol{\beta}\,\vec{\nabla}_{h_\parallel}\right) \end{array} \tag{3.7}$$

where the bold face type indicates that $\boldsymbol{\beta}$ is in general a spinor [77]. In the parabolic case, the free parameter(s) $\boldsymbol{\beta}$ is taken as the scalar

$$\beta_{parab} = \frac{m_e}{m_e + m_h} \tag{3.8}$$

in order that relative and COM motion completely decouple. For bulk excitons, $\boldsymbol{\beta}$ has been considered in the literature as a scalar [57], a tensor in real space [57] or even a spinor [77]. We will return later on to the problem of an appropriate choice for $\boldsymbol{\beta}$ and the COM coordinate $\vec{R}$.

Inserting Eq. (3.6, 3.7) into the eigenvalue problem of Eq. (3.1- 3.4) gives a system of four coupled partial differential equations in a four dimensional configuration space $(z_e,\, z_h,\, \vec{\rho})$.

Specular reflection with respect to the xy plane, σ_{xy}, is also a symmetry element for symmetric QW. The exciton can be characterized consequently by the parity $P = \pm 1$. Taking into account the electron spin degeneracy, each exciton state is at least fourfold degenerate in symmetric QW. It can be shown in a similar way as has been done for the hole subband states in Ref. [78] that the operator $R_\pi T$, with the rotation by π about the z axis, R_π, and time-reversal, T, transforms between the degenerate states of different parity and opposite electron spin. If one combines this operator with the Pauli-matrix σ_y^e, which flips only the electron spin, we have apart from an overall phase

$$\begin{aligned} \Psi^{\vec{Q};\,-Pa}(\vec{r}_e, \vec{r}_h) &= \left(\sigma_y^e\, R_\pi\, T\right)\, \Psi^{\vec{Q};\,Pa}(\vec{r}_e, \vec{r}_h) \\ &= \frac{e^{-i\vec{Q}\cdot\vec{R}}}{2\pi} \sum_{m_J} \Psi_{m_J}^{\vec{Q};\,Pa\,*}(z_e, z_h, -\vec{\rho})\, \mid \tfrac{3}{2} \;\; -m_J\rangle_v \;\; \mid \tfrac{1}{2} \; +\tfrac{1}{2}\rangle_c \,. \end{aligned} \tag{3.9}$$

Comparing (3.6) with (3.9), we find

$$\Psi_{m_J}^{\vec{Q};\,-Pa}(z_e, z_h, \vec{\rho}) = \Psi_{-m_J}^{\vec{Q};\,Pa\,*}(z_e, z_h, -\vec{\rho})\,. \tag{3.10}$$

That is, the state of opposite parity degenerate with some state of definite parity is obtained by inverting the order of the spin components of the exciton envelope, complex conjugating, and changing the sign of the in-plane relative coordinate. Thus, changing the multiband exciton parity with fixed electron spin in symmetric QW corresponds to flipping the hole spin in the single-band exciton case. In the axial approximation and for $Q = 0$, the different angular momentum components decouple [79], and changing the sign of $\vec{\rho}$ in Eq. (3.10) just changes the sign of two spin components leaving the other two unchanged; this holds no longer at $Q \neq 0$.

We have so far introduced the theoretical model for the description of excitons in QW used in this work. The theoretical description of excitons in QWR goes, in principle, along the same lines with minor modifications introduced in the next section.

3.3 Excitons in V-groove quantum wires

Today, there exists a number of technologically important QWR systems like V-groove [80], T-shaped [81, 2], etched mesa structures [82, 83], or wires grown along natural step-bunched surface steps [84, 85] or etched steps [86]. We will study, as an example, so called V-groove QWR, which are particular promising for device applications. They result from self-assembled growth under MOCVD or MBE on a substrate into which V-shaped grooves were etched. Alternating deposition of GaAs and AlGaAs [87, 80] or InGaAs and InP [88, 89] leads to stacks of V-shaped wells and barriers, like the one shown in Fig. 3.1. Due to different growth rates and lateral transport, crescent-shaped thicker well regions develop at the bottom, which act as QWR. The well regions on the side walls will be referred to as side quantum well (S-QW), henceforth. The stack of V-groove QWR is found to be connected by a central region of increased Ga concentration, which will be referred to as vertical quantum well (V-QW).

The particular sample we are going to investigate has been grown by MOCVD on grooved (001)-GaAs substrates with the wires oriented along the $[1\bar{1}0]$ direction [91]. The periodic corrugations were made by holographic photolithography and wet chemical etching. A cross-sectional view of the QWR heterostructure obtained in transmission electron microscopy (TEM) is shown in Fig. 3.2. As is clearly seen in this cross-section micrograph, the confining potentials show no strict symmetry. Only an approximate specular reflection symmetry with respect to the xz-plane exists. The stronger narrowing of the S-QW on the right rather than on the left side of the figure is partly an artefact of the concrete observation technique used [91]; this will, however, have only marginal influence on the calculated physical quantities.

3.3.1 Theoretical model

For the description of the Wannier exciton in a QWR, we use practically the same theoretical model as the one described in Sect. 3.2.1 for QW. We choose the coordinate system $x||[1\bar{1}0]$, $y||[110]$, $z||[001]$, i.e., the wire axis lies along the x-axis, the stronger confinement is along the z-axis and the weaker confinement is along the y-axis. Since we have two confinement directions (y, z) for the QWR, the Hamilton operator describing a Wannier exciton in this system is again of the form Eq. (3.1) with the same Coulomb interaction Eq. (3.2) and, in principle, the same single-particle operators (3.3), (3.4) except for the now two-dimensional confining potentials $V_c(\vec{\rho}_e)$, $V_v(\vec{\rho}_h)$ $(with\vec{\rho}_{e,h} = (x_{e,h}, y_{e,h}))$. and a

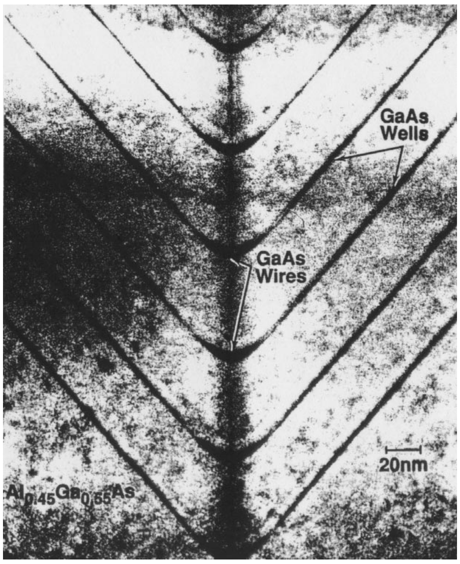

Figure 3.1: Transmission electron micrograph of the cross-section of a vertical quantum wire structure [90]. The darker the shading is, the higher is the Ga concentration. Note the vertical region of increased Ga concentration (VQW) joining the actual wire regions.

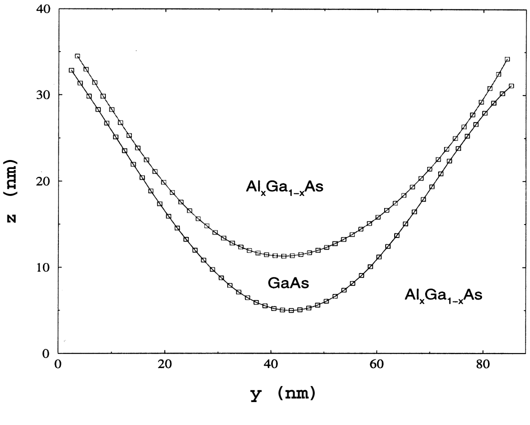

Figure 3.2: Cross-sectional view of a particular V-groove QWR sample obtained in transmission electron microscopy (TEM) [92, 91].

transformation of the Luttinger Hamiltonian to account for the new rotated real space coordinate system.[1] The quantization axis of the electron spin and the hole angular momentum remain along the z-axis, but in order to achieve formal simplicity, i.e., to get rid of phase factors arising in the Luttinger Hamiltonian because of the coordinate transformation, we rotate the spin basis around the quantization axis by an angle of $\frac{\pi}{4}$.[2] In addition, we do not invoke the axial approximation in the description of the valence band structure, since, in contrast to the QW case, it leads to no benefit during the numerical solution of the exciton problem. That is, we keep in the Luttinger Hamiltonian, Eq. (2.9), the full $\mathcal{M}$ term.

Due to the irregular shape of the V-groove QWR, there are no symmetries in real space left. Still, the electron spin remains decoupled due to the neglect of the exchange part of the Coulomb interaction and of any spin-orbit terms in the conduction band description. The QWR exciton states are, therefore, at least twofold degenerate. In the following, we will pin the electron spin at the value of $s_e = +1/2$.

Again, we introduce a COM transformation similar to Eq. (3.7)

$$\begin{aligned} \chi &= x_e - x_h & X &= \boldsymbol{\beta} x_e + (\mathbf{1} - \boldsymbol{\beta}) x_h \\ k &= -i\hbar\left((\mathbf{1} - \boldsymbol{\beta})\partial_{x_e} - \boldsymbol{\beta}\partial_{x_h}\right) & Q &= -i\hbar\left(\partial_{x_e} + \partial_{x_h}\right) . \end{aligned} \tag{3.11}$$

Again, the COM momentum Q is a constant of motion because the interaction term (3.2) depends only on the relative distance of the two particles and the wavefunction factorizes into

$$\Psi^{Q;\,a}(\vec{r}_e, \vec{r}_h) = \frac{e^{-iQX}}{\sqrt{2\pi}} \sum_{m_J} \Psi^{Q;\,a}_{m_J}(\vec{\rho}_e, \vec{\rho}_h, \chi) \mid \tfrac{3}{2}\; m_J\rangle_v \;\; \mid \tfrac{1}{2}\,\tfrac{1}{2}\rangle_c \,, \tag{3.12}$$

where a stands for the remaining quantum numbers. The numerical determination of the exciton eigenstates in such a QWR involves the solution of four coupled partial differential equations in a five dimensional configuration space $(\vec{\rho}_e,\, \vec{\rho}_h,\, z_e - z_h)$.

---

[1] Writing the kinetic operator as $H = \sum_{i,j} \partial_i\, \boldsymbol{h}_{ij}\, \partial_j$, where the bold face indicates that $\boldsymbol{h}$ is in general a spinor, then in a rotated coordinate system $x'_i = \sum_j g_{ij}\, x_j$, the Hamiltonian H is given through

$$H' \quad = \quad \sum\nolimits_{l,m} \partial'_l \left(\sum\nolimits_{i,j} g_{li}\, \boldsymbol{h}_{ij}\, g_{mj} \right) \partial'_m \quad .$$

For the rotation considered in the text it is

$$g \quad = \quad \tfrac{1}{\sqrt{2}} \begin{pmatrix} 1 & -1 & 0 \\ 1 & 1 & 0 \\ 0 & 0 & \sqrt{2} \end{pmatrix} \quad .$$

[2] The rotation matrix for this transformation in the $J = \frac{3}{2}$ base is

$$\boldsymbol{g} = diag \left\{ e^{i(+\frac{3}{2})\frac{\pi}{4}}, e^{i(+\frac{1}{2})\frac{\pi}{4}}, e^{i(-\frac{1}{2})\frac{\pi}{4}}, e^{i(-\frac{3}{2})\frac{\pi}{4}} \right\} .$$

Every spinor in the kinetic operator transforms according to $\boldsymbol{h}' = \boldsymbol{g}^{-1}\, \boldsymbol{h}\, \boldsymbol{g}$.

Chapter 4

Optimizing the Center-of-Mass Transformation

The COM transformation is well known from classical mechanics (rigid solid, planetary Kepler model) and quantum mechanics (hydrogen atom). It is used to simplify the equations of motion by separating "internal" and "external" degrees of freedom and is related to translational invariance along (some) space coordinates.

In the ideal case of a semiconductor with parabolic bands the exciton dispersion is easily found using the COM transformation. However, real semiconductors are characterized by degenerate valence band maxima and non-parabolic dispersions. Dresselhaus [58] was the first to point out the absence of a well-defined COM transformation due to this degeneracy.

Altarelli and Lipari [57] calculated the exciton COM dispersion for direct- and indirect-gap bulk semiconductors. They demonstrated that the ambiguity in the choice of the COM transformation can be used to achieve formal simplicity or optimal numerical convergence. However, they did not manage to find an algorithm that would give the COM transformation for an optimal numerical convergence other than the trivial trial and error method.

Previous to our work [32], there have been just two publications where numerical multiband exciton dispersion in quantum wells were calculated: in Ref. [30] $\beta = 1$ (in the parabolic case: $m_e = \infty$) was taken in order to keep the form factors (see below, Eq. (5.7)) Q-independent, and in Ref. [31] no particular choice or handling of β is mentioned. In analytic expressions, usually the symmetric (in the parabolic case: $m_e = m_h$) value $\beta = 1/2$ is taken [71]. In the following sections, we describe two more deterministic and systematic methods for the COM optimization introduced in our recent papers, Ref. [32, 33].

4.1 Exciton dispersion and center-of-mass transformation

The effect of the choice of β becomes clear when one evaluates Eq. (3.7) for two different values β, $\beta' = \beta + \Delta\beta$ giving $\vec{R}' = \vec{R} + \Delta\beta\,\vec{\rho}$, $\vec{k}' = \vec{k} - \Delta\beta\,\vec{Q}$. Clearly, β moves artificially part of the plane wave of the COM motion into the relative part of the exciton in real space, see Eq. (3.6), or, equivalently, it shifts the relative part of the wavefunction in $\vec{k}$-space. A good choice of β, in the sense of better numerical convergence, as in the parabolic case (3.8), keeps the relative part of the exciton in real space as smooth as possible or, equivalently, pins the relative part of the wavefunction in $\vec{k}$-space to the origin. The relevance of the choice of β for the numerical convergence is illustrated in Fig. 4.1. In the appropriate COM coordinate system the ground state exciton in the case of simple parabolic bands is described using an angular decomposition with one component ($\ell = 0$), whereas in any other COM coordinate system the wavefunction appears shifted to the new origin and takes an infinite number of angular momentum components to be described exactly.[1]

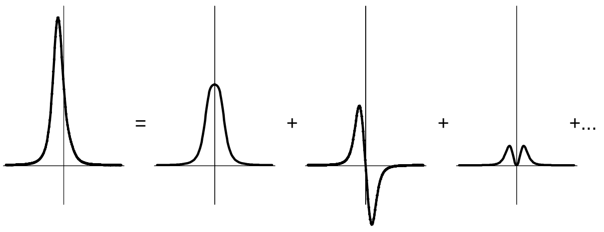

Figure 4.1: Illustration of the angular decomposition of a shifted 2D $1s$-exciton wavefunction in momentum space along the shift direction (see footnote 1). An infinite number of angular momentum components are needed to describe the shift.

---

[1] The angular decomposition of a shifted 2D $1s$-exciton wavefunction in $\vec{k}$-space $\phi_{1s}^{2D}(k) = \sqrt{\frac{2a_B^2}{\pi}}\left(1+(a_Bk)^2\right)^{-3/2}$ is given by

$$\phi_{1s}^{2D}\left(\vec{k}+\vec{\Delta}\right) = \phi_{1s}^{2D}(k)\sum_{\ell=0}^{\infty} c_\ell(k,\Delta)\,\cos\ell\theta\,,$$

with coefficients c_ℓ that can be obtained analytically

$$c_\ell(k,\Delta) = \frac{2}{(1+\delta_{\ell 0})\pi}\sum_{\mu=0}^{\ell}(-1)^\mu\binom{2\ell}{2\mu}\,B\left(\mu+\frac{1}{2},\ell-\mu+\frac{1}{2}\right)$$
$$\times F\left(\ell-\mu+\frac{1}{2},\frac{1}{2};\ell+1,\frac{-4a_B^2k\Delta}{1+a_B^2(k-\Delta)^2}\right),$$

where B is the Bernoulli function and F the hypergeometric function [93]. The x-axis is taken along $\vec{\Delta}$.

As already mentioned in Sect. 3.2.1, the optimal COM transformation in the case of simple parabolic bands is the one with the scalar value of $\beta = m_e/(m_e + m_h)$. For this value of β the relative and COM motion completely separate; hence, the numerical exciton dispersion is calculated to the same accuracy at all values of Q.

In real semiconductors, complete decoupling of relative and COM part of the exciton motion is not possible. Still, common sense implies, that, however strong the nonparabolicity of the underlying single-particle dispersions is, some "optimal" COM transformation exists corresponding to some "average" mass of the constituent particles.

4.2 Separation ansatz

We introduced in Ref. [32] a first quasi-analytical method for determining the optimal choice of the scalar β. It is motivated by the fact that in the parabolic case the correct COM transformation decouples the relative motion and COM motion completely. One can try to find the choice of β that decouples "as much as possible". To quantify this, we apply in Eq. (3.1) the general β-dependent COM-transformation (3.7) and integrate out the COM space coordinate $\vec{R}$. The resulting equation is the eigenproblem of the reduced Hamilton operator $H(Q)$ acting in the relative space $\{\vec{\rho}, z_e, z_h\}$, which depends parametrically on Q. We then separate the Q-dependent terms from the rest

$$H(Q) \quad = \quad H^{(0)} + H^{(1)}(\beta)\, Q + H^{(2)}(\beta)\, Q^2, \tag{4.1}$$

and view these as a perturbation acting on the $Q = 0$ relative exciton wavefunction. The explicit form of the operators in Eq. (4.1) is

$$H^{(n)}(\beta) = (1-\beta)^n\, H_e^{(n)} + \beta^n H_h^{(n)},\ n = 0, 1, 2 \tag{4.2}$$

with

$$H_{e,h}^{(n)} = \frac{1}{n!} \left(\hat{Q} \cdot \vec{\nabla}_{k_{e,h}} \right)^n H_{e,h} \left(\vec{k}_{e,h} \right), \tag{4.3}$$

and $\vec{Q} = Q\hat{Q}$.

The kinetic mass of the groundstate exciton g is given in second order perturbation theory by

$$\frac{\hbar^2}{2M_g^X} = \langle\, g \mid H^{(2)}(\beta) \mid g\,\rangle + \sum_{a \neq g} \frac{\mid \langle a \mid H^{(1)}(\beta) \mid g \rangle \mid^2}{E_g^X(0) - E_a^X(0)}. \tag{4.4}$$

Of course, the exciton mass does not depend on the choice of the coordinate system, that is, on β. Minimizing the first order contribution in Eq. (4.4) and thereby minimizing the absolute value of the strictly negative contribution of the higher states to the ground state dispersion (the avoided crossings with higher states lead to a flatter dispersion according to Ritz's variational principle) leads to the analytical result

$$\beta \;=\; \frac{\langle g \mid H_h^{(2)} \mid g \rangle}{\langle g \mid H_e^{(2)} \quad + H_h^{(2)} \mid g \rangle} \; . \tag{4.5}$$

Again, the matrices $H_{e,h}^{(2)}$ are simply the material-dependent coefficients of the quadratic terms for $\vec{k}_e = \vec{k}_h = \vec{Q}$ in Eq. (3.3) and (3.4), respectively [32].

In the procedure described above we neglected the second order contribution of the perturbation term $H^{(1)}$ and kept only the first order contribution of the perturbation term $H^{(2)}$ to the ground state dispersion, that is, we optimized β while keeping the ground state of the reduced Hamilton operator $H(Q)$ unchanged. Transforming back into full space, this is equivalent to the Ansatz

$$\Psi^{\vec{Q};g}(\vec{r}_e, \vec{r}_h) \;=\; e^{-i\vec{Q}\cdot\vec{R}}\, \Psi^{0;g}(\vec{r}_e, \vec{r}_h) \;, \tag{4.6}$$

which is simply the usual separation Ansatz.

The explicit form of Eq. (4.4) with the contributions from the higher states dropped and β from Eq. (4.5) suggests to *define* COM-related, effective masses $m_{e,h}^*$ for electron and hole

$$1/m_{e,h}^* = \frac{2}{\hbar^2}\langle g \mid H_{e,h}^{(2)} \mid g \rangle \qquad \text{satisfying} \qquad M_g^X = m_e^* + m_h^* . \tag{4.7}$$

Eq. (4.5,4.6,4.7) give the correct results in the limit of parabolic bands.

Numerical results show that the masses obtained from (4.7) tend to be too small. Nevertheless, the obtained values for β in [32], [94] were quite reasonable because of the much heavier hole mass. If one actually calculates the contributions of the higher exciton states to M_g^X in (4.4) (which are dropped in (4.7)), one finds that the only important correction comes from the coupling to the $LH_1C_1 - 1s$-like state. Taking in Eq. (4.4) this single correction term into account gives practically the exact curvature of the exciton groundstate dispersion at $Q = 0$.

4.3 Shifted exciton-envelope Ansatz

The above procedure is not the best for determining the optimal value of β for the problems relevant to this work. We tried therein, in principle, to eliminate as far as possible the part of the kinetic operator that couples relative and COM motion, the term $H^{(1)}Q$ in Eq. (4.1). However, for the semiconductors with degenerate valence bands and relatively small exciton binding energies this is not appropriate, as this coupling remains substantial for all values of β.

It may, therefore, be more advantageous to work in a subband representation, where this coupling has already been taken into account at least on the single-particle level. We expand, thus, the exciton wavefunction in the product basis of the electron $|n_e\vec{k}_e\rangle$ and hole subband states $|n_h\vec{k}_h\rangle$ combined in such a way to give the right momentum

$$\Psi^{\vec{Q};g}(\vec{r}_e,\vec{r}_h) = \sum_{n_e n_h} \int d\vec{k}\, \varphi^{\vec{Q};g}_{n_e n_h}(\vec{k})\, |n_h\, \vec{k}-(1-\beta)\vec{Q}\rangle\, |n_e\, \vec{k}+\beta\vec{Q}\rangle\,. \tag{4.8}$$

We remark, that the general COM transformation, Eq. (3.7), gives

$$k_e = k + \beta Q\ ,\ \ k_h = k - (1-\beta)Q\,. \tag{4.9}$$

Note also, that the plane waves of the single-particle states combine to give the right plane wave for the total COM momentum, since $\vec{k}_e\vec{\rho}_e - \vec{k}_h\vec{\rho}_h = \vec{k}\vec{\rho} + \vec{Q}\vec{R}$. The Hamilton operator takes the form

$$H = \Big(\mathcal{E}_{n_e}(\vec{k}+\beta\vec{Q}) + \mathcal{E}_{n_h}(\vec{k}-(1-\beta)\vec{Q})\Big)\, \delta(\vec{k}-\vec{k}')\delta_{\substack{n_e n_h \\ n'_e n'_h}} + V^{\vec{Q}}_{\substack{n'_e n'_h \\ n_e n_h}}(\vec{k},\vec{k}'), \tag{4.10}$$

with the interaction

$$\begin{aligned} &V^{\vec{Q}}_{\substack{n'_e n'_h \\ n_e n_h}}(\vec{k},\vec{k}') = \\ &\quad \langle n_e\, \vec{k}+\beta\vec{Q}|\langle n_h\, \vec{k}-(1-\beta)\vec{Q}|\, V_{Coul}(|\vec{k}-\vec{k}'|)\, |n'_h\, \vec{k}'-(1-\beta)\vec{Q}\rangle|n'_e\, \vec{k}'+\beta\vec{Q}\rangle\,, \end{aligned} \tag{4.11}$$

where

$$V_{Coul}(q) = -\frac{1}{2\pi}\frac{e^2}{\epsilon}\frac{e^{-|z_e-z_h|q}}{q} \tag{4.12}$$

is the 2D Fourier transform of the Coulomb potential.

The Q-dependence enters the wavefunction Eq. (4.8): (i) through the need to appropriately combine the subband states to get the right Q ($\vec{Q} = \vec{k}_e - \vec{k}_h$) and (ii) through the need for the envelope to adjust for the anharmonicities in the dispersions. In the perturbation approach described above, we tried to find a COM transformation that keeps the *whole wavefunction* as much as possible unchanged for small Q values. However, once the single-particle problem is solved, the Q-dependence due to the combination of the subband states in Eq. (4.8) is explicitly known. Therefore, a better Ansatz for the wavefunction would be to try to find a COM transformation that keeps the *envelopes* as much unchanged as possible; that is

$$\Psi^{\vec{Q};g}(\vec{r}_e,\vec{r}_h) = \sum_{n_e n_h} \int d\vec{k}\, \varphi^{0;g}_{n_e n_h}(\vec{k})\, |n_h\, \vec{k}-(1-\beta)\vec{Q}\rangle\, |n_e\, \vec{k}+\beta\vec{Q}\rangle. \tag{4.13}$$

The expectation value of Eq. (4.10) with Eq. (4.13) can then be minimized with respect to β. In order to keep the notation simple we switch temporarily to the independent subband approximation, which consists in keeping in Eq. (4.13) only one subband combination, and drop all subband indices and respective sums. The groundstate energy then reads

$$\begin{aligned} \langle g\,|H|\,g\rangle = \mathcal{E}_g(\beta,\vec{Q}) = &\int d\vec{k}\, |\varphi^{0;g}(\vec{k})|^2\, \Big(\mathcal{E}_e(\vec{k}+\beta\vec{Q}) + \mathcal{E}_h(\vec{k}-(1-\beta)\vec{Q})\Big) \\ &+ \iint d\vec{k}\, d\vec{k}'\varphi^{0;g^*}(\vec{k})\varphi^{0;g}(\vec{k}')\, V_{int}(\vec{k},\vec{k}';\beta,\vec{Q}). \end{aligned} \tag{4.14}$$

Making a Taylor expansion of the kinetic terms for $Q \to 0$ and neglecting any $\vec{Q}$ dependence of the potential energy, we arrive at

$$\begin{aligned}\mathcal{E}_g(\beta,\vec{Q}) - \mathcal{E}_g(0) \;\; &\simeq \;\; Q^2 \int d\vec{k}\, |\varphi^{0;g}(\vec{k})|^2 \\ &\quad \times \left(\beta^2 \left(\hat{Q}.\vec{\nabla}\right)^2 \mathcal{E}_e(\vec{k}) + (1-\beta)^2 \left(\hat{Q}.\vec{\nabla}\right)^2 \mathcal{E}_h(\vec{k}) \right). \end{aligned} \tag{4.15}$$

The first derivatives, being odd functions of k (since the single-particle dispersions themselves are even functions), do not contribute. Minimizing this expression with respect to β in the spirit of Ritz's variational principle, we easily obtain the optimized value

$$\beta_0 = \frac{\displaystyle\int d\vec{k}\, |\, \varphi^{0;\, g}(\vec{k})\, |^2\, (\hat{Q}\cdot\vec{\nabla})^2 \mathcal{E}_h(\vec{k})}{\displaystyle\int d\vec{k}\, |\, \varphi^{0;\, g}(\vec{k})\, |^2\, (\hat{Q}\cdot\vec{\nabla})^2 (\mathcal{E}_e(\vec{k}) + \mathcal{E}_h(\vec{k}))}\,. \tag{4.16}$$

Beyond the independent subband approximation, the above expression takes the form

$$\beta_0 = \frac{\displaystyle\sum_{n_e n_h} \int d\vec{k}\, |\, \varphi^{0;\, g}_{n_e n_h}(\vec{k})\, |^2\, (\hat{Q}\cdot\vec{\nabla})^2 \mathcal{E}_{n_h}(\vec{k})}{\displaystyle\sum_{n_e n_h} \int d\vec{k}\, |\, \varphi^{0;\, g}_{n_e n_h}(\vec{k})\, |^2\, (\hat{Q}\cdot\vec{\nabla})^2 (\mathcal{E}_{n_e}(\vec{k}) + \mathcal{E}_{n_h}(\vec{k}))}\,. \tag{4.17}$$

It accounts also for the dependence of β_0 on the direction $\hat{Q}$ of the COM-momentum in the case of warped valence bands.

In the derivation of Eq. (4.17), we neglected any Q-dependence of the (Coulomb) potential energy of the ground state. This is expected to be a good approximation since the Coulomb energy depends solely on the charge distribution, which should not be affected significantly by the COM motion of the exciton. Indeed, it has been estimated in Ref. [24] that the error introduced by neglecting in Eq. (4.11) the $\vec{k}$-dependence of the hole envelopes is about 5%. Our assumption is less restrictive and should lead to even smaller deviations.

4.4 Discussion

Based on two different Ansätze for the explicit dependence of the exciton ground state wavefunction on the COM momentum $\vec{Q}$, we developed two procedures for optimizing the COM transformation for the numerical calculation of the exciton ground state dispersion. The first one, see Eq. (4.5), requires only the knowledge of the exciton ground state wavefunction at vanishing COM momentum, but gives less satisfactory results for the systems of interest due to the strong coupling of the degenerate valence bands relative to the Coulomb coupling. The second one, Eq. (4.17), requires in addition to the exciton ground state

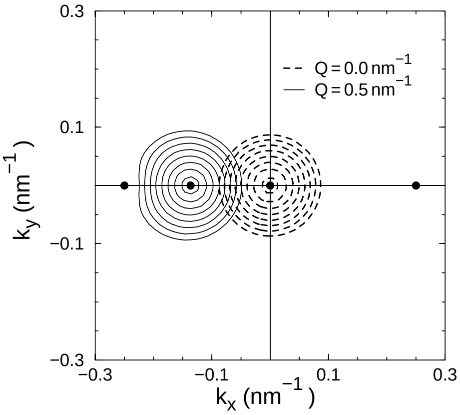

Figure 4.2: Logarithmic contour plots of the squared $HH_1C_1 - 1s$ exciton envelope in $\vec{k}$-space for a 5nm GaAs/Al$_{0.3}$Ga$_{0.7}$As QW at $Q_x = 0.5\text{nm}^{-1}$ plotted in a coordinate system with the not optimized value $\beta = 1/2$. Diamonds mark, from left to right, the origin of the shifted coordinate system [at $(1/2 - \beta)\, Q_x$] for $\beta = 0$, β_0, $1/2$, 1, with β_0 evaluated from Eq. (4.17). The $Q = 0$ envelope is plotted for comparison (dashed).

wavefunction at vanishing COM momentum the calculation of the single-particle dispersions (an easy task nowadays), but gives more accurate results.

The quality of Eq. (4.17) is illustrated in Fig. 4.2 where we plot the envelope of the $HH_1C_1 - 1s$ exciton in the single subband approximation using the symmetric value of $\beta = 1/2$ for $Q = 0$ and a quite large value of Q. This value of β is indeed not optimal, as the large shift of the envelope demonstrates. In contrast, the COM transformation for the value of β calculated after Eq. (4.17) would practically leave the envelope pinned at the origin.

The importance of a suitable choice of the COM transformation for the numerical convergence is illustrated in Fig. 4.3 for the dispersion of the $HH_1C_1 - 1s$ exciton of a 5nm QW. This has been calculated in $\vec{k}$-space for various values of β with the *same* basis (HH_1C_1, LH_1C_1, $\ell = 0, \pm 1, \pm 2$), see Sect. 5.1. The further the used β lies from the optimal value β_0 ($\beta_0 = 0.23$ in this case), the worse the results are. At large Q the $\beta = 0$ (in the parabolic case $m_h = \infty$) curve gives slightly better results than β_0 since the HH_1 subband dispersion gets more flat after the avoided crossing with the LH_1 subband, but it gives considerably worse results at small Q.

Although Eq. (4.17) was derived in the limes $Q \to 0$, it remains still useful even at quite large values of Q. Indeed, Fig. 4.4a demonstrates how small the deviations from the optimal values determined variationally at each Q value remain over the displayed large range of COM momenta.

Eq. (4.17) was derived by an optimization of the kinetic energy of the ground state exciton based on a rather realistic Ansatz for the wavefunction. However,

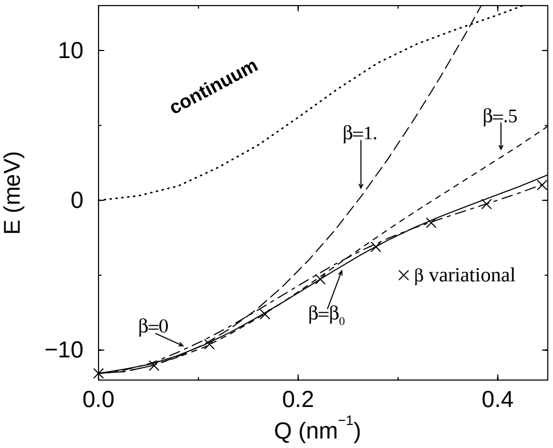

Figure 4.3: Numerical dispersion of the groundstate exciton of a 5nm wide QW calculated with the same basis set but for various values of β. The exciton continuum edge (dotted), Eq. (4.18), is given for comparison.

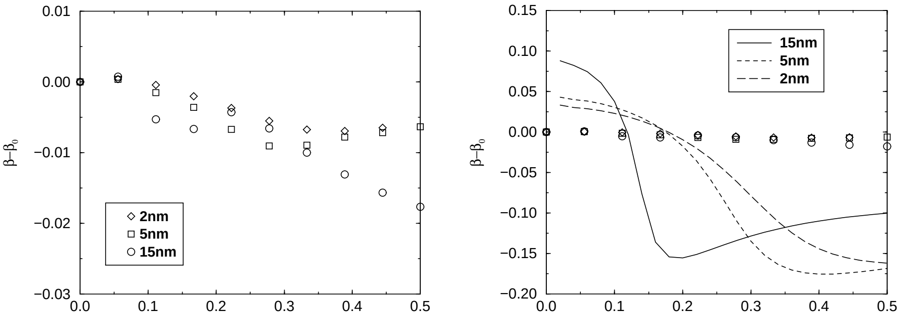

(a) (b)

Figure 4.4: Deviation of the analytical value β_0, Eq. (4.17), for the optimal choice of the COM transformation from the ones derived (a) variationally at each COM momentum Q for three different GaAs/Al$_{0.3}$Ga$_{0.7}$As QW and (b) from the exciton continuum edge (lines) for the same QW. For comparison, in the right panel also the variationally determined values from the left one are displayed. For the ground state, $0 \leq \beta \leq 1$ holds.

this requires the knowledge of the wavefunction at $Q = 0$.

One can also try to optimize the COM transformation based on some simpler exciton wavefunction, like, e.g., the one of the free electron-hole pair, i.e., a delta function in $\vec{k}$-space. Minimizing the kinetic energy of the free electron-hole pair for a given subband combination $n_e n_h$ and a given $\vec{Q}$ gives the electron-hole-pair continuum edge $\mathcal{E}_{n_e n_h}(\vec{Q})$

$$\mathcal{E}_{n_e n_h}(\vec{Q}) = min \left\{ \mathcal{E}_{n_e}(\vec{k}) + \mathcal{E}_{n_h}(\vec{k} - \vec{Q}) \right\} . \tag{4.18}$$

This coincides with the maximal energy of excited bound exciton states for a given subband combination in the single-band approximation and will be called in the following *exciton continuum edge*. For each value of $\vec{Q}$ the minimum occurs at some value $\vec{k}_{min}^{n_e n_h}(\vec{Q})$. In order to pin the exciton wavefunction at the origin, one has to choose the value $\beta_{n_e n_h}(\vec{Q}) = k_{min}^{n_e n_h}(\vec{Q})/Q$ (recall Eq. (4.9)) for the COM transformation. This can be evaluated with the sole knowledge of the subband dispersions. However, as shown in Fig. 4.4(b), this procedure does not give nearly as good results as Eq. (4.17). The real exciton ground state wavefunction having a finite extension averages over the subband dispersion features while the free electron-hole pair responds to all the details of the subband dispersions.

The optimization of the COM transformation of Sect. 4.3 will be of key importance for the numerically very demanding calculation of the QWR exciton ground state dispersion in Chap. 7.

Chapter 5

Exciton Dispersion in Quantum Wells

The multiband exciton (i.e., with the coupling of heavy- and light-hole bands taken fully into account) has been theoretically and numerically thoroughly investigated at vanishing COM momentum [22, 23, 24, 25, 26, 28, 27, 29]. The numerical effort for such calculations remains reasonable due to the high symmetry of this point. In contrast, only a few publications on multiband calculations of exciton dispersions in QW exist [30, 31, 32, 33], since these are very demanding.

We solved the eigenvalue problem (3.1) in two ways, which will be discussed in turn:

(i) in momentum space, expanding Eq. (3.6) in the product space of the electron and hole subband states, and

(ii) in real space, using a finite-differences scheme.

The first method gives very accurate results and is used to reveal the main features of the exciton dispersion. The second method is only suitable for the dispersion of a few low-energy states, but promised to be feasible for more general structures. A successful application to V-groove QWR is presented below in Chap. 7. The method (ii) is validated by comparing in this chapter its results for QW with the ones from the first method.

5.1 Solution in momentum space

The method we use here is in principle the extension for finite COM momentum Q of the one for $Q = 0$ introduced in [23] and described extensively in [26].

At a first step, we calculate the single-particle subband states and their dispersions. In the axial approximation the subband dispersions show no warping, and for symmetric QW the equations read

$$
\begin{aligned}
H_e \, |n_e \, \vec{k}_e; \pm\tfrac{1}{2}\rangle \;&=\; \mathcal{E}_{n_e}(k_e) \, |n_e \, \vec{k}_e; \pm\tfrac{1}{2}\rangle \\
H_h \, |n_h \, \vec{k}_h; \, p_h\rangle \;&=\; \mathcal{E}_{n_h}(k_h) \, |n_h \, \vec{k}_h; \, p_h\rangle \, ,
\end{aligned}
\tag{5.1}
$$

with the Hamilton operators of Eq. (2.9,2.10,3.3,3.4) and the single-particle states

$$
\begin{aligned}
|n_e \, \vec{k}_e; \pm\tfrac{1}{2}\rangle \;&=\; \frac{e^{i\vec{k}_e \cdot \vec{r}_{e_\parallel}}}{2\pi} \, \xi_{n_e}(z_e) \, |\tfrac{1}{2} \, \pm \, \tfrac{1}{2}\rangle_c \, , \qquad (5.2) \\
|n_h \, \vec{k}_h; \, p_h = \pm 1\rangle \;&=\; \frac{e^{i\vec{k}_h \cdot \vec{r}_{h_\parallel}}}{2\pi} \sum_{m_J} e^{i\,(m_J - \bar{m}_J)\,\theta_h} \, \xi^{m_J}_{n_h,\,p_h,\,k_h}(z_h) \, |\tfrac{3}{2} \, m_J\rangle_v \, .
\end{aligned}
$$

$n_{e,h}$ denote the subband indices, $\vec{k}_{e,h} = (k_{e,h}, \, \theta_{e,h})$ is the respective in-plane wavevectors in polar coordinates, $\xi^{m_j}_{nk}(z)$ are the envelopes of the respective band edge states, and p_h the hole parity under specular reflection with respect to the $z = 0$ (center of the symmetric structure) plane σ_{xy} [78]. We take advantage of the freedom in introducing an arbitrary phase factor to make the phase dependence vanish for the main spin component $\bar{m}_J$ of each subband (see footnote 4). [1]

Since we assume the conduction band to be parabolic, the conduction subbands and their dispersion are analytically known [95, 52]. The valence subbands are calculated using a transfer-matrix method as in [96, 97]. The latter is an extension for the multi-band case of the usual one-band transfer-matrix method often employed, e.g., in solving the Kronig-Penney model. In brief, the single-particle wavefunction is constructed as a superposition of the bulk band states at a trial energy at some point in the structure and propagated to the left and right with the additional condition for bound states of vanishing at infinity. This leads to a determinantal equation for the calculation of the subband dispersions. The formalism is presented in short in Appendix B. An important aspect of this method is that the subband eigenfunctions, in particular the envelopes, are finally known analytically as a superposition of exponentials and trigonometric functions. The usual symmetric boundary conditions have been used. The numerical dispersions and eigenfunctions were checked against the analytic results of Ref. [78].

At a second step, the exciton wavefunction for a given COM momentum $\vec{Q}$ is expanded into[2]

$$
\Psi^{\vec{Q};\,P\alpha}(\vec{r}_e, \, \vec{r}_h) \;=\; \sum_{n_e n_h} \int d\vec{k} \; \varphi^{\vec{Q};\,a}_{n_e n_h}(\vec{k}) \, |n_e \, \vec{k}_e \, ; +\tfrac{1}{2}\rangle_c \, |n_h \, \vec{k}_h; \, p_h\rangle_v \, , \tag{5.3}
$$

---

[1] The phase factors $e^{i\, m_{J_{e,h}}\, \theta}$ arise naturally from the $|J_{e,h} m_{J_{e,h}}\rangle$-basis, when the reference system is rotated through an angle θ around $J \parallel z$ [79].

[2] Eq. (5.3,5.6,5.7) are simply the subband expansion equations Eq. (4.8, 4.11) of Sect. 4.3 for the particular single-particle model examined in this section.

with subband states of the two particles combined in such a way that the resulting exciton state has the required parity P and total momentum $\vec{Q}$

$$\vec{k}_e = \vec{k} + \beta\vec{Q}, \qquad \vec{k}_h = \vec{k} - (1-\beta)\,\vec{Q}\,, \qquad P = p_h \cdot (-1)^{n_e+1}\,. \tag{5.4}$$

The last equality reflects the fact, that for symmetric QW the conduction subband envelopes are even (odd) for odd (even) subband index. Fixing exciton parity P and electron spin eliminates any degeneracy at $\vec{Q} \neq 0$.

With the expansion (5.3) and the relations (5.4), the exciton Schrödinger equation takes the form

$$\begin{aligned}\Big(\mathcal{E}_{n_e}(\vec{k}_e) + \mathcal{E}_{n_h}(\vec{k}_h) - E^X_a(\vec{Q})\Big)\;\varphi^{\vec{Q};\,a}_{n_e n_h}(\vec{k}) +&\\ \textstyle\sum_{n'_e n'_h} \int d\vec{k}'\, V^{\vec{Q}}_{\substack{n'_e n'_h\\ n_e n_h}}(\vec{k},\vec{k}')\,\varphi^{\vec{Q};\,a}_{n'_e n'_h}(\vec{k}') = 0\,,&\end{aligned} \tag{5.5}$$

where $E^X_a(\vec{Q})$ denotes the energy dispersion of the exciton state. The interaction

$$V^{\vec{Q}}_{\substack{n'_e n'_h\\ n_e n_h}}(\vec{k},\vec{k}') = -\frac{1}{2\pi}\frac{e^2}{\epsilon}\frac{1}{|\vec{k}-\vec{k}'|}\,\mathcal{F}^{\vec{Q}}_{\substack{n'_e n'_h\\ n_e n_h}}(\vec{k},\vec{k}') \tag{5.6}$$

is the in-plane 2D Fourier transform of the 3D Coulomb potential modified due to the confinement in z-direction. The latter is expressed through form factors (with Eq. (5.4))

$$\begin{aligned}\mathcal{F}^{\vec{Q}}_{\substack{n'_e n'_h\\ n_e n_h}}(\vec{k},\vec{k}') = \sum_{m_J}\iint dz_e\, dz_h\, e^{-|\vec{k}-\vec{k}'|\,|z_e-z_h|}\,\times&\\ \xi^*_{n_e}(z_e)\,\xi^{m_J\,*}_{n_h,\,\vec{k}_h}(z_h)\,\xi_{n'_e}(z_e)\,\xi^{m_J}_{n'_h,\,\vec{k}'_h}(z_h)\,.&\end{aligned} \tag{5.7}$$

Note that a dependence on Q enters the form factors via the hole momentum, Eq. (5.4). The parity selection rule of Eq. (5.4) for symmetric QW is obtained when changing the sign of both electron and hole z coordinates in the above equation. As mentioned before, the transfer matrix method that we used to calculate the subband states yields the wavefunctions, i.e., the envelopes in analytical form as linear combinations of exponential and trigonometric functions. The form factors are in this case known analytically in terms of the parameters (coefficients and wavelengths) of the envelopes.

The integrable singularity of the Coulomb potential (5.6) at $\vec{k} = \vec{k}'$ is taken care of by adding and subtracting in Eq. (5.5) the analytically integrable term

$$C(\vec{k},\,\vec{k}') = \frac{e^2}{\epsilon}\,\frac{1}{2\pi}\left(\frac{1}{|\vec{k}-\vec{k}'|} - \frac{1}{\max(k,\,k'))}\right). \tag{5.8}$$

This gives a very smooth "corrected" potential (5.15) of small absolute magnitude. Our singularity correction term $C(\vec{k},\,\vec{k}')$ is essentially the 2D-Coulomb potential having added to it a simple term, in order to make the correction term integrable. In contrast to the straightforward extension for $Q \neq 0$ of the singularity correction used in [26], it is independent of Q, and independent of the subbands and angular momentum components involved. Integrating out the angles leads to:

$$C(k,k') \;=\; \frac{e^2}{\epsilon}\,\frac{1}{2\pi}\,\frac{4}{\max(k,k')}\left(K\left(\frac{\min(k,k')}{\max(k,k')}\right)-\frac{\pi}{2}\right), \qquad (5.9)$$

where $K(x)$ is the complete elliptic Integral of the first kind. The integral over one of the arguments of this function is known to be [93]

$$\frac{\epsilon}{e^2}\int_0^\infty dk'\;C(k,k') \;=\; 2\ln 2 - 1\,. \qquad (5.10)$$

To take benefit of the axial approximation[3], the exciton envelope and the form factors are expanded into 2D angular momentum eigenstates $e^{i\ell\phi}$ [26]

$$\varphi^{Q;\,a}_{n_e n_h}(\vec{k}) = \sum_{\ell} e^{i\ell\phi}\varphi^{Q;\,\alpha}_{n_e n_h \ell}(k)\,. \qquad (5.11)$$

After integrating out the angles, the equations to be solved read

$$\begin{aligned}
&\big(\,T^{0;Q}_{n_e}(k) + T^{0;Q}_{n_h}(k) - E^X_a(Q) - k\;C(k)\,\big)\,\varphi^{Q;\,\alpha}_{n_e n_h \ell}(k)\\
&\quad - \sum_{n'_e n'_h \ell'} \int k'\,dk'\,\tilde{V}^{Q}_{n'_e n'_h \ell' \atop n_e n_h \ell}(k,k')\,\varphi^{Q;\,\alpha}_{n'_e n'_h \ell'}(k')\\
&-\int dk'\;C(k,k')\left(k'\,\varphi^{Q;\,\alpha}_{n_e n_h \ell}(k') - k\,\varphi^{Q;\,\alpha}_{n_e n_h \ell}(k)\right)\\
&\quad + \sum_{\ell' \neq \ell}\left(T^{\ell-\ell';Q}_{n_e}(k) + T^{\ell-\ell';Q}_{n_h}(k)\right)\varphi^{Q;\,\alpha}_{n_e n_h \ell'}(k) \;=\; 0\,, \qquad (5.12)
\end{aligned}$$

where in the axial approximation

$$T^{\mu;Q}_{n_{e,h}}(k) = \frac{1}{\pi}\int_0^\pi d\theta\,\mathcal{E}_{n_{e,h}}(k_{e,h})\cos(\mu\,\theta)\,. \qquad (5.13)$$

For $Q = 0$, the terms (5.13) are simply the moments of the single-particle dispersions, vanishing in the axial approximation for $\mu > 0$.

The term $C(k)$ is the integral of the added singularity correction over the k-space and depends on k if one restricts the integration to just a part of the k-space

$$C(k) \;=\; \int_0^{k_{max}} dk' C(k,k') \;=\; \frac{e^2}{\epsilon}\,(2\ln 2 - 1) - \int_{k_{max}}^{\infty} dk' C(k,k')\,. \qquad (5.14)$$

The latter integral can easily be done numerically, since the singularity lies outside the integration interval.

---

[3] In the axial approximation the exciton wavefunction is independent of the direction of $\vec{Q}$, thus, we index the quantities in the equations following only by Q.

$\tilde{V}$ is essentially what remains from the Coulomb interaction after the singularity is removed [4]

$$\tilde{V}^{Q}_{\substack{n'_e n'_h \ell' \\ n_e n_h \ell}}(k,k') = \frac{1}{2\pi} \iint \frac{e^{i(\ell\theta - \ell'\theta')}\, d\theta\, d\theta'}{\sqrt{k^2 + k'^2 - 2\,k\,k'\,\cos(\theta - \theta')}} \times \tag{5.15}$$
$$\left(\frac{e^2}{\epsilon} \sum_{m_J} e^{i\left((m_J - \bar{m}_J)\theta_h - (m_J - \bar{m}'_J)\theta'_h\right)} Z^{m_J}_{\substack{n'_e n'_h \\ n_e n_h}}(k_h, k'_h, \theta_h - \theta'_h) - C(k,k')\, \delta_{\substack{n_e n_h \ell \\ n'_e n'_h \ell'}} \right)$$

with

$$\begin{aligned} Z^{m_J}_{\substack{n'_e n'_h \\ n_e n_h}}(k,k',\theta) \quad &= \quad \tfrac{1}{2\pi} \iint dz_e\, dz_h\, e^{-|z_e - z_h|\sqrt{k^2 + k'^2 - 2\,k\,k'\,\cos\theta}} \times \\ &\qquad \xi^{*}_{n_e}(z_e)\, \xi_{n'_e}(z_e)\, \xi^{m_J}_{n_h k}(z_h)\, \xi^{m_J *}_{n'_h k'}(z_h)\,. \end{aligned} \tag{5.16}$$

For $Q = 0$, the integrand of Eq. (5.15) becomes, as expected, diagonal in the angular momentum ℓ, yielding the selection rule

$$\ell + \bar{m}_J = \ell' + \bar{m}'_J\,. \tag{5.17}$$

That is, for each combination $n_e n_h \ell$ [5] there are at a maximum four others to couple with. The double integral $Z(k,k',\theta)$ is a smooth function of its arguments, except at $k = k', \theta = 0$, i.e., at $\vec{k} = \vec{k}'$, where the first derivatives become discontinuous. It has been calculated once for a dense mesh of its arguments and then interpolated, taking care to treat the singularity correctly.[6]

All the integrals have been calculated using Simpsons rule. The double integral $Z(k,k',\theta)$ was calculated on a 151x151x25 mesh ($dk = 0.01\text{nm}^{-1}$, $d\theta = \pi/25$) for all the required subband combinations.

Before discretizing Eq. (5.12), we multiplied them by $\sqrt{dk\,k}$ and used the substitution $\bar{\varphi}^{Q;\,\alpha}_{n_e n_h \ell}(k) \equiv \sqrt{dk\,k}\,\varphi^{Q;\,\alpha}_{n_e n_h \ell}(k)$. This leads after the discretization to a symmetric matrix, whose eigenproblem can be solved efficiently (reduced memory and CPU usage). The reverse substitution is not a problem, since the mesh did not involve the $k = 0$ point (grid points at $k_i = (i - 1/2)dk$, $i =$

---

[4] Setting the phase of the main component of each subband to zero, Eq. (5.2), increases considerably the numerical accuracy for small Q values. This is related to the interference of the two phase factors, the one of the angular decomposition and the one of the spin components, in Eq. (5.15). At large Q values, the spin-dependent phase factors are becoming less important as the most important hole wavevectors are near $\vec{k}_h \simeq \beta\vec{Q}$ and hence $\theta_h \simeq 0$. In addition, with this choice the value of ℓ corresponds to the angular momentum L of the exciton's relative wavefunction in the independent subband approximation (otherwise $\ell = L + \bar{m}_{J_e} - \bar{m}_{J_h}$ [26]).

[5] The conduction subband index is also of relevance. It determines (over the parity selection rules Eq. (5.4)) whether the coupling is to the "spin up" or "spin down" subband state, whose main components are at opposite spin.

[6] A major numerical difficulty at this point is to avoid arbitrary sign changes of the numerically calculated subband states, which lead to artificial discontinuities in the double integral to be interpolated. Even after tracing the sign of the coefficient of the main bulk component of the envelopes, still some sign corrections had to be made by hand. In addition, this integral often changes sign in a continuous manner at avoided crossings, which complicates things even further.

$1,..,N$). Such a mesh was also used for the relative angle $\theta-\theta'$ in Eq. (5.15) to avoid the singularity at $\vec{k}=\vec{k}'$.

Of great importance for the numerical accuracy has been the use of the optimized COM transformation Eq. (4.17). Numerical evidence of this fact, that has been obtained with the method presented in this section, was discussed when commenting on Fig. 4.3 in Sect. 4.4. After solving Eq. (5.12) at $Q=0$, the obtained exciton ground state wavefunction has been used to calculate the optimal value of $\beta=\beta_0$. For this, a 2D $1s$-exciton groundstate function

$$\varphi_{1s}^{2D}(\vec{\rho}\,)=\sqrt{\frac{2}{\pi a_B^2}}\;e^{-\rho/a_B},\;\varphi_{1s}^{2D}(\vec{k}\,)=\sqrt{\frac{2a_B^2}{\pi}}\;\left(1+(a_Bk)^2\right)^{-3/2}, \qquad (5.18)$$

a_B the Bohr radius, is fitted to the HH_1C_1 envelope. For the wider QW, where the LH_1C_1 component becomes important, also a 2D $3d$-exciton function is fitted to the LH_1C_1 envelope. These fits are used, instead of the numerical envelope, to evaluate the optimized COM transformation (4.17), because it allows to take advantage of the analytically known derivatives of the fit function. This optimized COM transformation has been subsequently used for calculating the exciton at $Q\neq 0$.

5.1.1 Results for GaAs/Al$_{0.3}$Ga$_{0.7}$As quantum wells

We calculated exciton dispersions for GaAs/Al$_{0.3}$Ga$_{0.7}$As $\langle 001\rangle$ QW of widths between 2nm and 20nm. The material parameters γ_1, γ_2, γ_3 were obtained by linear interpolation from the GaAs ($\gamma_1=6.85$, $\gamma_2=2.1$, $\gamma_3=2.9$) and AlAs ($\gamma_1=3.45$, $\gamma_2=0.68$, $\gamma_3=1.29$) values; the conduction band mass was taken $m_e=0.0665m_0$ for both materials, the offset ratio was $V_v/V_c=0.68/0.32$, and the band gap in meV was $E_g(x)=1519+1040\,x+470\,x^2$, x being the Al content. The dielectric constant $\epsilon=12$ was used [98].

5.1.1.1 Valence subband dispersion features

Before examining more closely the results obtained for the exciton, let us first point to some QW-specific single-particle features that will be of relevance in the discussion of the exciton results. In Fig. 5.1, the calculated valence subband dispersions for some QW of characteristic width values are displayed. Some well-known features (see, e.g., [52]) are immediately seen: (i) the wider the QW, the more subbands exist, (ii) the confinement energy (difference in energy of subband and band edge of the well material at the Γpoint) of a particular subband decreases with the well width, (iii) the different masses of light- and heavy-hole, the light-hole having the larger in-plane mass (see Eq. (2.9,2.10)), lead to different curvatures of the dispersions and to avoided crossings, (iv) the confinement of the light-hole subbands is smaller than that of the respective heavy-hole subbands, due to the light-hole having a smaller mass in the growth direction than the heavy-hole, (v) the subband dispersions at the avoided crossing are extremely nonparabolic; this is especially true for wider QW, where the subband separation is smaller and the avoided crossings are more pronounced. The position of the avoided crossing between two specific subbands shifts to smaller k with increasing QW width.

Some subbands show a negative dispersion at the Γpoint, like, most noticeable, the first light-hole (LH) subband. This is due to the prevalent coupling to the lower subband over the coupling to the higher one. In the absence of strain, the highest subband has always a positive mass; this mass is larger than the heavy-hole in-plane mass in the diagonal approximation, Sect. 2.3.

We plot in Fig. 5.2 the light-hole admixture ratio, that is for the hole subband states of Eq. (5.2) the quantity

$$P_{lh} = \sum_{m_J=\pm\frac{1}{2}} \int dz_h \left|\xi^{m_J}_{n_h p_h, k_h}(z_h)\right|^2 , \qquad (5.19)$$

for the two lowest subbands versus the in-plane wavevector k. The subband states at the Γpoint have a clear light- or heavy-hole character, and are usually denoted by HH_n and LH_n, n an incremental index, for heavy- and light-hole subbands, respectively. However, away from the Γpoint the subbands attain a mixed heavy- and light-hole character. At large enough k all subbands acquire a light-hole character. Comparison of the panels (a) and (b) of Fig. 5.2 shows, not surprisingly, the aforementioned shift of the position of the $HH_1 - LH_1$ crossing towards small k with larger well width.

Another interesting feature is the fact, that, although the heavy-light-hole admixture P_{lh} changes drastically over the BZ, the charge distribution itself is not much affected by the in-plane momentum. This is clearly demonstrated in Fig. 5.3, where we plot in (c) the hole probability distribution along the growth direction for the HH_1 subband states at $k = 0$ and $k = 1\text{nm}^{-1}$ and in panels (a) and (b) the respective envelope components. Notice the somewhat stronger confinement for the large k value; this is not due to the variation of the confining potential (the energy difference of the lowest barrier and well band edges at same in-plane momentum) which in this case actually decreases with k, but rather to the coupling of in-plane motion and the motion in the confining direction. Because of this coupling, higher in-plane kinetic energy means also higher kinetic energy in growth direction and, hence, larger confinement.

5.1.1.2 Exciton dispersion

We introduce the following nomenclature: the exciton in the subband expansion has various $n_h n_e$ subband components with the corresponding envelopes $\varphi^{\vec{Q};a}_{n_e n_h}(\vec{k})$, Eq. (5.3). These envelopes have in the axial approximation at $Q = 0$ a definite angular momentum ℓ. According to this, they will be denoted $1s$, $2s$, $2p_\pm$, $3d_\pm$ and so on. At finite Q each exciton state will be named according to the main subband component of the corresponding state at $Q = 0$. That is, speaking of the $HH_1C_1 - 1s$ exciton only states that at $Q = 0$ its main subband component is the HH_1C_1 one with an $1s$ (node-free axial-symmetric) envelope. Similar to the single-particle hole subband states, that can change

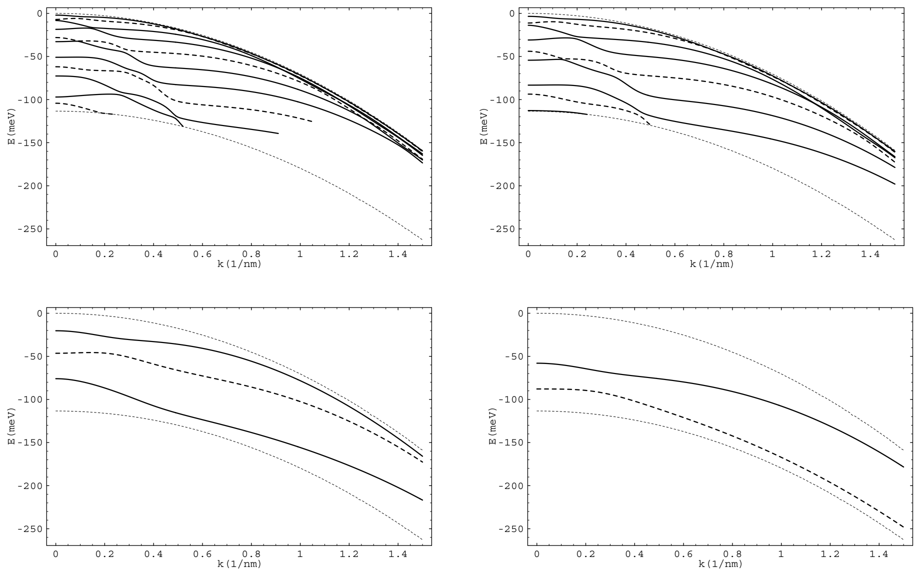

Figure 5.1: Dispersions of the HH subbands (thick) and LH subbands (thick dashed) in the axial approximation for GaAs/Al$_{0.3}$Ga$_{0.7}$As QW of width (from top left to bottom right) 20nm, 15nm, 5nm, and 2nm. The bulk band edges (thin dotted) for the well and barrier materials are also displayed. Note the shift of the HH_1-LH_1 avoided crossing towards the center of the Brillouin zone for increasing QW width L.

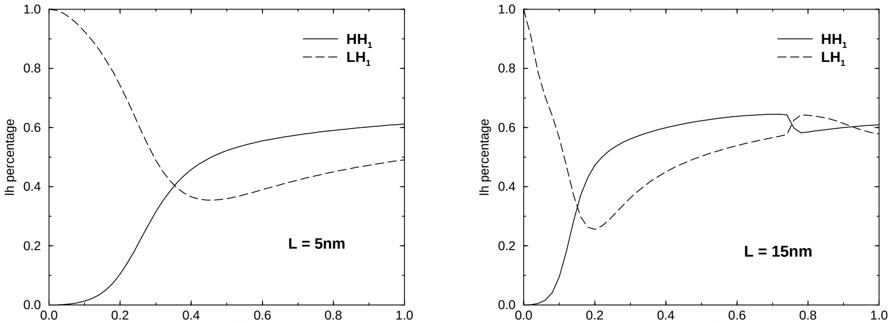

(a) (b)

Figure 5.2: Bulk light-hole admixture ratio P_{lh}versus the hole wavevector $\vec{k}$ for the HH_1 and LH_1 subbands in (a) the 5nm and (b) the 15nm QW of Fig. 5.1. Beyond the avoided crossing, the HH_1 subband acquires a prominent bulk lh character. The $HH_1 - LH_1$ crossing occurs for much smaller k in the wider well. A second avoided crossing due to the HH_2 subband is seen for the wider QW at large k.

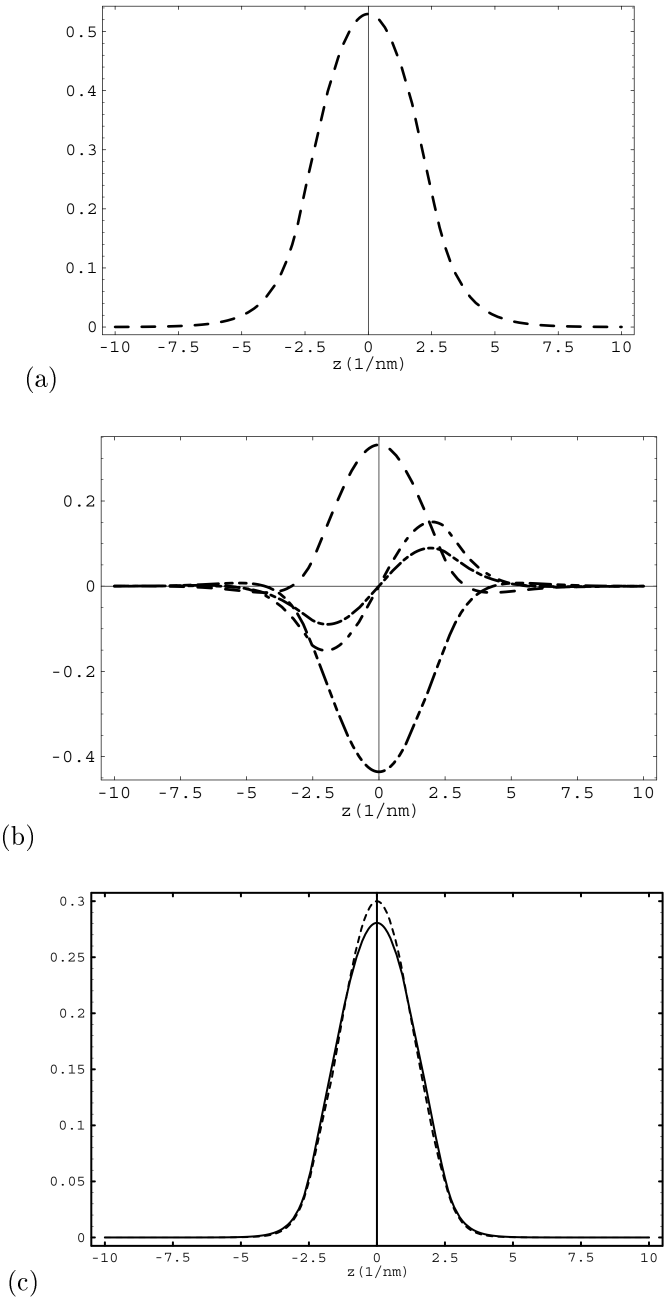

Figure 5.3: Envelopes of the HH_1 subband at (a) $k = 0$ and (b) $k = 1\text{nm}^{-1}$, respectively, for the 5nm QW of Fig. 5.1. The line style indicates the spin component: $+3/2$ (dashed), $+1/2$ (dot-dashed), $-1/2$ (dot-dot-dashed), and $-3/2$ (dot-dashed-dashed). (c) charge distribution for the subband states of (a) (line) and (b) (dashed), respectively.

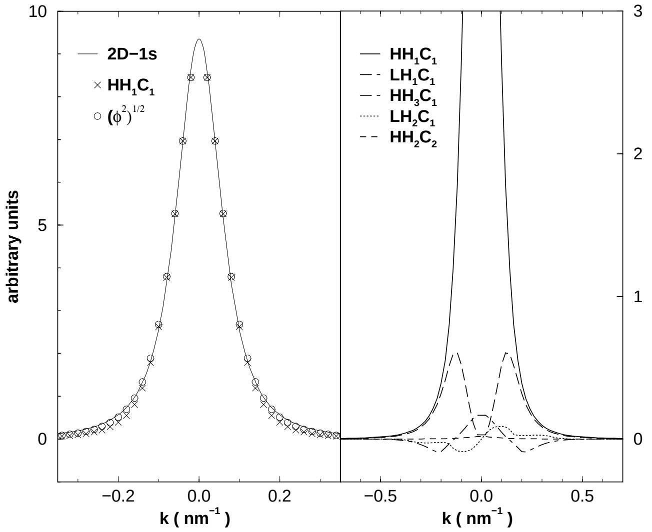

Figure 5.4: On the right: Envelopes of the subband components of the groundstate exciton calculated in k-space for a 15nm wide QW at $Q = 0$. On the left: HH_1C_1 envelope ($\times$), fitted 2D 1s-exciton wavefunction (line), and square root of the total probability distribution $\phi^2(k) = \sum_{n_e n_h} \varphi^{0;\,g}_{n_e n_h}(k)^2$ (circles).

their heavy- or light-hole character away from the Γ-point, the envelope of the main subband component or even the main subband component itself can change with increasing Q. To denote the main subband component of a state at some Q, we will speak of the "character" of the state at this Q. As an example, the $HH_1C_1 - 2p_+$ exciton that has a $HH_1C_1 - 2p_+$ character at $Q = 0$ might have an $LH_1C_1 - 1s$ character at some $Q \neq 0$ (and, indeed, it does in the case described in Sect. 5.2.2).

In Fig. 5.4, we display the envelopes of the components of the groundstate exciton in the subband expansion (5.3) for a 15nm wide QW at $Q = 0$. The coupling of the higher subbands is rather small, less than 3% for the LH_1C_1 component and even less for the others. The selection rules for parity, Eq. (5.4), and spin (the interaction being diagonal in the spin components) for the Coulomb coupling of the subbands at the Γ-point in symmetric QW are obeyed. For example, the admixture of the LH_1C_1 state vanishes at the Γ-point, since the Coulomb potential is spin-diagonal and the HH_1 and LH_1 subband states are pure heavy- and light-hole states, respectively. The HH_1C_1 envelope is very well approximated by a 2D 1s-exciton groundstate function. Deviations are mainly located at the vicinity of the $HH_1 - LH_1$ avoided crossing of the hole subband dispersions that for this QW lies at $k_{ac} \simeq 0.13\text{nm}^{-1}$. The total in-plane probability distribution follows the form of Eq. (5.18) even better than the HH_1C_1 envelope alone; the coupling to the higher subbands allows the exciton to relax further. This, again, supports the notion that the subband mixing has little

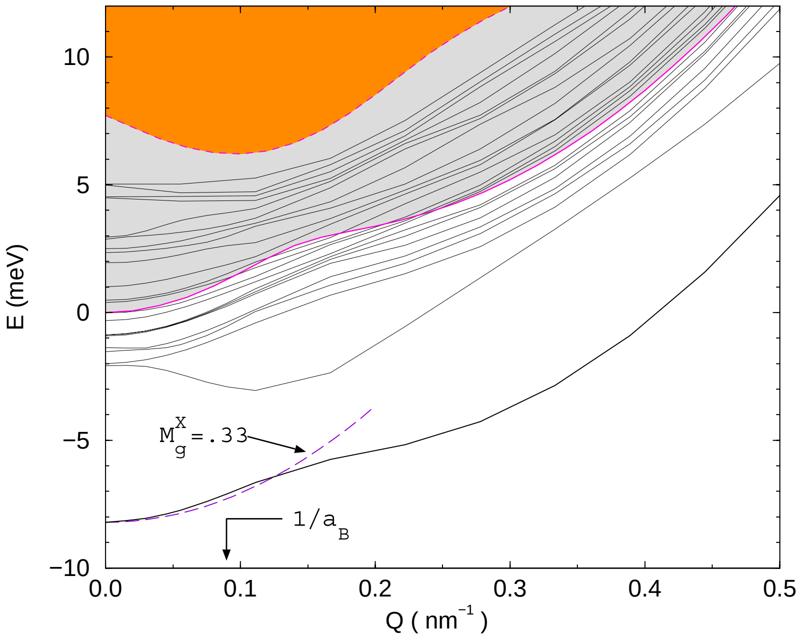

Figure 5.5: Exciton dispersions, ground state (thick) and some excited bound and continuum states (thin), calculated in k-space for a 15nm wide QW. The light (dark) gray shaded area mark the HH_1C_1 (LH_1C_1) exciton continuum. A parabola for the average groundstate exciton mass M_g^X after Eq. (6.1,6.2) is plotted (dashed). An arrow marks the position of $1/a_B$ (a_B the Bohr radius).

influence on the charge distribution.

The calculations in momentum space presented in the following take into account only the two lowest hole subbands ($n_hn_e = HH_1C_1$, LH_1C_1). Inclusion of higher subbands does not enlarge the binding energy of the groundstate exciton considerably. For the angular decomposition of the envelope components only the s, $p_\pm$, d_+ ($\ell = 0, \pm 1, 2$) components for the HH_1C_1 and the s, $p_\pm$, d_- ($\ell = 0, \pm 1, -2$) components for the LH_1C_1 were considered. Due to the optimized choice of the COM coordinate system, Eq. (4.17), these few angular momentum components are enough to describe excellently the dispersion of the $HH_1C_1 - 1s$ and $LH_1C_1 - 1s$ excitons over the whole range of COM momentum values considered, $Q \leq 0.5\text{nm}^{-1}$; the p components account mainly for the deformation of the envelope and the d components account for the Coulomb coupling to higher states.

In Fig. 5.5, we show the dispersion calculated in k-space of the first bound exciton states as well as some of the continuum states in a 15nm wide QW. The energy zero is the onset of the HH_1C_1 continuum at $Q = 0$. The Bohr radius a_B is the one obtained from the same fit of a 2D 1s-exciton to the envelope of the HH_1C_1 component at $Q = 0$ needed to calculate the optimized β_0. The

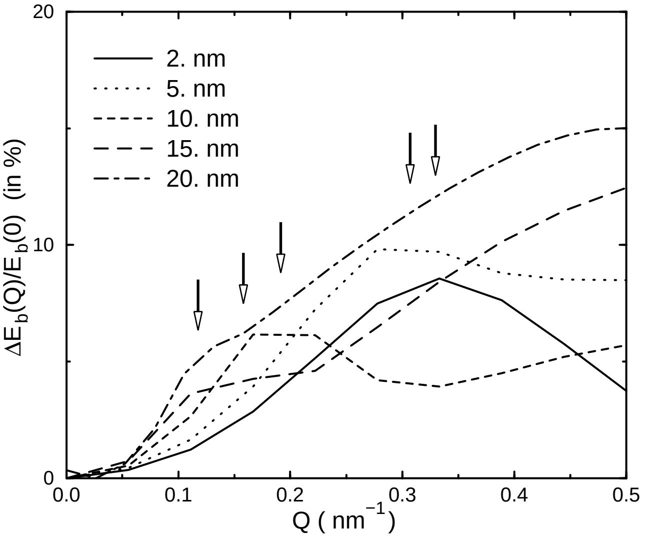

Figure 5.6: Enhancement of the exciton binding energy $E_b(Q)$ with increasing COM momentum Q for GaAs/Al$_{0.3}$Ga$_{0.7}$As QW of various widths. The arrows mark the position of the respective HH_1-LH_1 avoided crossing from the right to the left for growing QW width.

ground state is the $HH_1C_1 - 1s$. The next state is the $HH_1C_1 - 2p_+$ which at the region of the avoided crossing has $LH_1C_1 - 1s$ character. The $LH_1C_1 - 1s$ exciton is at $Q = 0$ the fourth excited state and shows a substantial mixing with the $HH_1C_1 - 3d_+$ exciton. The $HH_1C_1 - 2p_+$ exciton has at $Q = 0$ a slightly lower energy than the $HH_1C_1 - 2p_-$ (3rd state at $Q=0$) because it couples to the $LH_1C_1 - 1s$ outside of the Γ-point.

The enhancement of the groundstate binding energy for $Q \neq 0$ is particularly large when the exciton is built from hole subband states around the avoided crossings $(1 - \beta_0)Q = k_{a.c.}$. This is demonstrated in Fig. 5.6 for QW of various widths. Peaks are seen at the respective location of the HH_1-LH_1 avoided crossing, marked with arrows. The enhancement of the groundstate binding energy with Q is less than 15% and is generally larger for wider QW.

Indirectly, the enhancement of the groundstate binding energy for $Q \neq 0$ is also seen in Fig. 5.7 in the change of the groundstate exciton probability distribution with Q. Indeed, for $Q = 0.5\text{nm}^{-1}$ larger momentum values are involved in the probability distribution, indicating a smaller effective Bohr radius. The numerical fits give a reduction of the Bohr radius of about 30%.

The observed enhancement of the exciton binding energy is another indicator of the very good quality of our numerical results even at such large values of Q. Indeed, since numerical errors usually result in a steeper dispersion (Ritz's variational principle) and since the binding energy is taken as the difference to the exciton continuum edge, which is known with excellent accuracy, a binding

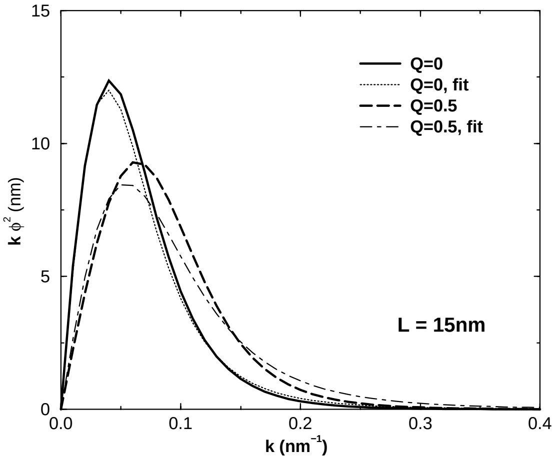

Figure 5.7: Radial probability distribution $k\sum_{n_en_h}\left|\varphi^{Q;g}_{n_en_h}(\vec{k})\right|^2$, calculated in the optimized COM coordinate system, for the groundstate exciton at $Q = 0$ (thick line) and $Q = 0.5\text{nm}^{-1}$(thick dashed) for the 15nm wide QW of Fig. 5.5. Fits with a $2D - 1s$ exciton function, Eq. (5.18), are displayed for comparison.

energy decreasing rather than increasing with Q can be expected.

5.1.1.3 The $LH_1C_1 - 1s$ exciton dispersion

It is a well-known feature [52], that the LH_1-subband shows near the Brillouin zone center a negative dispersion, due to the coupling with higher subbands or continuum states. This may result in a dispersion for the lh-exciton with the minimum being off the center of the Brillouin zone (see Fig. 5.1). We expect such a camel-back structure in the exciton dispersion to lead to the light-hole exciton relaxing into states, where it does not couple to the electromagnetic field, delaying significantly the exciton recombination and, hence, increasing its lifetime. However, the fast light to heavy exciton relaxation will make this effect difficult to observe.

In Fig. 5.8, we show the exciton dispersion of a 5nm QW. The exciton dispersions, like the hole subbands dispersions, are less anharmonic in the much narrower QW than for the QW of Fig. 5.5 because of the larger energy separation of the two subbands. The avoided crossing takes place at rather large k (0.31nm^{-1}).

In order to visualize the $LH_1C_1 - 1s$ exciton being resonant with the HH_1C_1 continuum, we use a shading indicating the percentage of the contribution of the LH_1C_1 subband states to the norm of the numerical eigenvectors. The very light shading of the bound exciton states confirms the small admixture of the LH_1C_1 states in the groundstate, being darker in the vicinity of the avoided crossing. Small-scale intensity variations are numerical artefacts due to the

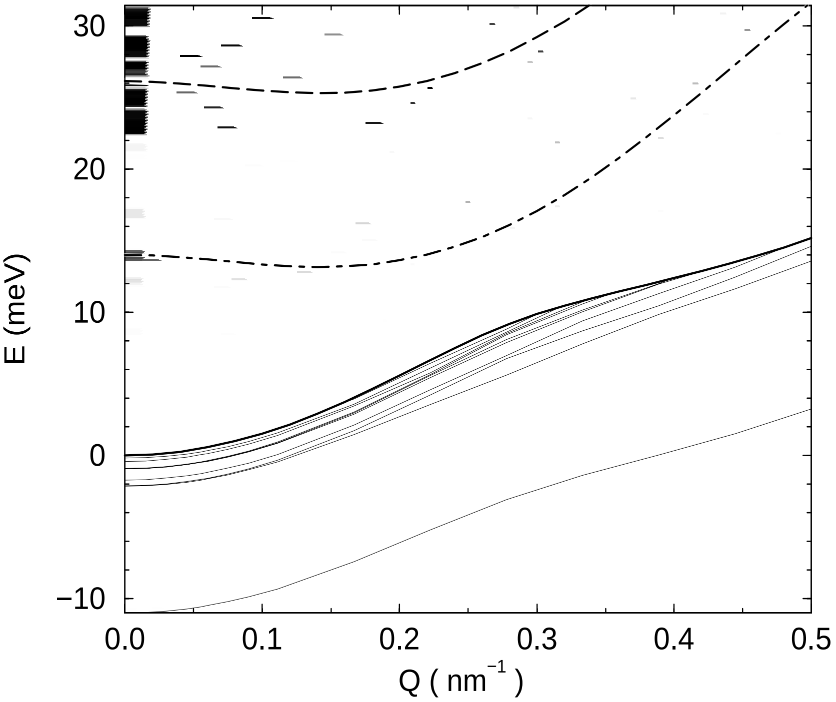

Figure 5.8: Exciton dispersion for the 5nm GaAs/Al$_{0.3}$Ga$_{0.7}$As QW. The HH_1C_1 (thick) and LH_1C_1 (dashed) exciton continuum edges are also shown. The background shading indicates how strong is the mixture of the LH_1C_1 exciton states to the numerically calculated eigenstates (black corresponds to 100%). For comparison, also a LH_1C_1 (dot-dashed) exciton continuum edge shifted to the energy of the $LH_1C_1 - 1s$ state at $Q = 0$ has been drawn.

finite k-space mesh. In the exciton continuum only the shading is shown. The $LH_1C_1 - 1s$ resonance is clearly seen starting at approximately 14meV, lying above the dash-dotted shifted LH_1C_1 exciton continuum edge line for larger Q. The resonance is sharper at the beginning and becomes more diffuse at the avoided crossing. It lies slightly above the respective exciton continuum edge. The $LH_1C_1 - 1s$ resonance does not seem to show the negative dispersion of the LH_1-subband.

For wider QW the separation of the HH_1- and LH_1-subbands at the Γpoint becomes smaller and the $LH_1C_1 - 1s$ exciton comes closer to the HH_1C_1 continuum edge eventually falling below it for the 13nm wide well. The camel-back shaped $LH_1C_1 - 1s$ dispersion can be clearly seen for the 20nm wide QW, where the $LH_1C_1 - 1s$ is well separated from the HH_1C_1 states, Fig. 5.9(b).

5.1.1.4 Groundstate dispersion and continuum edge

As was reported in earlier work [30, 31], the exciton COM dispersions are highly non-parabolic, much like the hole subband dispersions. This is not surprising, since the dispersion of the conduction subband is parabolic and the hole mass is much larger than the electron mass. Furthermore, it has been claimed in Ref. [31] that the exciton dispersion follows, in a good approximation, the hole subband dispersion. Although this is certainly true in the present case due to the parabolic electron dispersion and the small electron to hole mass ratio, the exciton groundstate dispersion should be related to a two-particle quantity. In fact, the dispersion of the groundstate exciton follows even more closely, in the studied cases within 1meV, the electron-hole-pair continuum edge or exciton continuum edge $\mathcal{E}_{n_e n_h}(\vec{Q})$, Eq. (4.18), with n_e, n_h the indices of the lowest conduction and valence subbands, respectively.

In Figs. 5.9(a,b) the exciton groundstate dispersion and the appropriately shifted exciton continuum edge are directly compared for a narrow and a wide QW. Also shown is the respective hole dispersion. The latter lies always above the shifted exciton continuum edge, since Eq. (4.18) implies $\mathcal{E}_{n_e n_h}(\vec{Q}) \leq \mathcal{E}_{n_e}(0) + \mathcal{E}_{n_h}(\vec{Q})$.

The exciton groundstate dispersion is found to lie below the shifted exciton continuum edge, i.e., the groundstate exciton binding energy becomes larger away from $Q = 0$. This can be understood based on the fact that for $Q \neq 0$ the groundstate exciton (5.3,5.4) is built from hole subband states around $(1-\beta_0)Q$. Due to the flatter subband dispersion around this point, i.e., the hole mass becoming heavier, the wavefunction can better adjust to the potential. The $LH_1C_1 - 1s$ exciton in the 20nm wide QW, Fig. 5.9b, is well separated from the spectrum of the HH_1C_1 exciton. We observe that at small Q the shifted exciton continuum edge lies above the $LH_1C_1 - 1s$ dispersion. Indeed, the LH_1 subband shows a negative mass at the Γ-point which becomes positive near the avoided crossing. Hence, the respective exciton has to pay with extra kinetic energy in order to achieve a small COM momentum and its binding energy is decreased. For larger Q values it gains again some binding energy.

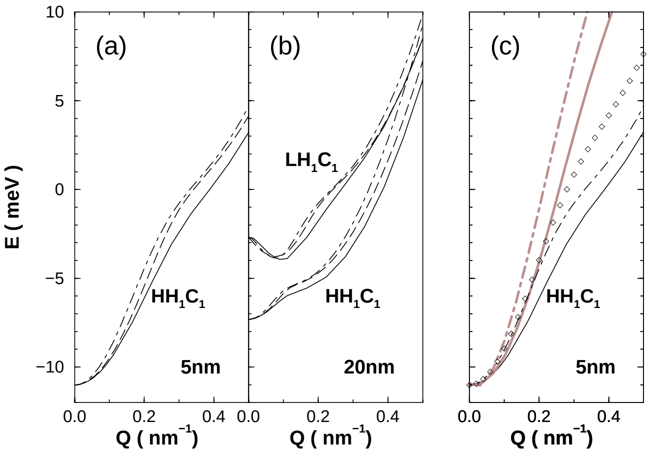

Figure 5.9: (a), (b): Comparison of the dispersion of $HH_1C_1 - 1s$ and $LH_1C_1 - 1s$ (20nm QW only) excitons (thick) with the appropriately shifted respective exciton continuum edge (dashed) and the underlying hole-subband dispersion (dot-dashed) for two GaAs/Al$_{0.3}$Ga$_{0.7}$As QW. (c): Comparison of our results (black) with those of Ref. [31] (gray) for the 5nm QW (shifted to match at $Q = 0$). The exact HH_1-subband dispersion for the parameters of [31] is plotted, too (diamonds).

5.1.1.5 Optical spectra

Having at hand the wavefunctions of the exciton states at vanishing COM momentum and the ones of the subband states, one can calculate the excitonic and non-interacting electron-hole absorption spectra as described briefly in Appendix D.

In Fig. 5.10 we plot the polarization-dependent exciton absorption spectrum for the 5nm QW. For the in-plane polarization the 3 : 1 ratio of the relative transition strengths for heavy and light holes almost survives. This is related to the relatively weak mixing of heavy- and light-hole bulk states in the exciton states for this QW; indeed, the $HH_1 - LH_1$ avoided crossing occurs at a distance greater than the inverse Bohr radius, Fig. 5.2(a), while the exciton is mainly constructed of the subband states in this region. The small admixture of light-hole bulk band-edge states to the groundstate exciton in this QW is more clearly seen in the left panel of Fig. 5.12. Another factor is the smearing out of the $LH_1C_1 - 1s$ exciton due to its resonance with the HH_1C_1 continuum, that leads to the asymmetric form of the respective lines [23, 99]. This resonance, however, is not very likely to result in a Fano resonance feature in the absorption spectrum, as the $LH_1C_1 - 1s$ exciton couples mainly to $HH_1C_1 - nd$ excitons, which are not optically active. A Fano resonance has been experimentally observed in GaAs/AlAs QW for the $HH_3C_1 - 1s$ exciton line [100], which couples mainly to the optically active states of the HH_1C_1 continuum [101].

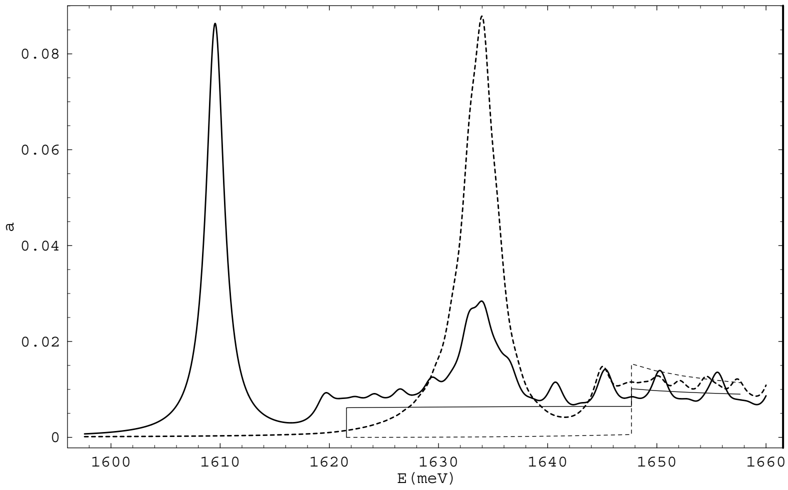

Figure 5.10: Calculated absorption spectrum for the 5nm wide GaAs/Al$_{0.3}$Ga$_{0.7}$As QW with polarization $\hat{e} \parallel z$ (thick) and $\hat{e} \perp z$ (thick dashed). Shown (thin and thin dashed) are also the respective polarization-dependent spectra for the non-interacting electron-hole system. We used the values $\hbar/m_0\, p^w_{cv} = 1.05$eVnm and $\hbar/m_0\, p^b_{cv} = 1$eVnm for the interband dipole matrix element of the well and barrier material, respectively, and a Lorentzian inhomogeneous broadening of half width $\gamma = 1$meV. The dimensionless absorption coefficient a is given in absolute values.

A Sommerfeld enhancement factor slightly greater than unity, i.e., substantially less than the expected factor of 2 for the ideal 2D case, can be seen at the onset of the HH_1C_1 absorption continuum for the in-plane polarization, revealing that the system is still far from being strictly two-dimensional. For polarization parallel to the growth direction, the Sommerfeld factor at the onset of the LH_1C_1 absorption continuum is even less than unity; However, this feature is related to the negative dispersion of the LH_1 subband, which yields a peak in the density of states rather than to the 2D step-like one [76]. It resembles the findings in QWR, where the inverse-square-root singularity at the band edge in the density of states is suppressed in the absorption spectra.

5.2 Solution in real space

For effectively two-dimensional structures with translational symmetry like the considered symmetric QW in axial approximation and, maybe, for some highly idealized quantum wire structures, the real-space method we present in this section can not compete with the one in k-space. But for realistic one-dimensional structures, like V-groove and T-shaped quantum wires, this may be the only feasible approach for calculating the exciton groundstate dispersion. This is due to the high number of confining dimensions for the exciton (in quantum wires four, two for each particle): an expansion in a problem-adapted basis like the product basis of the one-particle eigenstates, for which one expects reasonable convergence, leads to four-dimensional integrals for the Coulomb interaction, while an expansion in a basis where the Coulomb potential is not a problem will probably show a very slow convergence with basis size.

The calculations we report in this section on QW are mainly to be viewed as tests of the applicability of our real-space approach and of its generalization to finite-elements discretization. They are primarily compared with results obtained with the more established k-space methods. We will therefore discuss the results of the real-space calculations focusing on the convergence properties of the method and on the analysis of features of the wavefunctions more easily visualized in real space such as, e.g., the electron-hole correlation in the growth direction.

5.2.1 Discretization of the Coulomb potential

In order to attain a simple discretization for the interaction of some Hamilton operator, Glutsch, Chemla, and Bechstedt [102] proposed to discretize on the same mesh another operator whose groundstate is analytically known with the same interaction but with another kinetic operator, e.g., with another mass m^{ref}. We will call the latter in the following the reference system; to associated parameters a superscript ^{ref} will be assigned. For illustration, consider a simple one-dimensional system with known groundstate g of energy E_g^{ref} discretized on a mesh $\{x_i\}$ of size Δ_x. The discretized Schrödinger equation of the reference system

$$-\frac{\hbar^2}{2m^{ref}\,\Delta_x^2}\,(g(x_{i+1}) - 2g(x_i) + g(x_{i-1})) + V(x_i)\,g(x_i) = E_g^{ref}\,g(x_i) \qquad (5.20)$$

yields the groundstate-adapted discretization

$$V(x_i) = E_g^{ref} + \frac{\hbar^2}{2m^{ref}\,\Delta_x^2}\,\frac{g(x_{i+1}) - 2g(x_i) + g(x_{i-1})}{g(x_i)}\,,\quad g(x_i) \neq 0\,. \qquad (5.21)$$

The requirement for the wavefunction g not to vanish on the mesh is easily met by groundstate functions, that are nodeless. This procedure is very simple, easy to implement, cheap to calculate, and gives for the reference system always the correct groundstate energy, regardless how inappropriate the mesh is. In addition, no special handling for potentials with integrable singularities is needed.

Using this discretization for a reference state similar enough to the one sought, one may expect good convergence with mesh size. In order to check how the dependence of the potential discretization on the reference state influences the results, we performed calculations of the ideal 2D- and 3D-excitons using discretization of the Coulomb potential based on reference excitonic ground states with various Bohr radii. Fig. 5.11 shows the lowest numerical eigenvalues

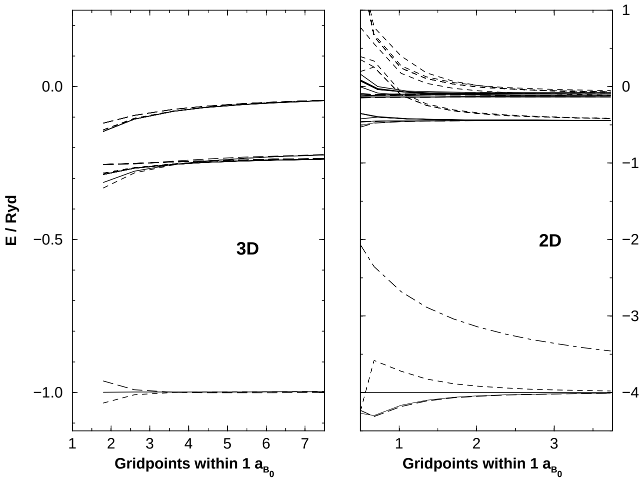

Figure 5.11: The lowest eigenvalues calculated in real space of the ideal 3D exciton (left) and 2D exciton (right) of Bohr radius a_{B0} plotted versus grid density. Discretization of the Coulomb potential as described in the text with reference Bohr radius a_B^{ref}: a_{B0}(thick), $2\,a_{B0}$(dashed), $a_{B0}/2$ (long dashed). For the 2D case, also results are shown with the potential integrated analytically in every mesh cell, Eq. (5.22), (thin) and for the ground state with the "naive discretization" (dot-dashed). The former curves are hardly to distinguish from the ones for $a_B^{ref} = 2\,a_{B0}$.

as a function of grid point density. One can see that the correct estimation of the "unknown" ground state is not so critical: a reference Bohr radius a_B within a factor of two from the actual one, a_{B0}, still gives good results for the ground state for reasonable mesh densities. Apparently, especially for the 2D case, it is better to choose a_B rather larger than smaller in order to get good results also for the excited states.

We also show for the 2D case the results obtained with the potential integrated analytically on each Cartesian mesh element yielding

$$\int^x\!\!\int^y \frac{d^2\vec{r}}{r} = \ln\left\{\left(x+\sqrt{x^2+y^2}\right)^y \left(y+\sqrt{x^2+y^2}\right)^x\right\},\ (x,\,y) \neq (0,\,0). \tag{5.22}$$

This procedure gives also a very good convergence with the mesh size. The 2D result obtained for the ground state with the potential integrated analytically only at the origin, and taking everywhere else its value at each center ("naive" discretization) is included in Fig. 5.11. Since both discretizations are the same at the origin, the difference does not originate from the divergence at this point. The superiority of the discretizations (5.21) and (5.22) is obvious. We therefore expect (5.21) to yield good results even with not very dense meshes.

For the 3D case, a similar expression to Eq. (5.22) for the Coulomb potential integrated analytically on a rectangular box can be derived. However, we could not use this result to obtain an alternative discretization for the real-space QW calculations because the natural mesh $(\rho_x, \rho_y, z_e, z_h)$ is not Cartesian in the relative coordinate $z_e - z_h$.

5.2.2 Results for GaAs/Al$_{0.3}$Ga$_{0.7}$As quantum wells

For the real-space calculations at finite Q, we used the optimized β_0 obtained in the respective k-space calculations. We could have used equally well some other procedure to find the effective Bohr radius a_B, e.g., a variational one, or we could also have fitted a 2D-1s exciton function to the in-plane probability distribution of the previously calculated exciton groundstate at $Q = 0$.

The Coulomb potential was discretized as described in Sect. 5.2.1. The 3D 1s-exciton in the four dimensional space $(\vec{\rho}, z_e, z_h)$ with $m_e^{ref} = 0.0665\, m_0$, $m_h^{ref} = 0.24\, m_0$ was used as reference groundstate. The value for the reference hole mass was taken from Fig. 6.1, discussed below, as an average value for the range of QW widths considered. This gives a reasonable reference Bohr radius of $a_B^{ref} = 12.2$nm; it is about the correct value for the in-plane motion or somewhat larger. In the confinement direction the size of the reference wavefunction is larger than the actual one (the exciton is quenched in this direction), too. As discussed in Sect. 5.2.1, a reference Bohr radius as large as or somewhat larger than the actual one gives good convergence. We did test calculations with a_B^{ref} doubled and with a_B^{ref} halved and found a qualitatively similar behavior as in Fig. 5.11. The integration region was 120nm wide in the $\vec{\rho}$ directions and 30nm (60nm) wide in the z directions for the 5nm (20nm) QW; this corresponds to a grid points density of about $6/a_B$ in the in-plane directions.

The resulting matrix is a sparse, complex hermetian of dimension up to $\approx 1.4 \cdot 10^7$ for grids fine enough to yield well converged results for the exciton dispersion. We used for this task the freely available iterative sparse matrix eigenproblem solver ARPACK [103, 104]. Some details concerning the numerical implementation are discussed in Appendix E.4.

The panel in the middle of Fig. 5.12 shows dispersions of the lowest exciton states (diamonds) from the real-space calculation for a 5nm wide QW. The exciton dispersions calculated in momentum space are plotted as full curves for comparison. The groundstate binding energy is not yet fully converged: all real-space results were shifted approximately 1meV to lower energies to match the groundstate energies at $Q = 0$ for both methods. Numerical tests show that the density of grid points in the growth direction (ca. 0.6 points/nm) is more critical than in the in-plane direction (ca. 0.6 points/nm); the exciton continuum edge lies also 0.5meV too high and the stronger confinement due to the Coulomb interaction lets us expect for the exciton a larger deviation. Nevertheless, the groundstate relative dispersion, $\mathcal{E}_g^X(Q) - \mathcal{E}_g^X(0)$, is converged and reproduces the k-space results very well. We remark, that in the case of parabolic one-particle dispersions this is an exact property of numerical exciton dispersions. The dispersions of the excited states calculated are not reproduced

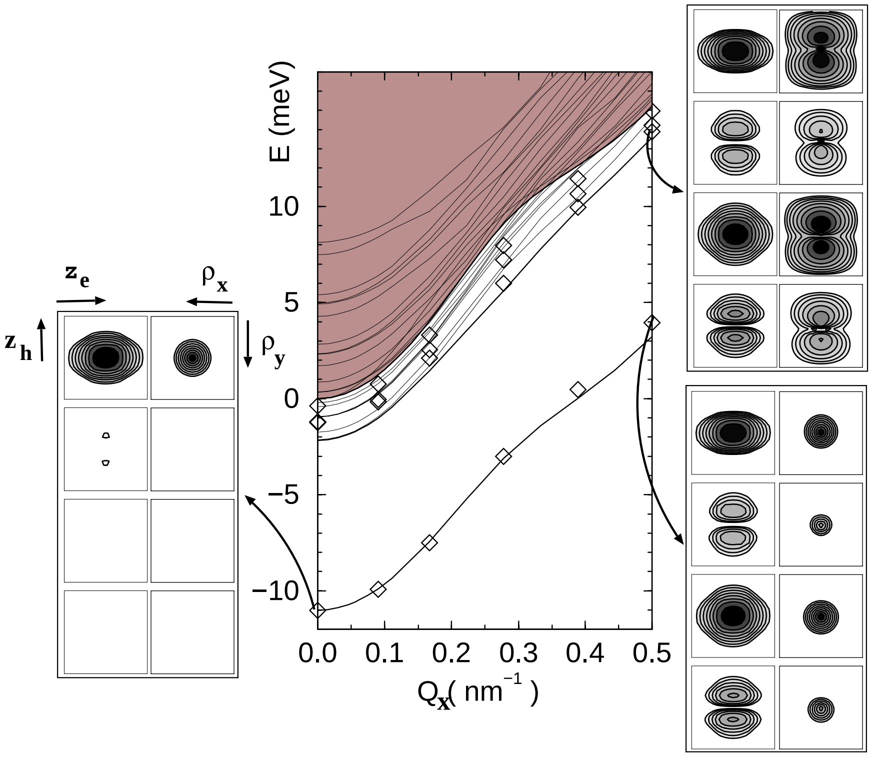

Figure 5.12: Middle panel: Exciton dispersion for a 5nm wide QW; notation, symbols and shading are the same as in Fig. 5.5. Side panels with logarithmic contour plots of the exciton probability distribution for each spin-component (from top to bottom $m_J = +\frac{3}{2}, +\frac{1}{2}, -\frac{1}{2}, -\frac{3}{2}$) are shown for characteristic exciton states at $Q = 0$ (left) and $Q_x = 0.5\mathrm{nm}^{-1}$ (right). The displayed area is in each direction $2\,L$ wide for the $z_e z_h$ plots and about $10\,a_B$ wide for the $\rho_x \rho_y$ plots, respectively.

that well. This is mainly due to their larger spatial extension and smaller energy separation from each other compared to the ground state.

The panels on the left and on the right in Fig. 5.12 show logarithmic contour plots of the exciton probability distribution for some characteristic states. The probability distribution is either integrated over z_e, z_h and displayed in the $\vec{\rho}$ plane or integrated over $\vec{\rho}$ and displayed in the $z_e z_h$ plane for each spin component separately. The numerically obtained wavefunctions are a linear combination of the two degenerate solutions with opposite parity (3.10). They are disentangled according to parity P, and only $P = -1$ states are displayed.

The lower left panel displaying the groundstate exciton at $Q = 0$ illustrates its $HH_1C_1 - 1s$ character: the main spin component is $m_J = +3/2$ and has no nodes. The bulk of the exciton is confined in the QW but there is substantial penetration into the barrier, being stronger for the lighter electron (we remark, however, that the plots are logarithmic). At $Q = 0.5\text{nm}^{-1}$ the groundstate exciton has still a $HH_1C_1 - 1s$ character, as is seen in the k-space calculations, Fig. 5.4. This does not contradict the strong mixture of heavy and light hole bulk states seen in the lower right panel. Indeed, the exciton is built from hole subband states near $(1 - \beta_0)Q$. This point lies past the $HH_1 - LH_1$ avoided crossing. Hence, the HH_1 subband states near this point are a strong mixture of heavy and light hole bulk band edge states. The stronger penetration into the barrier of the light hole component is again related to its smaller mass.

An interesting feature is the larger confinement of the $m_J = +\frac{3}{2}$ component at $Q = 0.5\text{nm}^{-1}$ compared to $Q = 0$. This is a consequence of the enhanced exciton binding energy. Altogether, the plots demonstrate that the total charge distribution in not altered much with increasing COM momentum; the somewhat stronger confinement of the heavy hole is at least partly canceled by the larger penetration into the barrier of the light hole. Although here not clearly resolved, the in-plane plots at $Q = 0.5\text{nm}^{-1}$ show the slight deformation of the originally radially symmetric wavefunction that was seen in Fig. 4.2. Again these deformations partly cancel each other in the sum over the spin components, and the in-plane charge distribution remains mainly symmetric. This is more clearly seen for the first excited state at $Q = 0.5\text{nm}^{-1}$ which has a HH_1C_1-$2p_y$ character (upper right panel in Fig. 5.12). The latter is the $HH_1C_1 - 2p_+$ exciton, which is, again, slightly lower in energy than the $HH_1C_1 - 2p_-$ exciton at $Q = 0$. At large Q the character of the HH_1C_1 envelope changes from $2p_\pm$ to $2p_{y,x}$ respectively.

One does not expect strong electron-hole correlation in the growth direction for the 5nm QW, which is considerably narrower than the exciton Bohr radius; the confining potentials are in average much stronger than the Coulomb potential and the wavefunction cannot relax in this direction. Indeed, in Fig. 5.13a the probability density integrated over $\vec{\rho}$ does not show much correlation: the contour lines are not elongated in the $z_e = z_h$ direction. However, some correlation exists as the plot of the cut at $\rho = 0$ in Fig. 5.13b demonstrates. This weak correlation is not included in our k-space calculations where only one conduction band was used. Its envelope does not depend on k and consequently the z_e coordinate can be separated, Eq. (5.3).

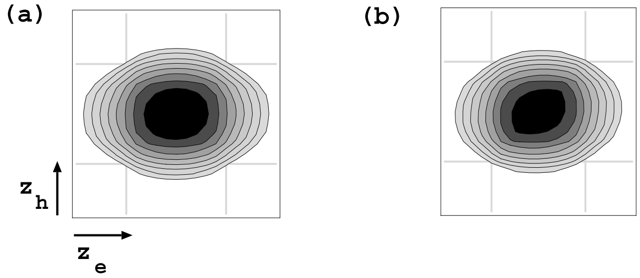

Figure 5.13: Groundstate exciton probability density in the $z_e z_h$-plane for the main spin-component ($m_J = +\frac{3}{2}$) at $Q = 0$ for a 5nm wide QW, (a) integrated over the in-plane relative coordinate $\vec{\rho}$ (same as lower left corner of Fig. 5.12) and (b) at $\vec{\rho} = 0$. The background lines mark the position of the QW interfaces.

In Fig. 5.14, results are displayed for a 20nm wide QW. Two set of points are shown for two different mesh sizes. The energies of the groundstate exciton are almost converged for the more dense mesh; the deviation from the results of the k-space calculations is only 0.2meV at $Q = 0$.

The small, but noticeable $m_J = +1/2$ component of the groundstate exciton $HH_1C_1 - 1s$ exciton in the lower left panel corresponds to the substantial admixing of the $LH_1C_1 - d_-$ exciton seen already for the 15nm QW in Fig. 5.4. The admixing is larger for wider QW due to the smaller energy separation of the respective subbands. At $Q = 0.5\text{nm}^{-1}$, the groundstate exciton has mainly bulk light-hole character ($m_J = -1/2$). This again does not contradict the $HH_1C_1 - 1s$ character since the HH_1 subband has beyond the avoided crossing with the LH_1 subband approximately 60% light-hole character. The first excited state at $Q = 0.5\text{nm}^{-1}$, which is the $LH_1C_1 - 1s$ exciton, has also $LH_1C_1 - 1s$ character even though an additional node is seen in the $z_e z_h$ probability distribution of the main spin component ($m_J = +1/2$); the envelopes of the single-particle subband states at large enough in-plane momentum show more nodes than at the Γ-point due to the coupling of in-plane and growth directions in the Luttinger Hamiltonian. This is one of the reasons why the expansion Eqs. (5.3,5.4) gives very good results with just two subbands, while an expansion in the subband states at the Γ-point [31] needs more subbands for the same accuracy.

The probability distribution plots illustrate the almost vanishing penetration into the barriers for the wide QW, in contrast to the narrower QW of Fig. 5.12. All panels show also a clear orientation of the contour lines towards the $z_e = z_h$ diagonal. This fact demonstrates the presence of considerable electron-hole correlation in the growth direction for QW wider than one Bohr radius. Still, the stronger correlation has little impact on the energies. Recall that in perturbation theory the first order correction to the wavefunction gives only a second order correction to the energy. This justifies the usual factoring out of the dependence on the growth direction for the much lighter electron

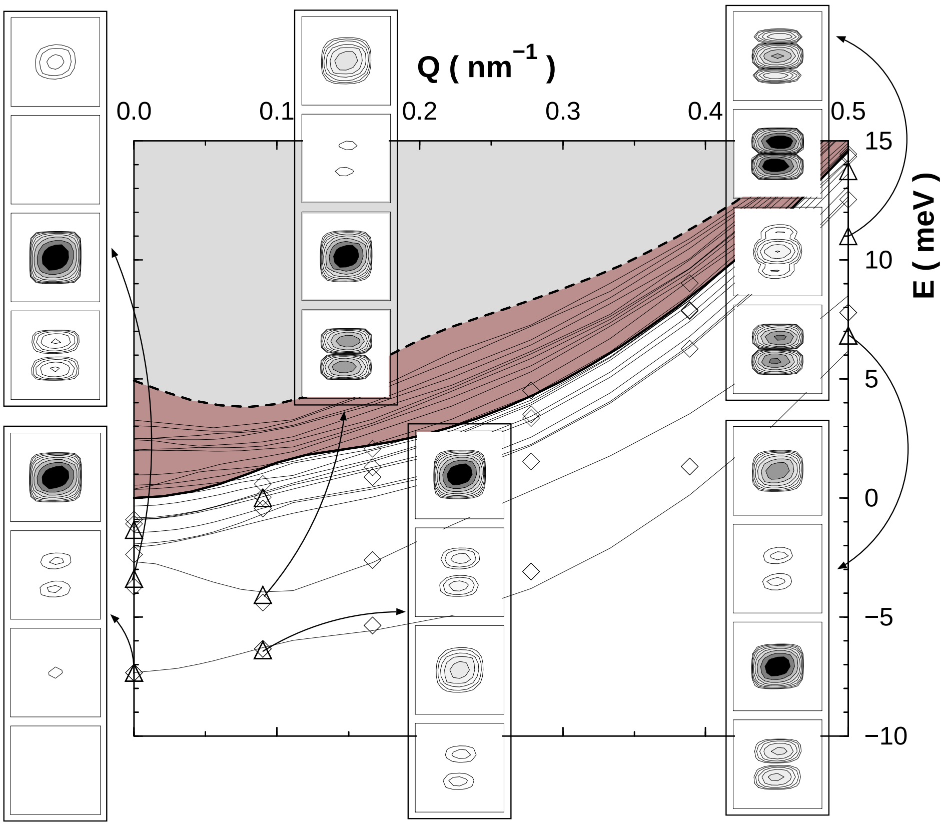

Figure 5.14: Logarithmic contour plots of the exciton probability distribution in the $z_e z_h$-plane for each spin-component (in each panel from top to bottom $m_J = +\frac{3}{2}, +\frac{1}{2}, -\frac{1}{2}, -\frac{3}{2}$) for the $HH_1C_1 - 1s$ and the $LH_1C_1 - 1s$ excitons at some characteristic Q-values for a 20nm QW. The displayed region extends in each direction twice the QW width. The triangles (diamonds) show results of the real-space calculations for a dense (less dense) mesh. The notation for the background panel is the same as in Fig. 5.5. We do not show the HH_2C_1 continuum that lies partly in the displayed region.

$\psi(\vec{\rho}, z_e, z_h) \approx \xi(z_e)\phi(\vec{\rho}, z_h)$.

This, in contrast, is not the case for the much heavier hole. It is a well known fact, that the Coulomb coupling of the hole subbands is considerable. Indeed, for the 20nm wide QW neglect of the Coulomb coupling of the HH_1C_1 and LH_1C_1 excitons leads to an error in the HH_1C_1 groundstate binding energy larger than 10%. That is, the correlation of in-plane and confinement directions for the hole is substantial.

To check the relevance of the optimized COM transformation also for real-space calculations, we performed for the 20nm QW a single calculation at $Q = 0.5\text{nm}^{-1}$ with $\beta = 1$. Indeed, the so calculated groundstate energy lies very far (43meV!) above the correct value.

Chapter 6

Exciton Mass

Although it is well known that the single-particle and exciton dispersions in bulk semiconductors as well as heterostructures are, apart from a few exceptions, nonparabolic, the concept of a mass assigned to them is widespread. This is, of course, due to the great simplicity of models involving parabolic dispersions. Such models allow to focus on the physics one is interested in without having to deal with all the features of the underlying dispersions, and they are, thus, of great practical importance.

When the involved dispersions are not parabolic and a well-defined mass does not exist, some "relevant" mass has to be defined, which reproduces on average that part of the dispersions that is of concern. Hence, different relevant mass values can be assigned to the same dispersion depending on the momentum range or other features involved in the physical process. It is, therefore, important to keep always in mind the context of each particular mass value.

However, one does not usually want to calculate first the exciton dispersion, which is, at least in heterostructures, numerically a very challenging problem, in order to make the averages necessary for simple masses. Hence, methods are necessary that yield good estimates for the desired relevant masses based on much simpler ingredients. In the following two sections, we introduce such an estimate for the exciton relative mass as well as one for the COM mass, and check their validity for various QW systems. They are also compared to other approaches often applied in the analysis of experiments and the characterization of heterostructures. Our estimate for the exciton relative mass has been successfully applied in the study of magnetoexcitons, see Sect. 6.4.

The expression Eq. (4.7) obtained from perturbation theory for the exciton mass as the derivative of the exciton groundstate dispersions at $Q = 0$ introduced in Sect. 4.2, although conceptually interesting, will not be investigated further; it does not give very satisfactory results and, more importantly, it can not be calculated without a multiband wavefunction for the exciton groundstate at $Q = 0$ (because of the operator $H_h^{(2)}$ in Eq. (4.7)). Indeed, if one does not use a multiband exciton groundstate wavefunction, one simply gets the masses of the diagonal approximation.

6.1 Analytical formula for the groundstate center-of-mass mass

In Sect. 4.3 a method has been proposed for optimizing the COM transformation. Therein, the analytical variation that led to the optimized β, Eq. (4.17), gives the groundstate energy up to terms quadratic in Q. The corresponding groundstate kinetic mass M_g^X has again the form

$$M_g^X = m_e^X + m_h^X \tag{6.1}$$

with the COM-related masses for electron and hole defined as

$$1/m_{e,h}^X = \frac{1}{\hbar^2} \sum_{n_e n_h} \int d\vec{k} \,|\, \varphi_{n_e n_h}^{0;\,g}(\vec{k}) \,|^2 (\hat{Q} \cdot \vec{\nabla})^2 \mathcal{E}_{e,h}(\vec{k}). \tag{6.2}$$

With these masses, the expression for β_0 (4.17) has the same form as in the parabolic case (3.8). Eq. (6.2) give the right results for the free-particle case.

Eq. (6.2) is physically appealing: it leads to a weighted average of the subband dispersion *curvatures*. This is perfectly reasonable, since the COM energy is a difference effect: it is the in(de-)crease in energy of the exciton when attaining some finite COM momentum Q.

This simple result can be of considerable practical importance. The semi-analytical expressions (6.1,6.2) are relatively simple to calculate. They require only the approximate knowledge of the envelope of the $Q = 0$ exciton [22, 23, 24, 25, 26, 28, 27, 29] and of the dispersion of the involved subbands. The numerical calculation of subband dispersions is nowadays an easy task (provided the $\vec{k} \cdot \vec{p}$ parameters are known). Moreover, especially for narrow QW, the envelope of the HH_1C_1 component of the groundstate exciton is to a very good approximation similar in shape to the groundstate of the 2D exciton, Eq. (5.18) (see Fig. 5.4, 5.7). The LH_1C_1 component is quite small e.g. 5% for the 20nm QW and can be safely neglected in this context. Therefore, only a good estimate for the effective Bohr radius a_B is needed to evaluate (6.2) and (6.1).

6.2 Exciton groundstate mass in GaAs/Al$_{0.3}$Ga$_{0.7}$As quantum wells

The expression for the kinetic mass of the groundstate exciton, Eq. (6.1,6.2), was introduced in the process of determining the optimal choice of the COM coordinate system of Sect. 4.3. Two assumptions were essential: (i) the Coulomb potential, i.e., the form factors, are a function of the in-plane momentum transfer only and (ii) the shifted exciton-envelope Ansatz (4.13) is valid. The numerical results of the previous sections support these assumptions.

Together with the exciton dispersions in Fig. 5.5, we displayed for the groundstate exciton a parabola with the exciton mass M_g^X of Sect. 5.1.1.2. This mass is obviously not the one determined by the curvature of the exciton

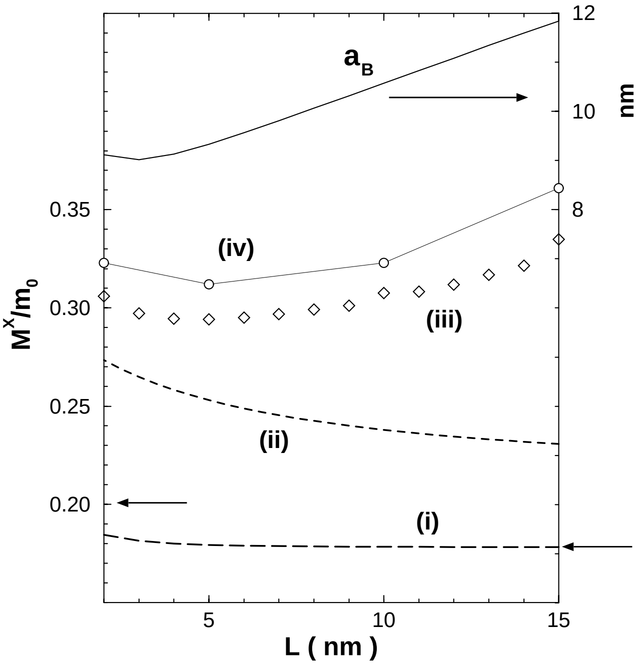

Figure 6.1: Exciton average kinetic mass in various approximations and Bohr radius a_B versus well width L for GaAs/Al$_{0.3}$Ga$_{0.7}$As QW. The figure is discussed in detail in the text.

groundstate dispersions at $Q = 0$. It is rather an average of the curvature of the groundstate dispersion in a region with size given by $1/a_B$. Indeed, this is implied by Eq. (6.1,6.2) and the observation made in Sect. 5.1.1.4 that the groundstate dispersion follows closely the respective exciton continuum edge.

This exciton COM momentum region is the one important for exciton localization due to, e.g., well width fluctuations, interface roughness, or alloy fluctuations in QW [10]. Indeed, the exciton averages over smaller scale fluctuations due to its finite size and feels an effective disorder potential that is spatially correlated over the Bohr radius a_B.

The dependence of various expressions for the groundstate exciton mass on the QW width L is displayed in Fig. 6.1. The conduction band mass was taken material-independent $m_e^{b,w} = 0.0665$, the shown L-dependence comes solely from the valence band. Displayed are the masses obtained by: (i) describing the hole in the diagonal Luttinger approximation $1/m_h = P_w\,(\gamma_1^w + \gamma_2^w) + P_b\,(\gamma_1^b + \gamma_2^b)$, where $P_{w,b}$ denote the probability that the hole is in the well and barrier material, respectively, (long dashed), (ii) taking as hole mass the subband curvature at the Γ-point (dashed), that is known analytically (see Appendix A), (iii) using our semi-analytical expression for the mass (6.1,6.2) with a 2D $1s$ exciton function fitted to the envelope of the HH_1C_1 component (diamonds), and (iv) the average of the curvature of the numerical exciton dispersion weighted with the same function as (iii) (circles, the line is a guide to the eye).

The top curve displays the values for the Bohr radius that we used for the calculation of (iii) and (iv). Arrows at either sides of the lower part of Fig. 6.1 mark the mass in the diagonal approximation, Eq. (2.15), in the well and barrier bulk materials.

Fig. 6.1 demonstrates the failure of the diagonal Luttinger approximation (i) to describe even the HH_1 subband curvatures at the Γ-point due to the degeneracy of heavy- and light-hole bands in the unstrained bulk. However, even the correct single-particle subband curvatures at the Γ-point (ii) fail to describe accurately the curvature of the groundstate exciton dispersion at $Q = 0$. This is mainly due to the finite extension of the exciton in k-space that implies an averaging of the subband dispersions over a region of approximately $1/a_B$ near the Γ-point and partly to the Coulomb coupling to higher subbands. Both effects tend to make the groundstate exciton heavier. The mass derived from the curvature of the groundstate exciton at $Q = 0$ (not shown) lies between curves (ii) and (iii).

The numerically obtained "best" mass values (iv) show a behavior quantitatively and qualitatively different from that of curves (i) and (ii). For very narrow QW, the subbands become flatter at the Γ-point because of the larger penetration into the barriers where the exciton becomes again heavier, as in models (i), (ii). But, for large L the region of the HH_1-LH_1 avoided crossing comes to a distance of approximately $1/a_B$ to the Γ-point and the exciton, averaging over the flatter subband dispersion, becomes heavier.

The quality of our semi-analytical result for the average exciton mass (iii) has to be judged according to its deviation from the numerical average (iv). The non-monotonous behavior is clearly seen for the mass (iii) obtained using only the HH_1 subband dispersion and the fitted Bohr radius. The mass values (iii) are somewhat smaller (<10%) than the ones of curve (iv). This is due to the enhancement of the binding energy for $Q \neq 0$ that yields larger average masses (iv) than one would expect based on the one-particle subband dispersions and the $Q = 0$ groundstate exciton. Our semi-analytical average groundstate exciton mass, (iii), reaches a minimum approximately at the QW width where the maximum binding energy is reached.

The small differences between curves (iii) and (iv) demonstrate the quality of our expression, Eq. (6.2, 6.1), for the average exciton groundstate mass. For this reasonable and easy to use mass expression, only a good estimate for the in-plane Bohr radius and the dispersion of the involved single-particle subbands is needed.

In the paper by Triques and Brum [31], average exciton effective masses were calculated that are relevant to the formation process of excitons in two different scenarios. These masses are defined by parabolic fits within a relevant energy range of: (a) 5meV, approximately half the exciton binding energy, in the case that the particles first relax and then form an exciton of kinetic energy lower than the binding energy and (b) 36meV, in the case that the exciton is formed very fast and relaxes initially via optical phonon emission, reaching energies below 36meV, the energy of the GaAs-LO phonon. These energy ranges translate to Q values in general much larger than $1/a_B$. Therefore, these average masses should be larger than those of the present work. However, the values published in Ref. [31] for the 5meV mass ($0.2m_0 \leq M_g^X \leq 0.3m_0$ for $L \leq 10$nm) are smaller than ours for narrow QW. Our average masses of scenario (a) never fall below $0.3m_0$ and show a smooth minimum for a QW of width somewhere between 2nm and 5nm. This difference can be traced back mainly to the inefficiency for narrow QW of their method involving an expansion in the subband states at the Γ-point, as already remarked by the authors themselves. Indeed, for narrow QW the few states at the Γ-point can not provide the needed flexibility to simulate states far away from the Γ-point, see the discussion in Sect. 5.2.2. This is substantiated by the lower left panel in Fig. 5.12 showing the groundstate exciton at $Q = 0.5\text{nm}^{-1}$ for the 5nm QW. The $z_e z_h$-plots show a substantial $m_J = +\frac{1}{2}$ spin component. In an expansion of the z_h dependence in the hole subband states at the Γ-point, this component would need a LH_2 subband to be described efficiently. However, for the 5nm QW only the HH_1, LH_1, HH_2 subbands exist below the top of the barrier.

In Fig. 5.9(c), we compare the results of Ref. [31] with ours for the 5nm QW. For this narrow QW, their exciton and HH_1 subband dispersions are much steeper than ours. The discrepancy is not due to the different parameters as a comparison with the subband dispersion calculated exactly with the transfer matrix method for the parameters of Ref. [31] demonstrates (diamonds).

6.3 Exciton relative mass

There is also a large class of exciton problems, where the focus lies on the interplay of an external perturbation with the relative motion of the exciton. For such systems a mass is needed for the relative part of the exciton motion, which we will call the exciton relative or reduced mass and denote with μ.

A reasonable definition for such a mass parameter is obtained when requiring that the kinetic energy of the exciton at rest (COM momentum $Q = 0$) in the absence of the external perturbation is reproduced exactly. Using the subband expansion of the exciton wavefunction at vanishing COM momentum, Eq. (4.8), this leads to the usual expression for the exciton relative mass

$$\frac{1}{\mu^{X;\,a}} = \frac{1}{m_e^{rel}} + \frac{1}{m_h^{rel}} \tag{6.3}$$

with the following expressions for the hole and electron effective masses related to the relative exciton motion

$$1/m_{e,h}^{rel} = \frac{2}{\hbar^2} \frac{\sum_{n_e n_h} \int d\vec{k}\, |\, \varphi_{n_e n_h}^{0;\,a}(\vec{k})\, |^2 \, \left(\mathcal{E}_{n_{e,h}}(\vec{k}) - \mathcal{E}_{n_{e,h}}(0)\right)}{\sum_{n_e n_h} \int d\vec{k} \left|\varphi_{n_e n_h}^{0;\,a}(\vec{k})\right|^2 k^2} \,. \tag{6.4}$$

The masses (6.4) are weighted averages of the subband dispersions themselves, and not of the second derivative of the subband dispersions as is the case in Eq. (6.2). Again, only the portion of the subband dispersions in the momentum range of $1/a_B$ around the Γpoint is relevant. These expressions are easy to calculate, provided the single-particle subband dispersions and a good estimate for the effective Bohr radius a_B are known. The expressions above can be evaluated for each exciton state a separately.

We display in Fig. 6.2 the mass values for the hole in the exciton after Eq. (6.4) for various exciton states and QW widths. Some general trends are seen; for the same QW the mass decreases (at least for the excitons of the lowest subband) within an ℓ-series with higher energy, which is due to the wavefunctions becoming more extended in real space and, hence, more concentrated near $k \simeq 0$ in k-space. This weights higher the steeper low-energy part of the subband dispersion. The more nonparabolic the underlying subband dispersions are, the more pronounced is the dependence of the relative mass on the “main quantum number”. For this very reason, the dependence on the QW width shows a similar behavior as the COM-related mass in Fig. 6.1 which is, as described in the previous section, related to the variation of the exciton confinement and, hence, of the Bohr radius a_B with L.

A second general trend is seen in Fig. 6.2 and more clearly in Fig. 6.6 below for a ZnSe/$\mathrm{Zn_{0.85}Mg_{0.15}Se}$ QW: the relative masses tend to group together for a whole ℓ-series. This feature is related to the ℓ-dependence of the Coulomb coupling between excitons from different subbands, Eq. (5.17), which leads to different admixture ratios. This effect is the more pronounced the stronger the Coulomb interaction, i.e., for narrow wells with stronger exciton confinement and for material systems with low dielectric constants.

Although the variation of the relative hole mass for a given QW seen in Fig. 6.2 is relatively large ($\sim 10\%$), the mass values from other simpler approximations, like, e.g., the diagonal approximation, Eq. (2.15), lie almost a factor of 2 (see Fig. 6.1) away. In addition, for many relevant systems the electron mass dominates the relative exciton motion; for such systems one can safely neglect this mass dependence on the exciton state.

6.4 Magnetoexcitons in $\mathrm{Zn_{0.87}Cd_{0.13}Se}$/ZnSe and ZnSe/$\mathrm{Zn_{0.85}Mg_{0.15}Se}$ quantum wells

Magneto-optics is a powerful tool for studying exciton binding energies and band parameters in 2D-structures. Rich spectral features due to the field dependent shift and splitting of the exciton absorption lines in a Landau manner are seen in experiments. Fits to the experimental data yield high accuracy results for the model parameters (see [105] and references therein).

In Fig. 6.3 peak positions of polarized exciton absorption spectra as a function of the applied magnetic field B in Faraday configuration (applied field parallel to the growth direction) are shown for a 5nm $\mathrm{Zn_{0.87}Cd_{0.13}Se}$/ZnSe and

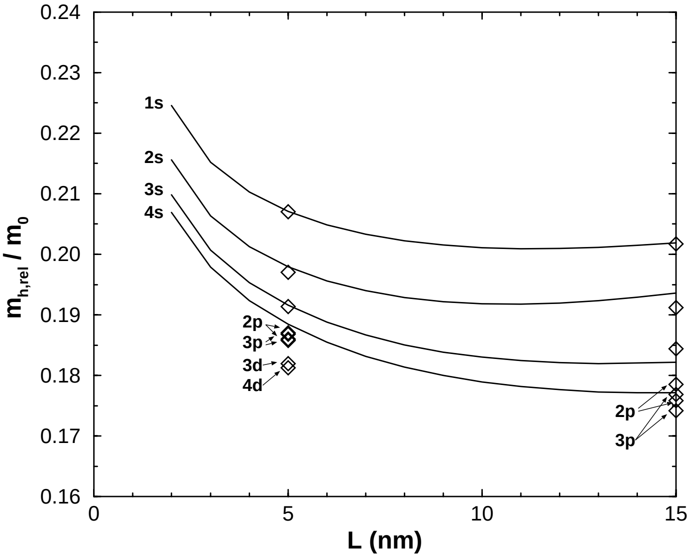

Figure 6.2: Hole mass for the HH_1C_1 exciton relative motion after Eq. (6.4) for the lowest lying $\ell = 0$ states versus well width L for GaAs/Al$_{0.3}$Ga$_{0.7}$As QW. For two well widths also the values for some $\ell \neq 0$ states are displayed. The lines are calculated on a twice as dense k-mesh than the diamonds.

a 4.5nm ZnSe/Zn$_{0.85}$Mg$_{0.15}$Se QW. Both material systems are under strain due to lattice mismatch; in the ZnCdSe QW the well material (Zn$_{0.87}$Cd$_{0.13}$Se) is under compressive strain, while the well material (ZnSe) of the ZnMgSe QW is under tensile strain. The opposite strain situation in the two systems results in a different alignment of the heavy- and light-hole exciton series. Indeed, the compressive strain in the ZnCdSe QW leads to a large separation of the HH_1 and LH_1 subbands (see Fig. 6.5); as a consequence, the $LH_1C_1 - 1s$ exciton lies in the continuum of the HH_1C_1 exciton and HH_1C_1 magneto-excitons up to the $6s$ state are observable. In contrast, the tensile strain leads to a LH_1 subband lying energetically lower than the HH_1 subband (see Fig. 6.4), the respective exciton series are intermingled.

The magnetic-field dependence of the observed spectral lines can, as a first step, be fitted quite well in a simple two-band model. The Hamilton operator used for the calculation of the B-dependence of the s-like excitons is

$$H \quad = E_g^{n_e n_h} + \frac{\hbar^2 k^2}{2\mu} + \frac{e^2}{8\mu}\left(\vec{B} \times \vec{\rho}\right)^2 + V_{Coul}^{n_e n_h}(\rho) \tag{6.5}$$

with the effective Coulomb potential

$$V_{Coul}^{n_e n_h}(\rho) \quad = \quad -\iint dz_e\, dz_h\, \phi_{n_e}^2(z_e)\phi_{n_h}^2(z_h)\frac{e^2}{\epsilon\,|\vec{r}_e - \vec{r}_h|}, \tag{6.6}$$

and $\phi_{n_{e,h}}(z_{e,h})$ the envelopes of the respective subband states calculated in the single-band approximation. $E_g^{n_e n_h} = E_g + \mathcal{E}_{n_e}(0) + \mathcal{E}_{n_h}(0)$ is the energy gap between the respective conduction and valence subbands, and $1/\mu = 1/m_e + 1/m_h$ is the relative exciton mass, which is taken different for the heavy- and light-hole exciton series. The material parameters entering Eq. (6.5) indirectly through the solution of the single-particle problem and Eq. (6.6), as well as μ and $E_g^{n_e n_h}$ are used as fit parameters.

As seen in Fig. 6.3, very satisfactory fits can be found in both cases. However, the fitted values for the relative exciton mass ($\mu_{hh}/m_0 = 0.114$ for the ZnCdSe QW and $\mu_{hh}/m_0 = 0.135$, $\mu_{lh}/m_0 = 0.125$ for the ZnMgSe QW) deviate remarkably from the ones obtained in the diagonal approximation from the ZnSe material parameters $\gamma_1 = 2.45, \gamma_2 = 0.61, \gamma_3 = 1.11, m_e = 0.147$ ($\mu_{hh}/m_0 = 0.101$, $\mu_{lh}/m_0 = 0.116$). The parameters for the other materials are not known. This is more clearly seen for the effective hole masses given in Tab. 6.1; there is a factor of approximately 2 or 3 between the fitted values and the ones expected in the diagonal approximation! This seems inappropriately large, especially when one considers the significant ($\sim$ 40meV) strain induced splitting of the heavy- and light-hole valence bands at the Γpoint that relaxes their strong coupling.

In Sect. 6.2 (see Fig. 6.1), the diagonal approximation was found to describe insufficiently the single-particle subband dispersions, the discrepancy being even larger for the COM exciton dispersions. In order to check whether the observed large deviation between the exciton relative mass in the diagonal approximation and the fitted values is reasonable, we performed [106, 19] full calculations of the exciton in the considered structures and calculated the expected relative masses after Eq. (6.3, 6.4). For the description of the valence band in the strained well materials, we used the strain operator (2.17), the corresponding deformation potential denoted as b. The parameters for the strain terms and the band offsets were those from the fit procedure of the experimental data; (a) for the 5nm ZnCdSe QW: $2b = -39.5$meV, $V_v = 24.85$meV, $V_e = 104.1$meV, (b) for the 4.5nm ZnMgSe QW: $2b = 39.2$meV, $V_v = 65.2$meV, $V_e = 152.1$meV. The dielectric constant was taken $\epsilon = 8.8$ for all materials.

The calculated subband dispersions for the ZnMgSe QW are plotted in Fig. 6.4. The deviation from the dispersions in the diagonal approximation is obvious. The large strain-induced splitting of the bulk valence bands has been reduced by the confinement. This is related to the stronger confinement of the light hole due to its smaller mass and the fact that the light-hole valence band is the energetically lowest one; the difference in the confinement energies is subtracted from the strain-induced splitting. The HH_1 subband is quite close to the LH_1 one, leading to a rather strong level repulsion and, hence, to a quite flat HH_1 dispersion. The situation is reversed for the compressively strained ZnCdSe QW, for which we show the subband dispersions in Fig. 6.5. For this system, the heavy hole band edge is the energetically lowest one and, although the confinement of the light hole is less than that of the heavy hole due to the very flat confining potential, the separation of the HH_1 and LH_1 subbands remains substantial. The HH_1 dispersion is, therefore, not as flat as the ones in the ZnMgSe QW.

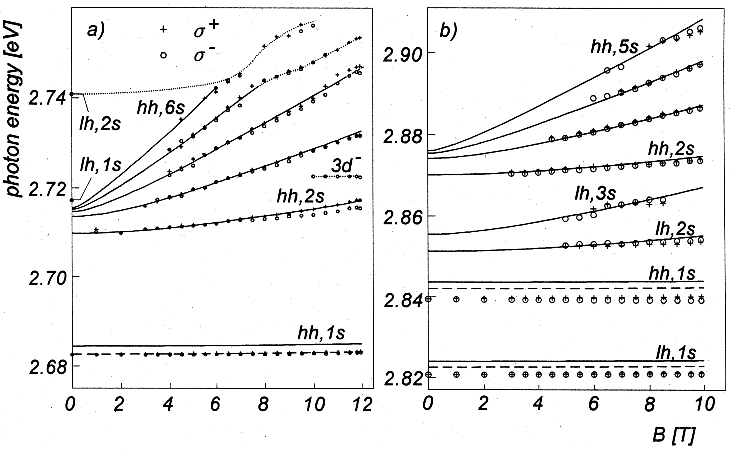

Figure 6.3: Dependence of (polarized) exciton absorption lines on the magnetic field in (a) a 5nm wide $Zn_{0.87}Cd_{0.13}Se/ZnSe$ and (b) in a $ZnSe/Zn_{0.85}Mg_{0.15}Se$ 4.5nm multiple QW, from [106, 19]. The lines are numerical fits based on the solution of a one-dimensional Schrödinger for s-like excitons at $Q = 0$ (lines) and on a variational Ansatz for the groundstate excitons (dashed) [105]. Dotted lines are just guides to the eye.

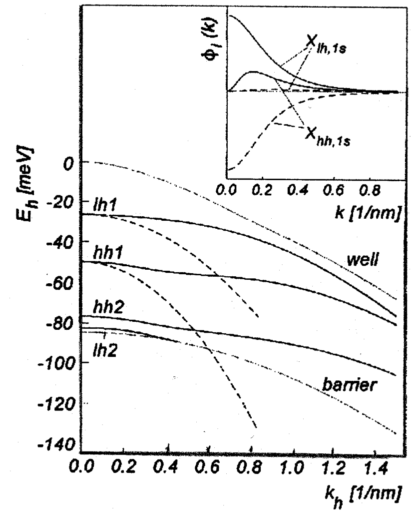

Figure 6.4: Subband dispersions (lines) for a $ZnSe/Zn_{0.85}Mg_{0.15}Se$ 4.5nm wide QW grown along the [001] direction. The well material (ZnSe) is under strong tensile strain leading to the LH_1 subband being the energetically lowest one. The bulk band edges (dotted) as well as the subband dispersions in the diagonal approximation (dashed) are also displayed. In the inset, the envelopes of the HH_1C_1 (line) and LH_1C_1 (dashed) components for the $HH_1C_1 - 1s$ and $LH_1C_1 - 1s$ exciton are shown.

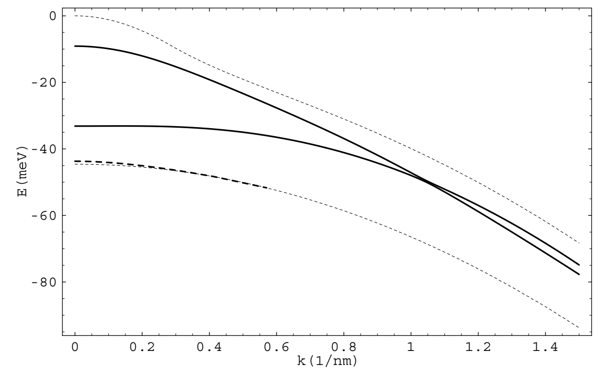

Figure 6.5: Subband dispersions for a 5nm wide $Zn_{0.87}Cd_{0.13}Se$/ZnSe QW. The well material is under compressive strain that pushes the LH_1 subband almost into the continuum. Displayed are the HH (line) and LH subbands (dashed), as well as the bulk band edges (dotted).

The very flat subband dispersions determine also the large relative exciton mass. In Fig. 6.6, we display the effective hole mass for the relative motion after Eq. (6.4) for the lowest bound exciton states in the ZnMgSe QW. In contrast to the $Al_xGa_{1-x}As$ QW, Fig. 6.2, almost constant mass values for each ℓ-series (including the $\ell = 0$-series!) are found. This is related to the stronger Coulomb interaction in these materials due to the small dielectric constant; the ℓ-dependent coupling of the heavy- to the light-hole exciton, Eq. (5.15), is respectively enhanced. In Tab. 6.1, we collect the theoretical and numerical hole relative mass values relevant for the lowest heavy- and light-hole excitons for both QW. Our theoretical results after Eq. (6.4) are in qualitative agreement with the numerical values. The deviations are due to the simplifications in the two-band model and, presumably, the fact that the used parameters were optimized for the fit of the experimental results to the one of the simple model rather than to the ones of our model.

	diag.	ZnMgSe, fit	ZnMgSe, th.	ZnCdSe, fit	ZnCdSe, th.
m_{hh}/m_0	0.33	0.84	1.4	0.51	0.58
m_{lh}/m_0	0.54	1.65	2.3	-	-

Table 6.1: Effective hole mass values for the two QW of Fig. 6.3 obtained from fitting of the experimental data as well as theoretical values obtained from Eq. (6.4) and numerically calculated multiband exciton wavefunctions. The mass values in the diagonal approximation, Eq. (2.15), for the material parameters of ZnSe are also given for comparison.

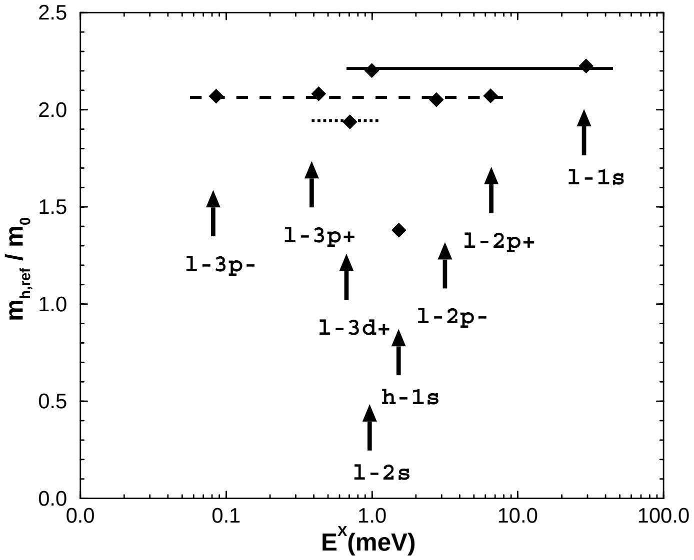

Figure 6.6: Effective hole mass for the relative motion, Eq. (6.4), for the lowest bound exciton states in the ZnSe/Zn$_{0.85}$Mg$_{0.15}$Se of Fig. 6.4. Rather well defined mass values are found for each ℓ-series. The excitons are named as defined in Sect. 5.1 with l standing for LH_1C_1 and h for HH_1C_1. The respective binding energies have been plotted on the horizontal axis. The COM related hole masses are $1.6m_0$ for the $HH_1C_1 - 1s$ exciton and $2.35m_0$ for the $LH_1C_1 - 1s$ exciton. Notice the strong splitting in energy of the $p_-$and p_+ states, which is due to the Coulomb coupling that is enhanced because of the small dielectric constant and reduced Bohr radius.

Chapter 7

Exciton Dispersion in Quantum Wires

We calculate single-particle and exciton dispersions for the particular V-groove QWR described in Sect. 3.3. The experimental wire cross-section was shown in Fig. 3.2, the central thickness of the wire region being approximately 6.3nm. The V-QW is modeled by a simple vertical slab with Al concentration $x = 0.21$, the slab placed approximately in the middle of the structure. A more detailed modeling, e.g., in order to take into account also the narrowing of the V-QW from the bottom to the top seen in Fig. 3.1, is easily possible within our approach, but seemed to be not necessary. The geometry of our QWR is seen as gray-scale background shading in the Figs. 7.2, 7.4, and 7.11 below. The material parameters that were used are summarized in Table 7.1.

$\mathrm{Al}_x\ \mathrm{Ga}_{1-x}\mathrm{As}$	QWR	barrier	V-QW
Al content x	0	0.33	0.21
gap E_g [eV]	1.519	1.931	1.781
Luttinger γ_1	6.790	5.8	6.16
parameters γ_2	1.924	1.695	1.778
(Ref. [42]) γ_3	2.681	2.257	2.411
electron mass m_e/m_0	0.0665	0.0941	0.0840
dielectric const. ϵ	12	12	12
offset ratio V_c/V_b	0.68/0.32	0.68/0.32	0.68/0.32

Table 7.1: Material parameters used for the V-groove quantum wire calculations.

7.1 Numerical solution

Numerical approaches to the exciton in QWR can be classified according to the chosen basis: The exciton wave function can be discretized in k-space, in real space, or it can be expanded into a superposition of simpler functions. The latter can be tight-binding orbitals, "arbitrary" orbitals with, e.g., Gaussian shape [34], or they can be derived from single-particle calculations for the confinement envelope functions. The simplest cases of the last approach are variational wavefunctions, which have been applied to QWR excitons by many groups in the last decade.

We presented in Sect. 5.1 for QW excitons full multiband calculations including $\vec{k}\cdot\vec{p}$ coupling in real space and compared them to calculations in $\vec{k}$-space involving a subband expansion. The real space approach to QW excitons was intended, besides for its own merits (wavefunctions, electron-hole correlation), as a first step towards the QWR results presented in this chapter. The finite momentum destroys already in the QW case the in-plane rotational invariance. With a resulting matrix dimension $\approx 1.4 \cdot 10^7$ for grids fine enough to yield well converged results for the exciton dispersion, that method was clearly inferior to a subband expansion in k-space.

The advantages of a $\vec{k}$-space based subband expansion, which proved so much more efficient in the QW case, are lost in the QWR case for several reasons: First of all, most technologically important QWR systems have only *weak* confinement in at least one direction. This implies that many subband pairs will contribute. Of similar importance are the Coulomb integrals, which have to be calculated and stored for each basis state pair and each z-distance. Coulomb integrals can be obtained more or less analytically only for model systems with rectangular or circular cross section and simple single-particle states. Using such basis states for general, more complicated shapes, however, will lead to poor convergence with basis size. Finally, and may be even more important, the Hamilton matrix in a subband expansion is no longer sparse. The difficulties involved in a QWR calculation are high-lighted by the fact that many papers have been written on valence-band structure effects on the single-particle level [36, 39, 40, 42, 107, 108], which is conceptionally and numerically much easier than the calculations of the two-particle wavefunction for the exciton. They focus mainly on free-carrier inter-subband absorption and polarization properties, which are considered to be a good test for the 1D-character of the involved states.

Similar to exciton calculations in QW, the choice of the COM coordinate $R_x = \beta x_e + (1-\beta)x_h$ is numerically very important for calculations at larger momentum along the wire (x-axis). The significance of the optimization of the COM transformation for the numerical convergence was discussed in Sect. 4.4.

7.2 Single-particle dispersions

The same real-space program used for the calculation of the exciton dispersions was used to obtain the single-particle dispersions for the conduction and valence band. Due to the lower dimensionality, much denser meshes can be used in this case; we present here results obtained with a 251 × 251 mesh on an area of 50nm × 80nm in the confinement plane. The numerical subband dispersions for electrons and holes are displayed in Fig. 7.1. A large number of subbands can be seen for both the conduction and valence band; this is due to the S-QW and the weak confinement along the y direction. As was already mentioned in the last section, this high number of subbands makes an expansion of the exciton wavefunction in products of electron and hole subband states, which was so successful in QW, numerically inefficient.

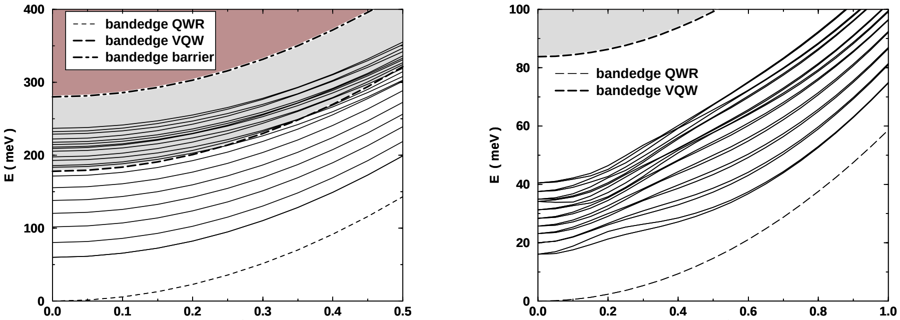

(a) (b)

Figure 7.1: V-groove GaAs/Al$_x$Ga$_{1-x}$As quantum wire: (a) Electron subband dispersions ($m_{CB_1} \approx 0.07 m_0$) (b) Hole subband dispersions. The band edges of the wire (thin dashed), of the V-QW (thick dashed) and of the barrier material (thick dot-dashed) are also displayed. The shadings visualize the continuum of the wire material (gray) and of the V-QW material (dark gray).

The electron, described by an effective mass that varies with aluminum concentration, see Tab. 7.1, is the simplest ingredient of our QWR exciton model. The subband dispersions, seen in Fig. 7.1(a), are rather parabolic and show no avoided crossings except when approaching the QWR continuum. Fig. 7.2 presents a selection of electron single-particle states for a momentum $k_e = 0.25\text{nm}^{-1}$ which is representative for electrons in the finite-momentum excitons discussed below. Besides 'typical QWR states', Fig. 7.2(a,b), also states are seen which are better described as states of the S-QW, Fig. 7.2(c), or the V-QW, Fig. 7.2(d). Altogether, a smooth transition from QWR states to well states is found, which should make electron trapping into the wire region efficient. Due to the heavier electron mass in AlGaAs barriers, effective confinement weakens with increasing electron momentum along the wire, $k_{e,x}$, and the electron envelopes reach deeper into the barriers.

In contrast to the electron, the hole dispersion, Fig. 7.1b, and the correspond-

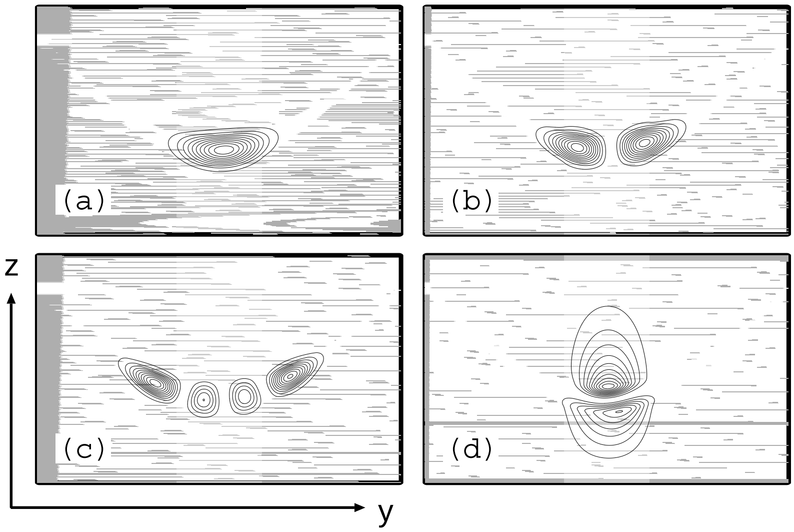

Figure 7.2: V-groove GaAs/Al$_x$Ga$_{1-x}$As quantum wire: Some of the lowest electron-subband states at $k = 0.25\text{nm}^{-1}$. Each panel shows an area of 50nm × 80nm. The shading marks the aluminum concentration $x = 0.33$, 0.21 and 0 in barrier (dark gray), vertical quantum well (light gray), and horizontal quantum well and crescent-shaped wire region (white), respectively.

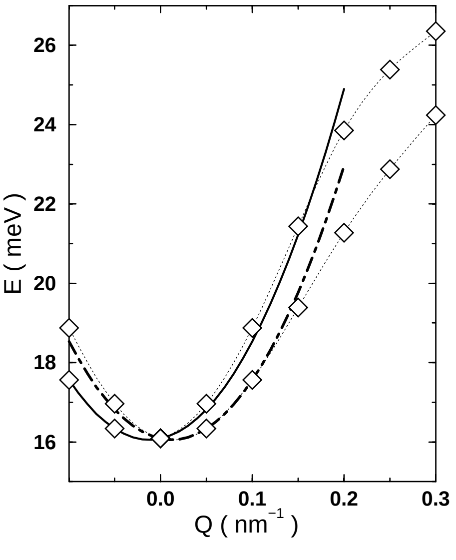

Figure 7.3: Quadratic fit including a linear term to the dispersion of the lowest hole subband doublet ($m_{HH_1} \approx 0.18 m_0$, $Q_{min} \approx 0.03\text{nm}^{-1}$) of Fig. 7.1.

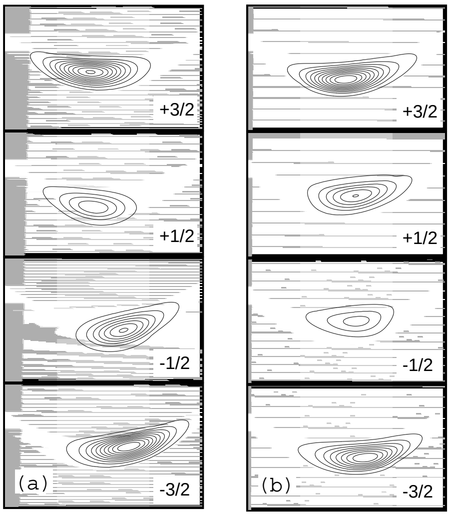

Figure 7.4: Probability distribution of the m_J-components for the spin-split lowest hole-subband pair at $k = 0.25\text{nm}^{-1}$. $E(b) - E(a) = 2.5\,\text{meV}$. Panels cover an area of 25nm × 40nm.

ing states exhibit some non-trivial features. The hole subband dispersions are, again, highly anharmonic due to the different masses of heavy and light holes. The LH_1 subband starts at the Γpoint around 34meV and an avoided crossing feature can be seen with all the lower HH subbands, which show no nodes in the direction of strongest confinement.

The hole subbands are spin-split at finite momentum due to the lack of inversion symmetry [45, 46]. The splitting is more pronounced for the lowest hole subband. It starts linearly for small k and leads to the subband minimum being slightly off the Γpoint, at about 0.03nm^{-1}, as clearly visible in Fig. 7.3.

The spin-splitting results from the terms of the Luttinger Hamiltonian, Eq. (2.9, 2.10), which are linear in the momentum along the wire axis;

$$H_{Lutt} = h^{(0)} + k_{h,x}\, h^{(1)} + k_{h,x}^2\, h^{(2)}\,. \tag{7.1}$$

These connect only 3/2 states with 1/2 states:

$$h^{(1)}_{\pm\frac{3}{2},\pm\frac{1}{2}} = \mp 2\sqrt{3}\gamma_3 \partial_y \ , \ \ h^{(1)}_{\pm\frac{3}{2},\mp\frac{1}{2}} = \mp 2\sqrt{3}\gamma_2 \partial_z\,. \tag{7.2}$$

They give a non-zero contribution only, if inversion symmetry is violated, e.g., by the confining potential $V_{conf}(y, z)$. (The spin-splitting is *not* related to the slight deviation from mirror symmetry $y \leftrightarrow -y$.)

The probability distribution of the spin components m_J (along the horizontal z-axis) at finite momentum is shown for the lowest two states in Fig. 7.4. The difference in energy goes along with a change of the distribution in real space. The components of the state with lower energy penetrate further into the S-QW region; those components with positive m_J are in the groundstate displaced to the left, those with negative m_J are displaced to the right. Note further a vertical displacement of the maxima between corresponding components.

The slight left-right asymmetry of the wire causes a minor additional shift of *all* components to the right. Not surprisingly, the light-hole components $m_J = \pm 1/2$ penetrate further into the V-QW than $m_J = \pm 3/2$ components. Only exactly at $\vec{k} = 0$, eigenstates with strong spin-polarization (close to $\pm 3/2$) can be found; for finite Q, the spin-polarization is small. We will find these features for the exciton dispersion and the hole densities within the exciton, too.

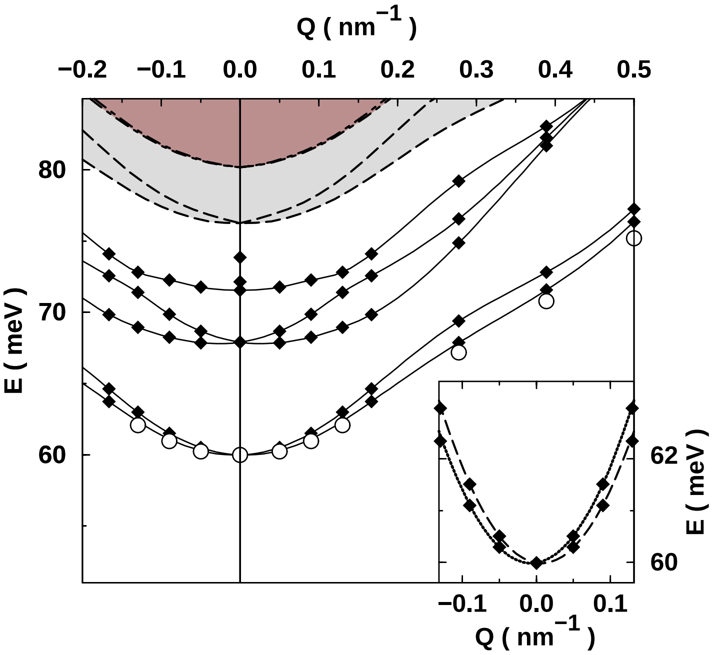

Figure 7.5: Dispersion of the lowest exciton states in a V-groove QWR (diamonds). For the lowest groundstate branch, results are shown for the denser mesh as open circles. The exciton continuum edges for the HH_1C_1 pairs (gray, dashed) and the LH_1C_1 pairs (dark-gray, dash-dotted) are included. Inset: The spin-split groundstate dispersion with parabolic fits on enlarged scale. Note the small linear contribution and the small minimum shifts.

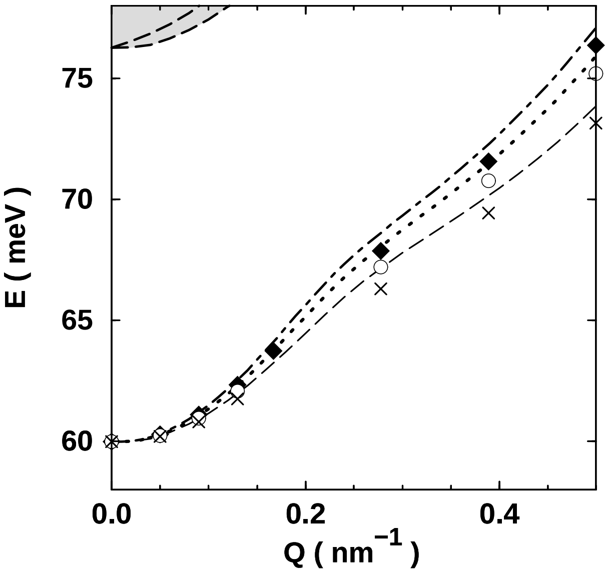

Figure 7.6: Comparison of groundstate exciton dispersion on the coarser (diamonds) and the finer mesh (circles) with the vertically displaced exciton continuum edges calculated on the same grids, (dot-dashed and dotted, respectively). The fully converged continuum edge (dashed) is vertically displaced for comparison as well as for estimation of the numerical accuracy. Small crosses mark the extrapolation for the exciton dispersion, see text.

7.3 Exciton dispersion in V-groove quantum wires

We present here exciton dispersion results for the 4-component wavefunctions on a coarser grid of $N_s \times N_{ye} \times N_{yh} \times N_{ze} \times N_{zh} \times N_x = 4 \times 17^2 \times 17^2 \times 27 \approx 10^7$ and a finer grid of $4 \times 23^2 \times 23^2 \times 27 \approx 3 \times 10^7$ sites for a five-dimensional volume of 57nm, 37nm, and 120nm in y, z, and x direction, respectively. With these grids, a good accuracy can be obtained if the COM transformation (3.11) is optimized and the groundstate-adapted discretization of the Coulomb potential, Sect. 5.2.1, is used. Due to the huge matrix size, we are limited to very few lowest eigenstates; for the denser grid to *the* lowest state. In Fig. 7.5, we show the exciton dispersions obtained for our V-groove QWR.

A spin-splitting analogous to that discussed for the hole subbands is clearly seen. It is weak within the lowest doublet (inset of Fig. 7.5), but large for the next higher doublet. For the lowest doublet, the linear contribution to the dispersion can reliably be obtained from a polynomial fit to the data, with the minimum at $Q = 0.007\text{nm}^{-1}$.

An enlightening discussion of why the lowest doublet is split and why the split is much stronger in T-shaped QWR than in V-groove QWR is given by Goldoni et al. in Ref. [39]. They note that the HH1 state of one of the two QW constituting a T-shaped QWR has a strong LH component from the point of view of the second QW and vice versa. Hence, the respective HH1 subbands couple strongly, leading to a strong avoided-crossing and a large spin splitting. The argument is formulated for single-particle states there, but applies to excitons as well. We shall point out that, as the present calculation does include the vertical quantum well, one should not be surprised to see in our QWR a feature which has been identified as characteristic for T-shaped wires. However, for this particular QWR, the confinement in the GaAs region is too strong for the V-QW to play a significant role for the groundstate exciton. Note that in the exciton equation, terms linear in Q occur beyond those of Eq. (7.1,7.2) with $k_{h,x}$ replaced by k_h from Eq. (4.9). They result from the quadratic terms $k_{h,x}^2 h^{(2)}$ and H_e when the expressions (4.9) are inserted.

One can trace back the dominant non-parabolicity of the groundstate dispersion in Fig. 7.5 to an avoided crossing near $Q \approx 0.28\text{nm}^{-1}$ with the higher exciton band that starts at Q=0 as an LH_1C_1 exciton. This is not surprising based on similar experience with excitons in bulk [57] and QW [30, 31, 33] as well as with single-particle hole subbands discussed before.

In the QW case, a comparison of the non-parabolic exciton dispersion with the electron-hole-pair edge, or exciton continuum edge, $\mathcal{E}_{n_e n_h}(Q)$ in Eq. (4.18), proved rather useful. Similar to the QW case, the exciton groundstate dispersion for our QWR is found to follow quite closely the exciton continuum edge, Fig. 7.6, from which it inherits its strong non-parabolicity. Both flatten at higher COM momentum.

The exciton dispersions are reasonably well converged, as the small differences between the results obtained for the two different meshes prove. However, the absolute energies are far from convergence. This is primarily due to the discretization error in the kinetic energy of the electron and, to a lesser extent, the hole. Rigid vertical shifts of up to about 5 meV are included in Fig. 7.5 and Fig. 7.6, such that the groundstate excitons, and in Fig. 7.6 the shifted continuum edge, coincide at $Q = 0$. We stress that the exciton binding energies (difference to the continuum edge) calculated with the two meshes differ only by 0.1meV (16.3meV vs. 16.2meV). As an aside, we remark that for a comparable QW of 6.3nm width with similar material parameters a binding energy of 10.5meV is found. This fact is evidence of a substantial wire confinement.

For an estimation of the Q-dependent numerical uncertainties and to show the increase of binding energy with increasing momentum, we display in Fig. 7.6 the groundstate exciton dispersion on both grids with the vertically displaced continuum edges derived from single-particle subbands calculated on the same grids. We already stated that the exciton dispersion follows quite closely the exciton continuum edge. The exciton dispersion lies consistently below the appropriately shifted continuum edge. This shows an increase in binding energy with Q, which is almost the same for both grids and is related to the mass increase along the dispersion. The exciton dispersion relative to the continuum edge seems to be better converged than the continuum edges. Since the latter can be obtained with high accuracy as a combination of single-particle properties, we are able to guess where a fully converged exciton dispersion would be (crosses in Fig. 7.6). This shows the achieved high numerical accuracy for the dispersions.

We want to emphasize that, as found before in QW, the easily obtainable exciton continuum edge yields a surprisingly reliable guide for the numerically expensive groundstate exciton dispersion. Furthermore, the sign and magnitude of the remaining small deviation can be guessed based on the physical argument of an increasing groundstate exciton binding energy for hole dispersions which become flatter at larger momentum (hole mass and reduced mass increase). The higher excitons follow their respective continuum edges much less closely than the groundstate (not shown). In particular, the exciton spin splitting within the lowest doublet is at large Q smaller than anticipated based on the difference of the respective continuum edges.

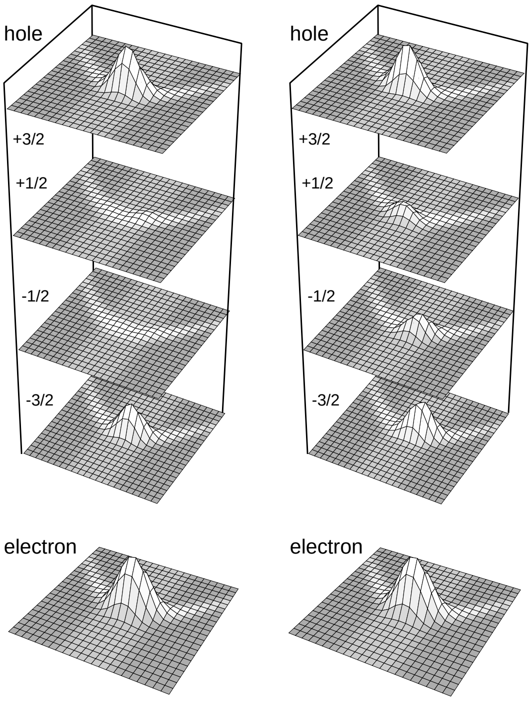

Figure 7.7: Groundstate exciton for $Q = 0.09\text{nm}^{-1}$ (left) and $Q = 0.28\text{nm}^{-1}$ (right). Hole densities for the different m_J-components, as well as the electron density are shown on 37nm × 57nm areas.

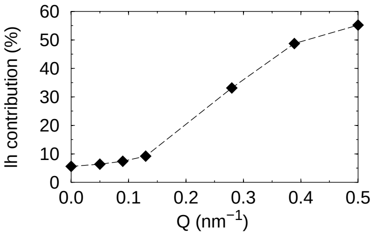

Figure 7.8: Contribution of bulk light-hole states ($m_J = \pm 1/2$) to the exciton groundstate versus COM momentum Q.

7.4 Exciton wavefunctions

Fig. 7.7 shows the multi-component character of the groundstate exciton wavefunction near the origin as well as at a COM momentum close to the avoided-crossing region. A strong admixture of the light-hole states ($m_J = \pm 1/2$) is seen for the larger Q. The light-hole contribution increases further for even larger COM momenta, as shown in Fig. 7.8. Note that this is only in part due to mixing of LH_1C_1- HH_1C_1 exciton; similarly to the hole subbands in QW, the lowest hole subband (HH_1) itself acquires a strong contribution of 'bulk light-hole states', i.e., $m_J = \pm 1/2$ - components; see Fig. 7.4.

For a more detailed analysis of the internal structure of the exciton with increasing momentum, we display in Fig. 7.9 the exciton extension along all five coordinates. For each one of these, the squared wavefunction was summed over the remaining four directions and, in the right panels, over angular momentum components. Then the root-mean-square deviation was calculated. The strong confinement of electron and hole along the growth direction, z, is clearly seen; confinement is weaker in the S-QW-direction y. The largest extension is that of the relative motion along the wire (x-direction). With increasing COM momentum, the hole in the exciton can relax in the weakly confined direction. However, the exciton contracts at the same time along the wire axis. The latter change is stronger, suggesting a slight enhancement of the exciton binding energy with Q, in agreement with the discussion of Fig. 7.5, 7.6 and similar to the results in comparable QW. The density profiles in the yz-plane can be fitted well by Gaussian functions, see Fig. 7.10(a). For density profiles along the wire, see the discussion of Fig. 7.11, below. On the coarser mesh, higher exciton states can be obtained as well. Their hole densities and relative wavefunction along the wire are shown in Fig. 7.11. For their description, we use a notation like HH_2C_1-s for QWR excitons which states, e.g., that this particular exciton branch is at Q=0 derived from the second QWR hole subband which has primarily heavy-hole ($m_J = \pm 3/2$) character and from the lowest electron subband; along the wire axis, the dominant component(s) have no nodes and therefore resemble an s-state.

The two states of Fig. 7.11(b) which lie above the groundstate doublet (Fig. 7.11(a) with clear HH_1C_1-s character) have one node in the S-QW di-

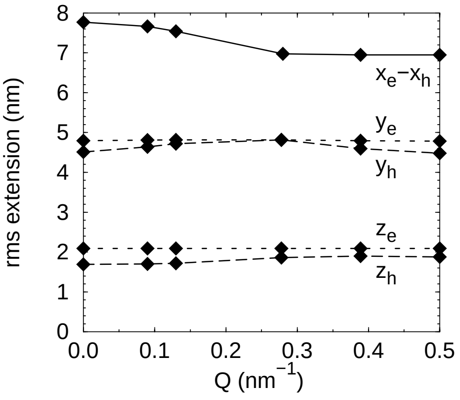

Figure 7.9: Spatial extension (root mean-square) of the exciton groundstate along each dimension versus COM momentum Q.

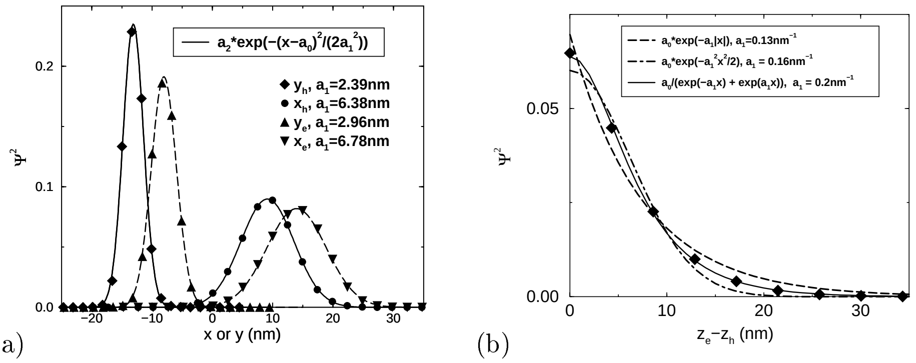

(a) (b)

Figure 7.10: Quality of various fit functions for the description of the exciton groundstate probability distribution along (a) the confinement space coordinates and (b) the relative coordinate in the growth direction. The latter can be fitted almost perfectly by a hyperbolic secant (line).

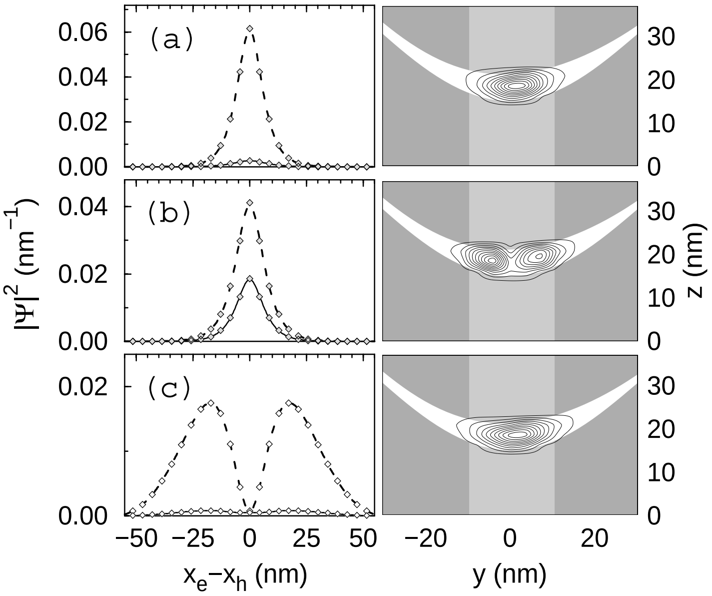

Figure 7.11: Right: Hole densities in yz-plane. Left: Density of the relative wavefunction components (dashed: heavy hole $m_J = \pm 3/2$, solid: light hole $m_J = \pm 1/2$) along the wire for the lowest three doublets at $Q = 0$. From top to bottom: $\mathrm{HH}_1\mathrm{C}_1$-$s$, $\mathrm{HH}_2\mathrm{C}_1$-$s$, $\mathrm{HH}_1\mathrm{C}_1$-$p$. Lines are hyperbolic-secant fits in panels (a) and (b), and a spline fit in (c) to the numerical data (diamonds).

rection. They can be interpreted as originating from a heavy-hole state with one node, and are, thus, $\mathrm{HH}_2\mathrm{C}_1$-$s$ states. The next doublet, Fig. 7.11(c), has one node along the wire, resembling a p-state. As it has no nodes in the yz-plane for both electron and hole coordinate, it is a $\mathrm{HH}_1\mathrm{C}_1$-$p$ doublet. Note its much larger extension in wire direction compared to the s-states, which goes along with an increased size in the S-QW-direction, at least in comparison to the s-state of the same subband pair, Fig. 7.11(a).

The relative motion in wire direction is determined by the Coulomb interaction, modified by form factors. In analogy to two-dimensional results, a wavefunction shape between an exponential and a Gaussian is expected and is seen in Fig. 7.11(a,b), indeed. The large-distance behavior is approximately exponential; at small distances, the relative wavefunction does not show a cusp, because the effective Coulomb interaction is weakened at small distances. For the groundstate, a hyperbolic-secant shape fits the squared wavefunction almost perfectly, see Fig. 7.10(b).

This brings us to the question, how closely the exciton groundstate wavefunction can be approximated by a factorization Ansatz of the form

$$\psi_{gs} \approx \varphi_{rel}(x_e - x_h)\, \varphi_e(y_e, z_e)\, \varphi_h(y_h, z_h)\, \chi_0 \,, \tag{7.3}$$

with suitably chosen functions φ_e, φ_h, for the single-particle electron- and hole-wavefunctions in the confined directions and φ_{rel}, for the relative motion along the wire and with a spatially constant four-component vector χ_0. Having the numerical exciton wavefunction at hand, this can be easily answered. At a not too large momentum of $Q = 0.09\text{nm}^{-1}$ (see left panel of Fig. 7.7) an overlap of 94% between the factorized Ansatz Eq. (7.3) and the numerically exact result can be obtained if only the $m_J = \pm 3/2$ components are included, i.e., $\chi_0 = (1/\sqrt{2}, 0, 0, -1/\sqrt{2})$. This is rather high, especially in view of the fact that in Ritz's variational principle, eigenvalue errors are proportional to the square of the wavefunction deviation. The inclusion of $m_J = \pm 1/2$ components, which is needed for larger Q, increases the overlap only to 95%.

7.5 Polarization anisotropy

From the calculated exciton groundstate wavefunction, the polarization anisotropy of the exciton line can be calculated. Some results on the polarization dependence of luminescence and absorption of V-groove wires are known from experiments [109, 41] and from single-particle calculations [39, 42]. For the anisotropy at the onset of the continuum of a QWR, which should be comparable to our case, Refs. [41, 42] give an average value of 10%, whereas Refs. [109, 39] state 10-20% for a V-groove QWR of different geometry. For the relative absorption strength, as given by the squared momentum matrix element averaged over the groundstate doublet (corresponding to the different electron spin states),

$$a_{j=}\frac{1}{2}\sum_{\pm} |\langle 0|\,\hat{p}_j\,|\Psi^X_{gs\pm}\rangle|^2 \quad , i = x, y, z \,, \tag{7.4}$$

we find the following values:

$$\frac{a_x - a_y}{a_x + a_y} = 0.12 \,, \quad \frac{2a_z}{a_x + a_y} = 0.01 \,. \tag{7.5}$$

This confirms what one would expect based on the single-particle results, e.g., combining the upper left corners of Fig. 7.2 and Fig. 7.4. Absorption with light polarized along z involves the $m_J = \pm 1/2$ components, which are according to Fig. 7.8 weak, whereas light polarized in the xy - plane is absorbed by the $m_J = \pm 3/2$ components. The dominantly heavy-hole states of the lowest exciton doublet are more polarizable along x than along y. The absorption anisotropy is in good agreement with the experimental results. The fact, that the single-particle results of Ref. [39, 42] are so close to Eq. (7.5), is probably due to the high overlap of the exciton wavefunction with the factorized form Eq. (7.3), which in turn reflects the strong carrier confinement in V-groove QWR.

7.6 Exciton center-of-mass mass

As discussed in Chapt. 6, the concept of a kinetic COM mass for a non-parabolic dispersion depends on the momentum range that is considered. In Table 7.2

some values of a kinetic COM mass for the groundstate exciton in the considered QWR and in QW with 5 and 10 nm well width are included. The QW widths correspond roughly to the wire's z-width, which ranges in the central region from about 8nm to 3nm; it takes into account that the lower Al concentration in the V-QW weakens the confinement compared to GaAs/Al$_{0.33}$Ga$_{0.67}$As QW. The Luttinger parameters of Table 7.1 yield in the spherical approximation for the bulk heavy-hole mass $m_h/m_0 = (\gamma_1 - 4\gamma_2/5 - 6\gamma_3/5)^{-1} = 0.49$, thus $m_e + m_h = 0.56 m_0$. As the QW and QWR dispersions are strongly non-parabolic, average values derived from parabolic fits to the dispersion in a Q-range of about the inverse Bohr radius ($Q < 0.1\mathrm{nm}^{-1}$) are reported.

Included in Table 7.2 are the results of the simple approximate expression for the exciton mass Eq. (6.2). These are obtained from the single-particle subband dispersions $\epsilon_{e,h}(k)$ and the squared Fourier transform $\Psi_{Q=0}(k)$ of the exciton wavefunction at vanishing COM momentum Q. Within the factorization approximation, Eq. (7.3), only the Fourier transform $\tilde{\varphi}_{rel}(k_x)$ is important, and the mass formula reads

$$\begin{aligned} M_X &= m_e + m_h \qquad \text{with} \\ \frac{1}{m_{e,h}} &= \frac{1}{\hbar^2} \int dk_x \, |\tilde{\varphi}_{rel}(k_x)|^2 \, \frac{\partial^2}{\partial {k_x}^2} \, \epsilon_{e,h}(k_x) \; . \end{aligned} \tag{7.6}$$

A decrease of the exciton mass going from GaAs bulk to GaAs/AlGaAs QW and QWR can be understood as result of the heavy- and light-hole separation due to confinement. For our QWR, we find a mass of 0.33 m_0. The agreement of the simple expression (7.6) with the result of the full numerical calculation is for the QWR case not as good as for QW. We attribute this to a stronger momentum dependence of the exciton's internal structure, probably reflecting the smaller subband separations and the linear terms in the dispersions.

M_X/m_0	QWR	5nm QW	10nm QW
$Q < 0.1$ nm^{-1}	0.27 (0.33)	0.31	0.32
Eq. (7.6)	0.28	0.29	0.31

Table 7.2: Kinetic COM mass for the groundstate $HH_1C_1 - 1s$ exciton derived from fits of dispersion in the range $Q < 0.1\mathrm{nm}^{-1}$ and from expression (7.6). In parenthesis: mass from extrapolated dispersions of Fig. 7.6.

Chapter 8

Summary and Outlook

A thorough study of the exciton center-of-mass properties in quantum wells and quantum wires has been presented in this work. The $\vec{k} \cdot \vec{p}$ coupling of heavy- and light-hole valence bands as well as the Coulomb potential have been taken fully into account. Our main achievements have been:

- We attacked the very old problem of optimizing the COM transformation for numerical calculations of excitons originating from degenerate bands [58, 57]. An *optimization methodology* other than the simple trial and error method has been introduced, based on Ansätze for the dependence of the exciton groundstate on the COM momentum Q, Chap. 4.
- We introduced an explicit Ansatz for the COM dependence of the exciton groundstate, Eq. (4.13), which proved to be very efficient. In particular, we found the *envelope* of the exciton groundstate in the subband expansion to be independent of the COM momentum to a good approximation.
- The COM optimization has lead to an *analytical expression* for an estimate of the exciton groundstate COM mass, Eq. (6.1,6.2). This estimate promises to be of great practical importance as it is based on *simple ingredients*: an estimate for the exciton groundstate at vanishing COM momentum and the knowledge of the subband dispersions. It proved to give quite good results for the average mass of the groundstate exciton in a momentum range of an inverse Bohr radius around $Q = 0$, which is the relevant momentum range for exciton localization problems.

The above innovations allowed us to calculate exciton dispersions even at quite large Q with unprecedented accuracy! We further:

- investigated the applicability of real-space discretization methods for exciton dispersion calculations, comparing the results of a simple finite-differences discretization scheme with state of the art calculations in momentum space in QW. Due to the high dimensionality of the configuration space, real-space discretization methods are suitable only for the calculation of a few lowest states. However, the method can be, and, indeed, it was successfully applied also for a realistic QWR model.

- We were, to the best of our knowledge, the first to calculate multi-band exciton states with full Coulomb coupling in QWR at all.

Our investigations revealed some interesting effects:

- The groundstate exciton dispersion follows rather closely the respective exciton continuum edge, Eq. (4.18).
- A non-monotonous increase of the exciton groundstate binding energy with increasing Q is observed; The binding energy is particularly large in the vicinity of avoided crossings of the subband dispersions.
- A small electron-hole correlation along the growth direction for the GaAs/$\mathrm{Al_{0.3}Ga_{0.7}As}$ quantum wells was found; It contributes insignificantly to the exciton groundstate binding energy.
- A rather small spin-splitting of the exciton groundstate in V-groove QWR was found.
- The exciton groundstate in the investigated V-groove QWR can be quite well described with a factorization Ansatz.

We could also reproduce some recent experimental findings:

- The polarization anisotropy of absorption data in V-groove QWR.
- The enhanced exciton reduced mass in $\mathrm{Zn_{0.87}Cd_{0.13}Se}$/ZnSe and ZnSe/$\mathrm{Zn_{0.85}Mg_{0.15}Se}$ QW observed in magneto-exciton experiments, Sect. 6.4.

As an outlook, we would like to list some physical properties that can be obtained from calculations of the groundstate exciton or the lowest exciton doublet for given COM momentum:

- We already mentioned the possible application of QWR in lasers. For their modeling, optical transition matrix elements and the density of states are needed.
- Exciton localization involves COM wavefunctions, which in turn can be obtained by a COM Schrödinger equation that needs the groundstate dispersion or at least the exciton mass as input [10]. The same is true for relaxation processes and diffusion.
- Results on the quantum confined Stark effect in QWR [6, 110] and experiments in magnetic fields [111, 112] could be obtained by inclusion of the appropriate terms in the Hamiltonian.

The exciton dispersion also enters the polariton dispersion [30], where, however, a much smaller momentum range (of the order of the photon momentum) is relevant. For such an application the mass from Eq. (4.7) obtained with the separation Ansatz, see Sect. 4.6, could be of use, since the solution of the exciton problem for $Q = 0$ is a much easier task than at $Q > 0$.

Appendix A

Hole Subband Mass in Symmetric Quantum Wells from Perturbation Theory

The envelopes of the QW subband states at $k = 0$ are, given their confinement energy, analytically known, since heavy- and light-hole valence band decouple at the Γpoint. Thus, perturbation theory for small in-plane momentum k can be used in order to calculate analytically the second derivative of the subband dispersions at the Γpoint. Such a work has previously been done by Foreman [62], who, however, used other boundary conditions than ours. We performed, therefore, similar analytical calculations using the symmetrized form of the Luttinger Hamiltonian, Eq. (2.9, 2.10), which we present here. The hole mass derived along this lines has been compared to the QW exciton mass from our semi-analytical formula, Eq. (6.2), in Sect. 6.2.

It is well known [22], that a unitary transformation U exists

$$U \quad = \quad 1/\sqrt{2}\begin{pmatrix} -e^{-i\varphi} & 0 & 0 & -ie^{-i\varphi} \\ 0 & ie^{i\eta} & e^{-i\eta} & 0 \\ 0 & -ie^{i\eta} & e^{-i\eta} & 0 \\ -e^{-i\varphi} & 0 & 0 & ie^{-i\varphi} \end{pmatrix}, \tag{A.1}$$

with

$$\begin{aligned} \varphi &= +(\chi - \theta + \pi)/2 \\ \eta &= -(\chi + \theta + \pi)/2 \\ \chi &= \arctan\left(\frac{\gamma_+ - \gamma_-}{\gamma_+ + \gamma_-}\tan(2\theta)\right) \end{aligned} \tag{A.2}$$

which brings the Luttinger Hamiltonian into block-diagonal form

$$H_{Lut} \quad = \quad -\frac{\hbar^2}{2m_0}\begin{pmatrix} \mathcal{P}+\mathcal{Q} & \mathcal{R} & 0 & 0 \\ \mathcal{R}^\dagger & \mathcal{P}-\mathcal{Q} & 0 & 0 \\ 0 & 0 & \mathcal{P}-\mathcal{Q} & \mathcal{R} \\ 0 & 0 & \mathcal{R}^\dagger & \mathcal{P}+\mathcal{Q} \end{pmatrix}, \tag{A.3}$$

where

$$\mathcal{R} \;=\; \mid \mathcal{M} \mid - i \mid \mathcal{L} \mid \tag{A.4}$$

and $\vec{k} = (k, \theta)$ in polar coordinates. In the axial approximation, Eq. (2.14), ($\gamma_- = 0$, $\chi = 2\theta$) this transformation is material-independent and can be also used for heterostructures.

All k-dependent terms are then viewed as perturbation to the Luttinger Hamiltonian for $k = 0$. Working much along the lines of [62], we derive the following expression for the in-plane hole mass:

$$\begin{aligned}
m_{\|}^{-1} &= I_{w1} + I_{w2} + I_{b1} + I_{b2} \\
I_{w1} &= (\gamma_1^w \pm \gamma_2^w \mp 3(\gamma_3^w)^2/\gamma_2^w) P_w \\
I_{w2} &= \mp 6\gamma_3^w \frac{k_1 \kappa_0}{k_0^2 - k_1^2} \Big(k_1(\sigma + \Delta) - \frac{\gamma_1^b \mp 2\gamma_2^b}{\gamma_1^w \mp 2\gamma_2^w} \kappa_0 (\rho - \lambda\Delta) \Big) P_b \\
I_{b1} &= \Big(\gamma_1^b \pm \gamma_2^b \mp 3 \frac{(\gamma_3^b)^2}{\gamma_2^b} \Big) P_b \\
I_{b2} &= \pm 6\gamma_3^b \frac{\kappa_0 \kappa_1}{\kappa_0 + \kappa_1} \Delta P_b
\end{aligned} \tag{A.5}$$

with

$$\begin{aligned}
\sigma &= \frac{1}{\kappa_0} \Big(\frac{\gamma_3^w}{\gamma_2^w} \frac{E_0}{E_0 + V_0} - \frac{\gamma_3^b}{\gamma_2^b} \Big) \\
\rho &= -\frac{1}{k_1} \Big(\frac{\gamma_3^w}{\gamma_2^w} - \frac{\gamma_1^b \pm 2\gamma_2^b}{\gamma_1^w \pm 2\gamma_2^w} \frac{\gamma_3^b}{\gamma_2^b} \pm \frac{\gamma_3^b - \gamma_3^w}{\gamma_1^w \pm 2\gamma_2^w} \Big) \\
\lambda &= \frac{\gamma_1^b \pm 2\gamma_2^b}{\gamma_1^w \pm 2\gamma_2^w} \frac{\kappa_1}{k_1} \\
\Delta &= \frac{\rho \big(\tan(k_1 L/2) \big)^{\pm 1} \mp \sigma}{\pm 1 + \lambda \big(\tan(k_1 L/2) \big)^{\pm 1}},
\end{aligned} \tag{A.6}$$

and

$$\begin{aligned}
&P_b = 1 - P_w \\
&k_0 = \sqrt{\frac{-E_0}{\gamma_1^w \mp 2\gamma_2^w}} \qquad k_1 = \sqrt{\frac{-E_0}{\gamma_1^w \pm 2\gamma_2^w}} \\
&\kappa_0 = \sqrt{\frac{V_0 + E_0}{\gamma_1^b \mp 2\gamma_2^b}} \qquad \kappa_1 = \sqrt{\frac{V_0 + E_0}{\gamma_1^b \pm 2\gamma_2^b}}
\end{aligned} \tag{A.7}$$

The indices b, w denote barrier and well material, respectively. k_0, and κ_0 denote wavevector and decay length of the subband envelope at the Γpoint in the well and barrier material, respectively, and E_0 is the energy of the subband at the same point. In the expressions above, the upper sign is valid for light-hole subbands and the lower for heavy-hole ones. P_b, P_w denote the probability for the hole to be in the barrier and well material, respectively, with

$$P_w \quad = \quad \frac{\left(1 \pm \frac{\sin(k_0 L)}{k_0 L}\right)}{\left(1 \pm \frac{\sin(k_0 L)}{k_0 L}\right) + \left(1 \pm \cos(k_0 L)\right)/\kappa_0 L}\,, \tag{A.8}$$

where the upper sign applies to even and the lower to odd subband states.

Appendix B

Transfer-Matrix Method

The usual single-band transfer-matrix method can be extended to degenerate bands and has been successfully applied to planar heterostructures, like superlattices [97]. The transfer-matrix formalism used in this work for the calculation of subband states in QW is presented here in short for the sake of a complete description of our numerical approach. As mentioned in Sect. 5.1, of particular advantage for our work has been the fact, that the single-particle wavefunctions calculated with the transfer-matrix method are obtained in an analytical form in terms of few numerically determined parameters. This has simplified considerably the calculation of the Coulomb form factors, Eq. (5.7).

In general, the transfer-matrix method is suitable for the solution of systems of linear differential equations with piecewise constant coefficients. The eigenvalue problem describing the single-particle dispersion in QW and superlattices belongs to this category; the Hamiltonian Eq. (3.4, 2.9,2.10) is ($k_z \to -i\partial_z$) of the form

$$H(\vec{k},z) = -\partial_z A(\vec{k},z)\partial_z - \frac{i}{2}\left(\partial_z B(\vec{k},z) + B(\vec{k},z)\partial_z\right) + C(\vec{k},z) \;, \qquad \text{(B.1)}$$

with the coefficient matrices A, B, and C determined by material constants.

The system of second order differential equations can be reduced to one of first order for the sought eigenfunction $\psi(z)$ and its first order derivative

$$\partial_z \overline{\phi}(\vec{k},z) = \Lambda(\vec{k},z)\overline{\phi}(\vec{k},z)\,, \qquad \text{(B.2)}$$

with $\bar{\phi} = (\psi(z),\, \partial_z\psi(z))^T$ and

$$\Lambda = \begin{pmatrix} 0 & \mathbf{I} \\ A^{-1}(C - E\mathbf{I}) & -iA^{-1}B \end{pmatrix} , \qquad \text{(B.3)}$$

where E denotes the eigenvalue and $\mathbf{I}$ the identity matrix. For constant coefficients, the solution is a combination of exponentials

$$\overline{\phi}(z) = \exp(\Lambda(z - z_0))\overline{\phi}(z_0) = P \cdot \exp(\lambda(z - z_0)) \cdot P^{-1}\overline{\phi}(z_0)\,, \qquad \text{(B.4)}$$

where P is the unitary transformation that brings Λ in its diagonal form λ.

Since the solution in each material separately is known, one has just to match the wavefunctions from either side of an interface. The symmetrized form of the Hamilton operator (B.1) implies, after integrating over the interface and requiring that no singular contributions to the energy exist, that the quantity $-A(\vec{k},z)\partial_z\psi(z) - \frac{i}{2}B(\vec{k},z)\psi(z)$ has to be continuous, additionally to the wavefunction. That is, the quantity $J\bar{\phi}$ has to be continuous, where

$$J \;=\; \begin{pmatrix} \mathbf{I} & 0 \\ -\frac{i}{2}B & -A \end{pmatrix}. \tag{B.5}$$

It is now easy to construct the matrix that "transfers" the solution, written in the diagonal representation of the respective layers, from the first layer to the last one

$$T = P_N^{-1}\cdot J_N^{-1}\cdot \prod_{n=2}^{N-1}\left(J_n\cdot P_n\cdot e^{\lambda_n d_n}\cdot P_n^{-1}\cdot J_n^{-1}\right)\cdot J_1\cdot P_1\,, \tag{B.6}$$

where N is the number of material layers in the structure, and d denotes the thickness of each layer.

Bound states vanish at infinity; they can involve only exponentially decaying terms in the outer layers. Defining projection operators U_1 and U_N that remove the exponentially growing terms at the outer layers (diagonal matrices with value 1 for the elements of the respective diagonal matrix λ that correspond to the exponentially decaying terms, and 0 otherwise), the solution must satisfy $(\mathbf{I}-U_N)\cdot T\cdot U_1\bar{\phi} = 0$. Non-trivial solutions exists, where the determinant

$$\det\left((\mathbf{I}-U_N)\cdot P_N^{-1}\cdot J_N^{-1}\cdot \prod_{n=2}^{N-1}\left(J_n\cdot P_n\cdot e^{\lambda_n d_n}\cdot P_n^{-1}\cdot J_n^{-1}\right)\cdot J_1\cdot P_1\cdot U_1\right) = 0 \tag{B.7}$$

vanishes. This condition is easy to implement numerically, since all the matrices involved are known analytically as functions of the material parameters. It is, however, somewhat difficult to follow the subband dispersions with k, since they come quite close at avoided crossings. We use the following procedure: We densely scan the determinant at the Γpoint using a mesh of trial energy E values starting somewhat above the band edge of the well material and ending somewhat below the band edge of the barrier material. Then, starting from the minima found, we use the golden rule method to locate the roots. For increasing k, we bracket the minima by the values half between the previous and next root at the previous value of k and then use the golden rule to find the new minima. For wide QW, where the spacing between the subbands becomes quite small, a dense mesh of k values has to be taken. However, the method does not require too much computer resources, and more simple strategies that are easier to implement like, e.g., scanning densely the determinant for each value of k and subsequent use of the golden rule method, should be sufficiently efficient as well.

For symmetric QW, the subband states at each value of k are twofold degenerate. The obtained degenerate wavefunctions are linear combination of even and odd states with respect to the specular reflection σ_{xy}, see Sect. 5.1, and are subsequently disentangled. The numerical results have been checked against the analytical results of Ref. [78].

Appendix C

Single-band Exciton with Effective Potential

In Chapt. 6, we derived an analytical expression for an effective exciton mass related to the COM motion of the exciton groundstate, Eq. (6.1,6.2). The ingredients for this expression are simply the involved single-particle dispersions and the exciton wavefunction for vanishing COM momentum or, at least, some good estimate for the Bohr radius a_B. We want here to demonstrate, that there are simple single-band models for the description of the exciton groundstate in QW which give quite satisfactory results for the extension of the groundstate exciton, i.e., the Bohr radius a_B entering the mass formula.

We display in Fig. C.1(a),(b) results for the numerical exciton groundstate binding energy and the respective Bohr radius obtained from full calculations and compare with results obtained from a simple variational method. The variational results were obtained using a 2D 1s exciton Ansatz in a single-band model with the numerically calculated multi-band single-particle dispersions. The potential used was an effective 2D Coulomb potential [?]

$$V^*_{Coul}(\rho) = -\frac{e^2}{\epsilon}\frac{1}{bL_{eff}} Arsh\left[\frac{bL_{eff}}{\rho}\right] \tag{C.1}$$

that reproduces correctly the limits of large ($V^*_{Coul}(\rho \to \infty) \propto 1/\rho$)and vanishing ($V^*_{Coul}(\rho \to 0) \propto \ln(\rho)$) relative particle distance in QW. The fit parameter b was taken as $b = 0.4$ by fitting the exciton groundstate binding energies to the ones obtained from full single-band calculations in Ref. [?]. This effective potential has a simple Fourier transform

$$V^*_{Coul}(k) = -\frac{e^2}{\epsilon}\frac{1 - e^{-0.4kL_{eff}}}{0.4L_{eff}k^2} \tag{C.2}$$

and can thus be easily handled also in momentum space.

The effective QW width L_{eff} entering Eq. (C.1) was obtained by minimizing the sum of the confinement energies of the two particles with $\cos(\pi z/L_{eff})$

wavefunctions. It shows, Fig. C.1(c), the maximum exciton confinement at approximately the same QW width as the full calculations.

For widths between 2nm and 15nm, very good results for the groundstate binding energy (deviations <5%) are obtained; the Bohr radii are consistently 1.-1.5nm smaller than the actual ones. The deviation is, not surprisingly, larger for the wavefunctions than for the energies. Still, the error in the Bohr radius is only of the order of 10%; hence, they can be used, together with the analytical formula for the exciton mass, to give quite a good estimate for the exciton groundstate mass.

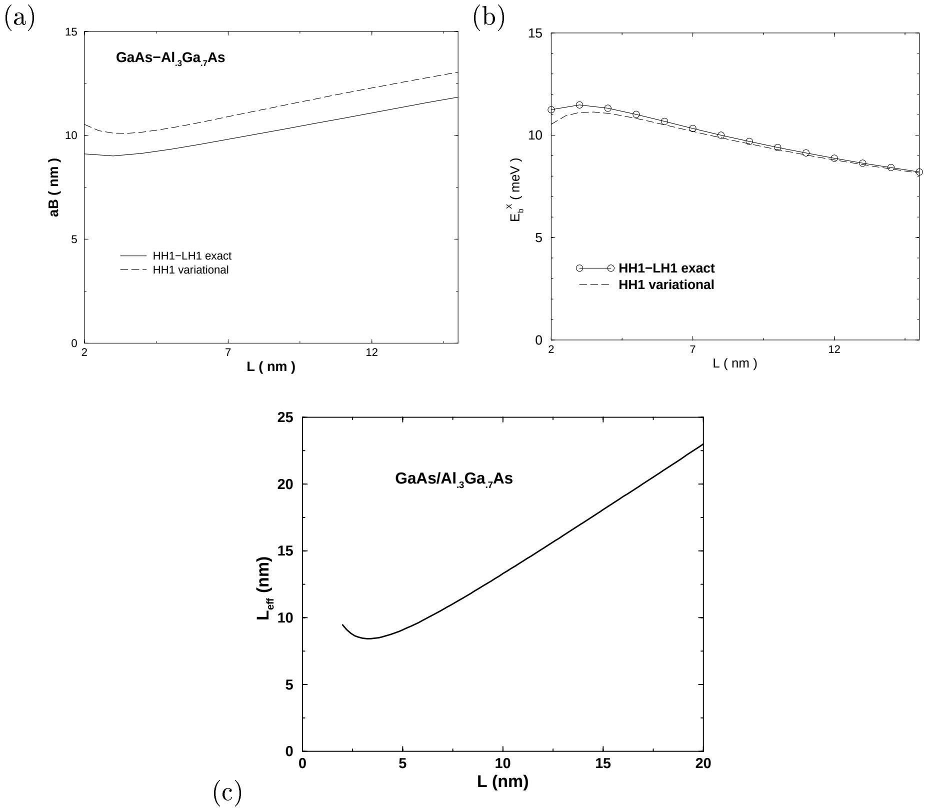

Figure C.1: (a) Exciton groundstate binding energy and (b) Bohr radius a_B versus QW width L obtained from a simple variational single-band calculation compared to the results of the elaborate full multi-band calculation of Sect. 5.1. (c) Effective L_{eff} versus real L width for GaAs/Al$_{0.3}$Ga$_{0.7}$As QW used for the variational calculations.

Appendix D

Absorption in Quantum Wells

The formalism for the calculation of oscillator strengths and absorption coefficients in QW in terms of single-particle and exciton wavefunctions is well known [?, 52]. We will present it here briefly, with a special focus on the selection rules in symmetric QW. We will consider both the absorption due to the interaction-free electron-hole system and due to the exciton, since we discuss in Sect. 5.1.1.5 also results for the Sommerfeld enhancement factor.

D.1 Absorption due to the interaction-free electron-hole system

The absorption of not too intense linearly polarized light from a system of N_e electrons is described for allowed transitions and in the dipole approximation (vanishing photon momentum) by the interaction operator

$$H^{dip}_{e-ph} = \frac{eA}{m_0 c} \left(\hat{e} \cdot \sum_{i=1}^{N_e} \vec{p}_i \right) e^{-i\omega t} \, , \tag{D.1}$$

where ω is the frequency, $\hat{e}$ the polarization vector, and $\vec{A}$ the corresponding vector potential (in the Coulomb gauge) of the electromagnetic field, and $\vec{p}_i$ is the momentum of the respective particle. Defining for a single QW the absorption coefficient in QW $a^{QW}(\omega)$ as absorbed energy per time and unit area divided by the energy flux [52], leads to a dimensionless quantity, in contrast to the 3D case. First order perturbation theory and Fermi's rule yields the following expression for $a^{QW}(\omega)$

$$a^{QW}_{\hat{e}}(\omega) \;=\; \frac{4\pi^2 e^2}{\eta \mathcal{A} c m_0^2 \omega} \sum_{n_e,\, n_h} \int d\vec{k}' \, \frac{\mathcal{A}}{(2\pi)^2} \, \delta\left(\hbar\omega - \mathcal{E}_{n_h}(\vec{k}') + \mathcal{E}_{n_e}(\vec{k}') \right) \times$$

$$\left| \langle \mathbf{0} \,|\, \hat{e}\cdot \sum_{i}^{N_e} \vec{p}_i \,|\, n_e \vec{k}' \rangle \, | n_h \vec{k}' \rangle \right|^2 , \qquad \text{(D.2)}$$

with $|\,\mathbf{0}\rangle$ the many-body ground state and η the index of refraction. The single-particle states in the above expression are normalized with respect to the area $\mathcal{A}$.

In symmetric QW, parity with respect to the specular reflection σ_{xy} is a good quantum number, see Sect. 5.1. Following Eq. (5.2),

$$\langle 0 \,|\, \hat{e}\cdot \sum_{j} \vec{p}_j \,|\, n_e j_e \, n_h p_h \, \vec{k} \rangle = \langle n_e j_e \, \vec{k} \,|\, \hat{e}\cdot\vec{p} \,|\, n_h p_h \rangle = \qquad \text{(D.3)}$$

$$\sum_{m_J} \int dz \, \xi^{m_J *}_{n_h, p_h, \vec{k}} (z) \; \xi_{n_e} (z) \; \langle \frac{3}{2} \, m_J \,|\, \hat{e}\cdot\vec{p} \,|\, \frac{1}{2} \, j_e \rangle = \sum_{j_e m_J} \mathcal{D}^{j_e m_J}_{n_e n_h p_h} (\hat{e}; k) \, .$$

Since vectors in the xy-plane (parallel to z) are of even (odd) parity with respect to σ_{xy}, the selection rule $\Delta p = \pm 1$ holds; the upper sign holds for in-plane polarization. The momentum operator matrix elements within our basis, (four components for the hole, Eq. (2.8), and two for the electron), are given by

$$p_x = \frac{P_{cv}}{\sqrt{6}} \begin{pmatrix} \sqrt{3} & 0 & 1 & 0 \\ 0 & i & 0 & i\sqrt{3} \end{pmatrix}, \quad p_y = \frac{P_{cv}}{\sqrt{6}} \begin{pmatrix} i\sqrt{3} & 0 & -i & 0 \\ 0 & -1 & 0 & \sqrt{3} \end{pmatrix},$$

$$p_z = \frac{2 P_{cv}}{\sqrt{6}} \begin{pmatrix} 0 & -i & 0 & 0 \\ 0 & 0 & 1 & 0 \end{pmatrix} . \qquad \text{(D.4)}$$

Note the vanishing contribution of the heavy-hole bulk edge states to absorption for polarization p_z along the growth direction.

Defining the dimensionless oscillator strength $f^{\hat{e}} \left(\vec{k} \right)$ in analogy to atomic physics, one derives after integration over the direction of $\vec{k}$ (axial approximation)

$$f^{\hat{e}}_{\substack{n_e j_e \\ n_h p_h}} (k) \;=\; \frac{2}{m_0 \left(-\mathcal{E}_{n_h} (k) + \mathcal{E}_{n_e} (k) \right)} \sum_{j_e j_h} \left| \mathcal{D}^{j_e j_h}_{n_e n_h p_h} (\hat{e}; k) \right|^2 \qquad \text{(D.5)}$$

and[1]

$$a^{sQW}_{\hat{e}} (\omega) = \frac{4\pi^2 a}{\eta} \frac{\hbar^2}{2\, m_0} \sum_{n_e n_h} 2 \int \frac{k' dk'}{2\pi} \, \delta \left(\hbar\omega - \mathcal{E}_{n_h} (k') + \mathcal{E}_{n_e} (k') \right) f^{\hat{e}}_{n_e n_h} (k') \, , \qquad \text{(D.6)}$$

where $\hat{e} = e_z \, \hat{z} + \vec{e}_\perp$, $a = e^2/\hbar c \approx 1/137$ the fine-structure constant, and $f^{\hat{e}}_{n_e n_h}(k) = e_z^2 \, f^{\hat{z}}_{n_e n_h}(k) + e_\perp^2 \, f^{\hat{x}}_{n_e n_h}(k)$.

---

[1] Changing the parity of both electron and hole just changes the sign of the momentum operator matrix element

$$\begin{aligned} \langle n_e \; -p_e \, \vec{k} \,|\, \hat{e}\cdot\vec{p} \,|\, n_h \; -p_h \, \vec{k} \rangle &= \langle n_e p_e \, \vec{k} \,|\, (R_\pi T)^{-1} \; \hat{e}\cdot\vec{p} \, (R_\pi T) \,|\, n_h p_h \, \vec{k} \rangle \\ &= -\langle n_e p_e \, \vec{k} \,|\, \hat{e}\cdot\vec{p} \,|\, n_h p_h \, \vec{k} \rangle . \end{aligned}$$

This gives the factor 2 in Eq. (D.6).

D.2 Excitonic absorption in quantum wells

Working along the same lines as in the previous section, the absorption coefficient for exciton formation in the QW is given by

$$a_{\hat{e}}^{X,QW}(\omega) \;=\; \frac{4\pi^2 e^2}{\eta \mathcal{A} c m_0^2 \omega} \sum_{\nu} \delta\left(\hbar\omega - \mathcal{E}_{\nu 0}^{X}\right) \left| \langle \mathbf{0} \,|\, \hat{e}\cdot \sum_i \vec{p}_i \,|\, \nu\, 0 \rangle \right|^2 , \tag{D.7}$$

where $|\nu 0\rangle$ denotes an exciton state at vanishing COM momentum Q of energy $\mathcal{E}_{\nu 0}^{X}$ with ν standing for the remaining quantum numbers. The summation is replaced by an integration in the exciton continuum. Using the subband expansion Eq. (5.3,5.4), with the subband states now normalized with respect to the area $\mathcal{A}$, the dipole matrix element is

$$\langle \mathbf{0} \,|\, \hat{e}\cdot \sum_i \vec{p}_i \,|\, \nu j_e P\, 0 \rangle = \frac{\sqrt{\mathcal{A}}}{2\pi} \sum_{n_e n_h} \int d\vec{k}\, \varphi_{n_e n_h}^{0;\,\nu}(\vec{k}) \langle n_e j_e \vec{k} \,|\, \hat{e}\cdot\vec{p} \,|\, n_h p_h \vec{k} \rangle \,. \tag{D.8}$$

In the axial approximation, the angular momentum ℓ is a good quantum number at $Q = 0$. Due to the phase factors of the single-particle states in the axial approximation, Eq. (5.2), the dipole matrix element becomes after the integration over the angle

$$\begin{aligned} \langle \mathbf{0} \,|\, \hat{e}\cdot \sum_i \vec{p}_i \,|\, \ell \nu j_e P\, 0 \rangle \;=\; & \\ \sqrt{\frac{\mathcal{A}}{2\pi}} \sum_{n_e n_h} \int k dk\, \varphi_{n_e n_h \ell}^{0;\,\nu}(k) & \left(\sum_{m_J} \delta_{0,\ell - m_J + \bar{m}_J}\, \mathcal{D}_{n_e j_e n_h p_h}^{m_J}(\hat{e}; k) \right) . \end{aligned} \tag{D.9}$$

That is, for excitonic absorption the selection rule $|\ell| \leq J_e + J_h$ is valid, with ℓ the angular momentum of the relative motion of the exciton, and J_e, J_h the total angular momenta of the conduction and valence band, respectively. This is the analogue to the $\ell = 0$ selection rule for the absorption of free electrons. Only for the angular momentum values $|\ell| \leq J_e + J_h$, there is a spin component with a finite probability for the electron and hole occupying the same space coordinates.

The polarization selection rules are exactly the same as for the non-interaction electron-hole system; this is because the Coulomb interaction has a higher (spherical) symmetry than the heterostructure potential.

Appendix E

Numerical Solution of the Exciton in Real Space

E.1 Finite-differences discretization

The discretization of the symmetrized operators, Eq. (3.5), has to be done carefully, in order to keep the discretized operator Hermitian. We used the following differentiation patterns:

$$\begin{aligned} \left(\left(\partial_x \gamma\, \partial_x\right) f\right)_0 &= \gamma_{+\frac{1}{2}} f_{+1} - \left(\gamma_{+\frac{1}{2}} + \gamma_{-\frac{1}{2}}\right) f_0 + \gamma_{-\frac{1}{2}} f_{-1}\,, \\ \left(\tfrac{1}{2}\left(\gamma\, \partial_x + \partial_x \gamma\right) f\right)_0 &= \tfrac{1}{2}\left(\gamma_{+\frac{1}{2}} f_{+1} - \gamma_{-\frac{1}{2}} f_{-1}\right)\,, \end{aligned} \tag{E.1}$$

and

$$\begin{aligned} &\left(-\tfrac{1}{2}\left(\partial_x \gamma\, \partial_y + \partial_y \gamma\, \partial_x\right) f\right)_{0,0} = \\ &\quad \tfrac{1}{4}\left(\gamma_{+\frac{1}{2},+\frac{1}{2}} + \gamma_{-\frac{1}{2},-\frac{1}{2}} - \gamma_{-\frac{1}{2},+\frac{1}{2}} - \gamma_{+\frac{1}{2},-\frac{1}{2}}\right) f_{0,0} + \\ &\quad \tfrac{1}{4}\left(\gamma_{-\frac{1}{2},+\frac{1}{2}} f_{-1,+1} + \gamma_{+\frac{1}{2},-\frac{1}{2}} f_{+1,-1} - \gamma_{+\frac{1}{2},+\frac{1}{2}} f_{+1,+1} - \gamma_{-\frac{1}{2},-\frac{1}{2}} f_{-1,-1}\right)\,. \end{aligned} \tag{E.2}$$

It can be easily verified that the resulting matrices are Hermitian.

E.2 Coulomb discretization

The discretization of the Coulomb potential is described in Sect. 5.2.1. For both QW and QWR, we used the 3D $1s$-exciton as basis $\varphi_{1s}^{3D}(r) = 2a_B^{-3/2} e^{-r/a_B}$ with energy $\mathcal{E}_{1s}^{3D} = \frac{\mu}{\epsilon}$Ryd. The reduced mass μ and Bohr radius a_B are derived from the electron and hole reference masses given in Sect. 5.2.1. Since we want to use the same discretization mesh for the reference system and for the real one.

Therefore, we write the Laplace operator as

$$T = \partial^2_{\rho_x} + \partial^2_{\rho_y} + \partial^2_{z_e - z_h} = \partial^2_{\rho_x} + \partial^2_{\rho_y} + \frac{1}{4}\left(\partial^2_{z_e} + \partial^2_{z_h} - 2\partial^2_{z_e z_h}\right)$$

and discretize according to the previous section. The Coulomb potential is then

$$V_{\{ijkl\}} \quad = \quad \frac{1}{d\Omega}\mathcal{E}^{3D}_{1s} + \frac{\hbar^2}{2\mu}\textstyle\sum_{\{i'j'k'l'\}} T^{\{i'j'k'l'\}}_{\{ijkl\}} e^{-\left(r_{\{i'j'k'l'\}} - r_{\{ijkl\}}\right)/a_B} \quad ,$$

where $\{ijkl\}$ are the grid-points indices in the 4D configuration space $\{x, y, z_e, z_h\}$, $r_{\{ijkl\}}$ the respective particle distance, $d\Omega$ the volume element of the mesh, and $T^{\{i'j'k'l'\}}_{\{ijkl\}}$ the discretized Laplace operator. A similar procedure is used for the QWR.

E.3 Efficient implementation of the matrix-vector product

Denoting with h_{ij}, $i, j = x_{e,h}, y_{e,h}, z_{e,h}$ the $z_{e,h}$-dependent coefficients matrices of the corresponding $k_i k_j$ products in the $\vec{k} \cdot \vec{p}$ -matrices of the one-particle Hamiltonians and setting $\vec{Q}_e = \beta\vec{Q}$, $\vec{Q}_h = (\beta - 1)\vec{Q}$, the QW exciton Hamilton operator takes the form

$$\begin{aligned}
H \quad = \quad & -h_{z_h z_h}\partial^2_{z_h} - h_{z_e z_e}\partial^2_{z_e} \\
& -(h_{x_h x_h} + h_{x_e x_e})\partial^2_{\rho_x} - (h_{y_h y_h} + h_{y_e y_e})\partial^2_{\rho_y} - (h_{x_h y_h} + h_{x_e y_e})\partial_{\rho_x}\partial_{\rho_y} \\
& -h_{x_h z_h}\partial_{\rho_x}\partial_{z_h} - h_{x_e z_e}\partial_{\rho_x}\partial_{z_e} - h_{y_h z_h}\partial_{\rho_y}\partial_{z_h} - h_{y_e z_e}\partial_{\rho_y}\partial_{z_e} \\
& -i\left(Q_{ey}h_{x_e y_e} + Q_{hy}h_{x_h y_h} + 2Q_{ex}h_{x_e x_e} + 2Q_{hy}h_{x_h x_h}\right)\partial_{\rho_x} \\
& -i\left(2Q_{ey}h_{y_e y_e} + 2Q_{hy}h_{y_h y_h} + Q_{ex}h_{x_e y_e} + Q_{hx}h_{x_h y_h}\right)\partial_{\rho_y} \qquad \text{(E.3)} \\
& +\Big\{Q^2_{hx}h_{x_h x_h} + Q^2_{hy}h_{y_h y_h} + 2Q_{hx}Q_{hy}h_{x_h y_h} \\
& +Q^2_{ex}h_{x_e x_e} + Q^2_{ey}h_{y_e y_e} + 2Q_{ex}Q_{ey}h_{x_e y_e} \\
& +\left(V_h(z_h) + V_e(z_e)\right)\boldsymbol{I}\Big\} \\
& +V_C\left(\sqrt{(z_e - z_h)^2 + \rho_x^2 + \rho_y^2}\right)\boldsymbol{I}\,.
\end{aligned}$$

We take advantage of the highly structured form of (E.3) and define 15 matrices $T^0_{e,h}\left(N_{z_e,z_h}, 4, 4\right)$, $T^{\pm}_{z_e,z_h}\left(N_{z_e,z_h} + 1, 4, 4\right)$, $T^{\pm}_{\rho_x,\rho_y}\left(\left(N_{z_e} + 1\right)\left(N_{z_h} + 1\right), 4, 4\right)$, $T_{\rho_x\rho_y}\left(\left(N_{z_e} + 1\right)\left(N_{z_h} + 1\right), 4, 4\right)$, $T_{(z_e,z_h)(\rho_x,\rho_y)}\left(N_{z_e,z_h} + 1, 4, 4\right)$ (in parenthesis are the dimensions). These contain all the coefficients needed: $T^0_{e,h}$ for the space-diagonal matrix elements that depend only on the $z_{e,h}$ coordinates, $T^{\pm}_{z_e,z_h,\rho_x,\rho_y}$ for the forward (backward) elements along the respective coordinate, and $T_{\rho_x\rho_y}$, $T_{(z_e,z_h)(\rho_x,\rho_y)}$ for the non-diagonal elements of the respective mixed derivatives. With these matrices and the potential matrix, one can easily and efficiently construct the matrix-vector product, using, e.g., the array features of FORTRAN90, which a good compiler can optimize automatically. All these matrices together need only a bit more than a quarter of the memory required for one eigenvector! We used a similar procedure for the QWR.

E.4 Matrix diagonalization

Discretization in real space of the excitonic equation of motion results in a sparse, complex Hermetian matrix of dimension up to $\approx 1.4 \cdot 10^7$ for grids fine enough to yield well converged results for the exciton dispersion. This matrix, which we will call the Hamilton matrix in the following, can be reduced to a real symmetric matrix only at vanishing COM momentum $Q = 0$. The sparsity pattern of the matrix consists of 44 non-vanishing off-diagonals (46 for the QWR calculations discussed in Chap. 7) additionally to the non-vanishing diagonal. The bandwidth of the Hamilton matrix, which for the QWR is at least $2(4N_{z_e}N_{y_e}N_{z_h}N_{y_h}N_{x_e-x_h})/\max(N_{z_e}, N_{y_e}, N_{z_h}, N_{y_h}, N_{x_e-x_h})$ (N_i the number of grid points along the i-coordinate, the factor 4 is the number of spin components), is too large for band matrix diagonalization routines to be efficient. In addition, all eigenvalues of the Hamilton matrix are twofold degenerate for symmetric QW and all $\vec{Q}$ as well as for QWR and $Q = 0$.

The dimension of the matrix is so large that only two general classes of diagonalization routines for sparse matrices are suitable: (i) out-of-core routines, where part of the matrix and eigenvectors is stored on the file system, and (ii) iterative routines that do not require to hold in memory the non-zero elements of the matrix, but require instead some user supplied routines.

We used the freely available software packet ARPACK, which is capable of solving large-scale Hermitian, non-Hermitian, standard or generalized eigenvalue problems. The software bases on the implicitly restarted Arnoldi method, an algorithmic variant of the Arnoldi process, that can be viewed as a synthesis of the Arnoldi/Lanczos process with the implicitly shifted QR algorithm. The software is well documented and is one of the most efficient ones for very large sparse matrices [103, **?**, 104]. A parallel version exists, called PARPACK, based on MPI or BLACS communication. We did not use PARPACK, due to the high dimensionality of the configuration space that would lead to too heavy communication between the single processing units.

Since we are interested in a few eigenvalues and eigenvectors at the edge of the spectrum, no shift-invert spectral transformations are necessary and only the matrix-vector multiplication routine has to be implemented. Due to the highly structured nature of our Hamilton matrix, the multiplication routine can be very efficiently implemented with additional memory consumption much less than that for one eigenvector. Hence, the total memory usage was given by the number of vectors used as iteration space. For a maximum of 10 desired lowest eigenvalues and respective eigenfunction an iteration subspace of 30 vectors has been used, in order to keep the CPU-usage reasonable. We used the maximum memory available on a CRAYJ90 at the Konrad-Zuse-Zentrum in Berlin, which was 1 Cray Gigaword.

Another advantage of this method is that multiple eigenvalues offer no particular difficulties, it is, however, necessary that the iteration space is sufficiently large and the requested convergence tolerance is sufficiently tight to capture all multiple instances. This point was, however, not a problem to us, since we were primarily interested in the dispersions, while both degenerate eigenfunctions could be obtained from the numerical one using symmetry considerations.

A further advantage of the ARPACK package is that the algorithm is completely based on BLAS and LAPACK routines, which are available and highly optimized for almost all platforms. For the vectorized version of our program, only the matrix-vector multiplication routine had to be explicitly vectorized, while for the optimization of the ARPACK software we just linked against the vectorized versions of the BLAS and LAPACK libraries. We achieved peak performance of 140MFlops/CPU, with the peak performance of the limiting BLAS routine being 185MFlops/CPU.

Bibliography

[1] L. Esaki and R. Tsu. IBM Res. Note RC-2418, 1969.

[2] W. Wegscheider, L. N. Pfeiffer, M. M. Dignam, A. Pinczuk, K. W. West, S. L. McCall, and R. Hull. *Phys. Rev. Lett.*, 71:4071, 1993.

[3] R. Ambigapathy, I. Bar-Joseph, D. Y. Oberli, S. Haacke, M. J. Brasil, F. Reinhardt, E. Kapon, and B. Deveaud. *Phys. Rev. Lett.*, 78:3579, 1997.

[4] L. Sirigu, D. Y. Oberli, D. Degiorgi, A. Rudka, and E. Kapon. *Phys. Rev. B*, 61:10575, 2000.

[5] T. Ogawa and T. Takagahara. *Phys. Rev. B*, 44:8138, 1991.

[6] S. Benner and H. Haug. *Phys. Rev. B*, 47:15750, 1993.

[7] S. Glutsch and F. Bechstedt. *Phys. Rev. B*, 47:4315, 1993.

[8] F. Rossi and E. Molinari. *Phys. Rev. Lett.*, 76:3642, 1996.

[9] A. L. Ivanov and H. Haug. *Phys. Rev. Lett.*, 71:3182, 1993.

[10] E. Runge and R. Zimmermann. *Festkörperprobleme/Advances in Solid State Physics*, 38:251, 1998.

[11] R. Zimmermann and E. Runge. *Phys. Stat. Sol. (a)*, 164:511, 1997.

[12] H. F. Hess, E. Betzig, T. D. Harris, L. N. Pfeiffer, and K. W. West. *Science*, 264:1740, 1994.

[13] T. C. Damen, J. Shah, D. Y. Oberli, D. S. Chemla, J. E. Cunningham, and J. M. Kuo. *Phys. Rev. B*, 42:7434, 1990.

[14] B. Devaud, F. Clèrot, N. Roy, K. Satzke, B. Sermage, and D. S. Katzer. 67:2355, 1991.

[15] P. Roussignol, C. Delalande, A. Vinattieri, L. Carraresi, and M. Colocci. *Phys. Rev. B*, 45:6965, 1992.

[16] R. Kumar, A. S. Vengurlekar, S. S. Prabhu, J. Shah, and L. N. Pfeiffer. *Phys. Rev. B*, 54:4891, 1996.

[17] M. Z. Maialle, E. A. Andrada e Silva, and L. J. Sham. *Phys. Rev. B*, 47:15776, 1994.

[18] A. Vinattieri, J. Shah, T. C. Damen, D. S. Kim, L. N. Pfeiffer, M. Z. Maialle, and L. J. Sham. *Phys. Rev. B*, 50:10868, 1994.

[19] J. Puls, F. Henneberger, M. Rabe, A. Siarkos. *J. of Crys. Growth*, 184/185:787, 1998.

[20] H. Chu, G. D. Sanders, and Y.-C. Chang. *Phys. Rev. B*, 36:7955, 1987.

[21] P. Michler, A. Hangleiter, A. Moritz, G. Fuchs, V. Härle, and F. Scholz. *Phys. Rev. B*, 48:11991, 1993.

[22] D. A. Broido and L. J. Sham. *Phys. Rev. B*, 31:888, 1985.

[23] D. A. Broido and L. J. Sham. *Phys. Rev. B*, 34:3917, 1986.

[24] G. D Sanders and Y.-C. Chang. *Phys. Rev. B*, 35:1300, 1987.

[25] L. C. Andreani and A. Pasquarello. *Phys. Rev. B*, 42:8928, 1990.

[26] C. Y.-P. Chao and S. L. Chuang. *Phys. Rev. B*, 48:8210, 1992.

[27] B. Zhu and Y.-C. Chang. *Phys. Rev. B*, 50:11932, 1994.

[28] J. Chen, R. Chen, and K. K. Bajaj. *Phys. Rev. B*, 50:10947, 1994.

[29] R. Winkler. *Phys. Rev. B*, 51:14395, 1995.

[30] S. Jorda, U. Roessler, and D. Broido. *Phys. Rev. B*, 48:1669, 1993.

[31] A. L. C. Triques and J. A. Brum. *Phys. Rev. B*, 56:2094, 1997.

[32] A. Siarkos, E. Runge, and R. Zimmermann. *Ann. d. Physik (Leipzig)*, 7:523, 1998.

[33] A. Siarkos, E. Runge, and R. Zimmermann. *Phys. Rev. B*, 61:10854, 2000.

[34] J.-B. Xia and K. W. Cheah. *Phys. Rev. B*, 55:1596, 1997.

[35] L. Banyai, I. Galbraith, C. Ell, and H. Haug. *Phys. Rev. B*, 36:6099, 1987.

[36] F. Rossi and E. Molinari. *Phys. Rev. B*, 53:16462, 1996.

[37] S. Glutsch, F. Bechstedt, W. Wegscheider, and G. Schedelbeck. *Phys. Rev. B*, 56:4108, 1997.

[38] S. N. Walck, T. L. Reinecke, and P. A. Knipp. *Phys. Rev. B*, 56:9235, 1997.

[39] G. Goldoni, F. Rossi, E. Molinari, and A. Fasolino. *Phys. Rev. B*, 55:7110, 1997.

[40] O. Stier and D. Bimberg. *Phys. Rev. B*, 55:7726, 1997.

[41] F. Vouilloz, D. Y. Oberli, M.-A. Dupertuis, A. Gustafsson, F. Reinhardt, and E. Kapon. *Phys. Rev. Lett.*, 78:1580, 1997.

[42] F. Vouilloz, D. Y. Oberli, M.-A. Dupertuis, A. Gustafsson, F. Reinhardt, and E. Kapon. *Phys. Rev. B*, 57:12378, 1998.

[43] M. Grundmann, O. Stier, and D. Bimberg. *Phys. Rev. B*, 58:10557, 1998.

[44] A. Siarkos and E. Runge. *Phys. Rev. B*, 61:16854, 2000.

[45] C. Kittel. *Quantum Theory of Solids.* John Wiley and Sons, N. Y., 1987.

[46] E. L. Ivchenko and G. E. Pikus. *Superlattices and Other Heterostructures: Symmetry and Optical Phenomena.* Springer-Verlag, New York, 1994.

[47] P. Y. Yu and M. Cardona. *Fundamentals of Semiconductors: Physics and Material Properties.* Springer-Verlag, Berlin Heidelberg, 1996.

[48] M. L. Cohen and J. R. Chelikowsky. *Electronic Structure and Optical Properties of Semiconductors.* Springer Verlag, Berlin Heidelberg, 1988 and 1989.

[49] S. Albrecht, L. Reining, R. del Sole, and G. Onida. *Phys. Rev. Lett.*, 80:4510, 1998.

[50] L. X. Benedict, E. L. Shirley, and R. B. Bohn. *Phys. Rev. Lett.*, 80:4514, 1998.

[51] M. Rohlfing and S. G. Louie. *Phys. Rev. Lett.*, 80:3320, 1998.

[52] G. Bastard. *Wave Mechanics applied to Semiconductor Heterostructures.* Halsted Press, New York, 1988.

[53] J. Singh. *Physics of Semiconductors and their Heterostructures.* McGraw-Hill Inc., New York, 1993.

[54] B. K. Ridley. *Quantum Processes in Semiconductors.* Clarendon-Press, Oxford, 1993.

[55] J. M. Luttinger. *Phys. Rev. B*, 102:1030, 1956.

[56] U. Rössler. *Solid State Commun.*, 49:943, 1984.

[57] M. Altarelli and N. O. Lipari. *Phys. Rev. B*, 15:4898, 1977.

[58] G. Dresselhaus. *J. Phys. Chem. Solids*, 1:14, 1956.

[59] E. O. Kane. *Phys. Rev. B*, 11:3850, 1975.

[60] U. Ekenberg. *Phys. Rev. B*, 40:7714, 1989.

[61] B. A. Foreman. *Phys. Rev. B*, 48:4964, 1993.

[62] B. A. Foreman. *Phys. Rev. B*, 49:1757, 1994.

[63] M. J. Godfrey and A. M. Malik. *Phys. Rev. B*, 53:16504, 1995.

[64] G. T. Einevoll and L. J. Sham. *Phys. Rev. B*, 49:10533, 1993.

[65] R. Eppenga, M. F. H. Schuurmans, and S. Colak. *Phys. Rev. B*, 36:1554, 1987.

[66] T. Ando, S. Wakahara, and H. Akera. *ISSP*, September 1989.

[67] B. Laikhtman. *Phys. Rev. B*, 46:4769, 1992.

[68] S. R. White and L. J. Sham. *Phys. Rev. B*, 47:879, 1981.

[69] R. A. Morrow and K. R. Brownstein. *Phys. Rev. B*, 30:678, 1984.

[70] M. F. H. Schuurmans and G. W. 't Hooft. *Phys. Rev. B*, 31:8041, 1985.

[71] R. Winkler and U. Roessler. *Phys. Rev. B*, 48:8919, 1993.

[72] D. B. Tran Thoai, R. Zimmermann, M. Grundmann, and D. Bimberg. *Phys. Rev. B*, 42:5906, 1990.

[73] D. F. Nelson, R. C. Miller, and D. A. Kleinman. *Phys. Rev. B*, 35:7770, 1987.

[74] E. L. Ivchenko, A. Y. Kaminski, and U. Roessler. *Phys. Rev. B*, 54:5852, 1996.

[75] T. Hassenkam, S. Pedersen, K. Baklanov, A. Kristensen, C. B. Sorensen, P. E. Lindelof, F. G. Pikus, and G. E. Pikus. *Phys. Rev. B*, 55:9298, 1996.

[76] S. Jorda. *Exzitonen und Exziton-Polaritonen in Quantentrögen.* PhD thesis, Regensburg, 1992.

[77] M. A. Kanehisa. *Physica*, 117/118B:275, 1983.

[78] L. C. Andreani, A. Pasquarello, and F. Bassani. *Phys. Rev. B*, 36:5887, 1987.

[79] B. Zhu and K. Huang. *Phys. Rev. B*, 36:8102, 1987.

[80] E. Kapon, D. M. Hwang, and R. Bhat. *Phys. Rev. Lett.*, 63:430, 1989.

[81] A. R. Goni, L. N. Pfeiffer, K. W. West, A. Pinczuk, H. U. Baranger, and H. L. Stormer. *Appl. Phys. Lett.*, 61:1956, 1992.

[82] M. Kohl, D. Heitmann, P. Grambow, and K. Ploog. *Phys. Rev. Lett.*, 63:2124, 1989.

[83] P. Ils, C. Greus, A. Forchel, V. D. Kulakovskii, N. A. Gippius, and S. G. Tikhodeev. *Phys. Rev. B*, 51:4272, 1995.

[84] R. Nötzel, N. N. Ledentsov, L. Däweritz, K. Ploog, and M. Hohenstein. *Phys. Rev. B*, 45:3507, 1992.

[85] I. Rasnik, L. G. C. Rego, M. V. Marquezini, A. L. C. Triques, M. J. S. P. Brasil, J. A. Brum, and M. A. Cotta. *Phys. Rev. B*, 58:9876, 1998.

[86] R. Nötzel, U. Jahn, Z. Niu, A. Trampert, J. Fricke, H.-P. Schönherr, T. Kurth, D. Heitmann, L. Däweritz, and K. H. Ploog. *Appl. Phys. Lett.*, 72:2002, 1998.

[87] E. Kapon, M. C. Tamargo, and D. M. Hwang. *Appl. Phys. Lett.*, 50:347, 1989.

[88] J. Wang, B. J. Robinson, D. A. Thompson, and J. G. Simmons. *Appl. Phys. Lett.*, 67:2358, 1995.

[89] M. Kappelt, M. Grundmann, A. Krost, V. Türck, and D. Bimberg. *Appl. Phys. Lett.*, 68:3596, 1996.

[90] E. Kapon, M. Walther, J. Christen, M. Grundmann, C. Caneau, D. M. Hwang, E. Colas, R. Bhat, G. H. Song, and D. Bimberg. *Superlatt. and Microstruc.*, 12:491, 1992.

[91] M. A. Dupertuis, 2000. private communication.

[92] C. Vanderstraeten. Electronic levels and exciton kinetics in a quantum wire including disorder. Master's thesis, Berlin, 1998.

[93] I. S. Gradshteyn and I. M. Ryzhik. *Table of Integrals, Series, and Products.* Academic Press, New York, 1994.

[94] Unfortunately, in Fig. 1 of Ref. [32] a different convention was used, with β replaced by $\beta - 1/2$.

[95] D. J. BenDaniel and C. B. Duke. *Phys. Rev.*, 152:683, 1966.

[96] B. Chen, M. Lazzouni, and L. R. Ram-Mohan. *Phys. Rev. B*, 45:1204, 1992.

[97] L. R. Ram-Mohan, K. H. Yoo, and R. L. Aggarwal. *Phys. Rev. B*, 38:6151, 1988.

[98] Landolt-Bornstein. *Elastic, Piezoelectric, Piezooptic, Electrooptic Constants, and Nonlinear Dielectric Susceptibilities of Crystals*, volume III/2a of *New Series.* Springer, Berlin, 1982. Ed. by O. Madelung.

[99] D. A. Broido, E. S. Koteles, C. Jagannath, and J. Y. Chi. *Phys. Rev. B*, 37:R2725, 1988.

[100] D. Y. Oberli, G. Boehm, G. Weimann, and J. A. Brum. *Phys. Rev. B*, 49:R5757, 1994.

[101] H. Chu and Y.-C. Chang. *Phys. Rev. B*, 39:10861, 1989.

[102] S. Glutsch, D. S. Chemla, and F. Bechstedt. *Phys. Rev. B*, 54:11592, 1996.

[103] U. Elsner, V. Mehrmann, F. Milde, R. A. Römer, and M. Schreiber. *SIAM J. Sci. Comp.*, 20:2089–2102, 1999.

[104] ARPACK and the parallel version PARPACK can be downloaded free of charge at http://www.caam.rice.edu/software.

[105] J. Puls, V. V. Rossin, F. Henneberger, and R. Zimmermann. *Phys. Rev. B*, 54:4974, 1996.

[106] J. Puls, M. Rabe, A. Siarkos, and F. Henneberger. *Phys. Rev. B*, 57:14749, 1998.

[107] P. C. Sercel and K. J. Vahala. *Phys. Rev. B*, 44:5681, 1991.

[108] D. S. Citrin and Y.-C. Chang. *Phys. Rev. B*, 43:11703, 1991.

[109] G. Goldoni, F. Rossi, E. Molinari, A. Fasolino, R. Rinaldi, and R. Cingolani. *Appl. Phys. Lett.*, 69:2965, 1996.

[110] K. Chang and J. B. Xia. *Phys. Rev. B*, 58:2031, 1998.

[111] G. Goldoni and A. Fasolino. *Phys. Rev. B*, 52:14118, 1995.

[112] S. N. Walck and T. L. Reinecke. *Phys. Rev. B*, 57:9088, 1998.

Acknowledgements

This work has been funded by the Deutsche Forschungsgemeinschaft in the frame of SFB 296. We gratefully acknowledge support by the Rechenzentrum of the Humboldt University and the Konrad-Zuse-Zentrum in Berlin, in particular through granting access to their Cray J932 (project bvph08as).

At this point I would like to express my thanks to all the people that one way or another contributed to this work.

I am particularly indebted to Prof. Dr. R. Zimmermann for support, for the many helpful discussions and suggestions throughout this work, as well as for the fruitful collaborations with other research groups he initiated.

My deepest gratitude belongs to Dr. E. Runge for his support and guidance (not only in matters of physics), for exhaustive and productive discussions on numerous topics, and also for having had a lot of patience with me. Much of my current physical, and numerical insight originates from working so close with him.

I am indebted to Dr. J. Puls for fruitful discussions, during which interesting questions aroused; they lead to valuable physical insights. I also wish to thank M. A. Dupertuis and C. Vanderstraeten for valuable contributions.

Further, I would like to thank all the colleagues that made the hard work such a fun; a special thanks to Y. Dhaibi, B. Starke, F. Neugebauer, F. Große, T. Altevogt, A. Esser, T. Mančal, S. Ramakrishna and our secretary, Mrs. Heider.

Last but not least, I would like to thank all my friends, that supported me during this time. Special thanks to Anna-Maria for her love and patience throughout the last years.

Lebenslauf

Name: Anastassios Siarkos
Geboren: 10. März 1966 in Berlin
Nationalität: Griechisch

10/1983 - 10/1987	Studium an der Aristoteles-Universität von Thessaloniki (Griechenland) in der Fachrichtung Physik. Diplom-Note: 1.6.
10/1990 - 10/1994	Aufbaustudium in der Fachrichtung Physik an der Technischen Universität Berlin. Diplom-Note: 1. Diplomarbeit in Theoretischer Festkörperphysik mit dem Thema Phononenankopplung an $^3A_2$-Multiplett von Ni-Zentren in II-VI-Verbindungen” unter der Betreuung von Prof. Dr. U. Scherz
02/1995 - 03/1999	Doktorand in der AG Halbleitertheorie im Inst. f. Physik der Humboldt-Universität zu Berlin (finanziert von der DFG im Rahmen des Sfb 296 ”Wachstumskorrelierte Eigenschaften niederdimensionaler Halbleiterstrukturen”) Anfertigung einer Dissertation mit dem Thema “Exciton Center-of-Mass Motion in Quantum Wells and Quantum Wires” unter Betreuung von Prof. Dr. R. Zimmermann und Dr. E. Runge

Selbständigkeitserklärung

Hiermit erkläre ich, die vorliegende Arbeit selbständig ohne fremde Hilfe verfaßt zu haben und nur die angegebene Literatur und Hilfsmittel verwendet zu haben.

Anastassios Siarkos 29. Mai 2000